CSIRO
MARINE RESEARCH

# A New Version of the Australian Community Ocean Model for Seasonal Climate Prediction

---

A. Schiller, J. S. Godfrey, P. C. McIntosh, G. Meyers, N. R. Smith*,
O. Alves*, G. Wang* and R. Fiedler

* Bureau of Meteorology Research Centre, Melbourne

April 2002

## CONTENTS

# ABSTRACT

A model-to-data intercomparison is performed as part of the LWRRDC-funded project "Extended seasonal climate predictions using a dynamical model". The Australian Community Ocean Model Version 2 (ACOM2) is the ocean component of a new seasonal prediction system for Australia, developed jointly between CSIRO Marine Research and the Bureau of Meteorology Research Centre. The main purpose of this report is to validate ACOM2 with observations. Furthermore, it is expected that the results presented in this report will serve as a reference for future work with this model. The report focuses on physical aspects of the model and addresses their potential impact on the forecast skill of the coupled ocean-atmosphere model.

A result of ACOM2 common to many other ocean general circulation models (OGCMs) is that simulated quantities representing the depth-integrated circulation, such as depth-integrated steric height, sea-surface height or depth of 20° C isotherm are better simulated than surface quantities like, e.g., SST. The near-surface circulation of the ocean is determined by model physics and exterior forcing (surface heat and freshwater fluxes, wind stresses). Both of these components contain errors irrespective of the source of the surface forcing (from observations as used in this report or from an atmospheric circulation model in a coupled mode), which hampers identification and rectification of model errors. Nevertheless, results presented here for oceanic surface circulation still reveal improvements over earlier models.

The main results of this report are summarised at the end. It is concluded that the winds used to drive the model seem to have serious deficiencies near 10° N in the Pacific. Most other differences between model and observation may be due either to model error or to flux problems. However, model error seems a likely cause for the broad-scale overestimate of thermocline depth, and for misrepresentation of mean water temperature and salinity in the eastern equatorial Pacific.

Overall, the implementation of an improved mixed-layer model, the parameterisation of tidal mixing in the Indonesian Archipelago, the enhanced meridional grid resolution, the better resolution of the Indonesian Archipelago and the reduced horizontal mixing all contribute to an improved ocean/atmosphere simulation in the coupled model runs, as was demonstrated in the comparison with the early version of the ocean model. None-the-less there is still space for significant improvements in the coupled ocean-atmosphere system, including data assimilation. This work will be a focus of the two modelling groups at BMRC and CMR over the next years.

# 1. INTRODUCTION

This Report describes a series of tests of an Ocean General Circulation Model (OGCM), built at CSIRO Marine Research to become the ocean component of the Australian Bureau of Meteorology's newly coupled climate model. This coupled model will be used by BoM as a part of its routine seasonal climate forecasts. Since a large number of coupled models are in use throughout the world, it is considered desirable to provide fairly exhaustive documentation of the performance of each component of the coupled model individually, as well as of the coupled model itself. The project to build this coupled model was supported by the Land and Water Resources Research and Development Council.

*Wang et al.* (2001) and *Zhong et al.* (2001a) provide a brief description of the performance of the new coupled model. The ocean model is ACOM2 (e.g. *Schiller et al.* 1998, *Schiller et al.* 2000); the atmospheric component is the Bureau of Meteorology unified Atmosphere Model (BAM). *Wang et al.* compared the new coupled model with its BoM predecessor, which used earlier versions of both the OGCM and the AGCM. *Zhong et al.* provide more detail on the performance of the newly coupled model. The newly coupled model, like its predecessor, is a state-of-the-art representation of the oceanic and atmospheric physics. It is capable of capturing variability associated with the ocean subsurface as well as the changes in the ocean surface temperature. These changes strongly affect local rainfall patterns, which in turn affect Australia and many other parts of the world by (primarily) atmospheric teleconnections.

Stand-alone testing of the Atmospheric General Circulation Model (AGCM) involves assessing the simulated atmospheric circulation and fluxes exerted on the earth's surface, when the AGCM is forced with observed solar forcing and the observed seasonally and interannually-varying SST. This has been done for an initial version of the AGCM used by BoM, as part of the Atmospheric Model Intercomparison Project (AMIP) (*Zhong et al*., 2001b).

This Report, which also fulfils a requirement of the LWRRDC contract, is concerned with the problem of assessing OGCM standalone performance. Specifically we wish to assess the ocean circulation (and SST patterns) generated by the OGCM, when it is driven with seasonally and interannually-varying "observed" surface fluxes. No single agreed standard for these fluxes exists at this time, so we discuss our choice of fluxes, and we use various methods to guard against errors introduced by flux uncertainty. The principal aim of the tests described here was threefold:

- to examine the skill of the model (and the imposed surface fluxes) in simulating observed seasonal and interannual sea-level patterns, when driven with "observed" surface forcing (especially wind stresses). We expected that this would not be particularly demanding of the model, because the calculation of sea-level is (to first approximation) a quite simple calculation involving wind-driven ocean waves. Thus it was expected that this test primarily acts as a check on the wind stress products used.

- to explore the performance of ACOM2 in simulating observed seasonal and interannual sea-surface temperature (SST) patterns, when driven with “observed” interannually-varying products for wind speed and stress, surface radiation and other surface forcings. Here good simulations depend on adequate representation of ocean mixed-layer processes. *Godfrey and Schiller* (1997) reported a one-dimensional test of the Chen-Power mixed-layer model used in ACOM2; high-quality flux and SST data from the four-month TOGA-COARE experiment were used for this test. SSTs were well simulated throughout this period when the model vertical resolution was 2m, though SST responses on timescales of a few days were degraded when the vertical resolution was coarsened to the 15m resolution used in ACOM2.

- In dynamically critical regions such as the equatorial strip and the Indonesian Throughflow, to compare the model's subsurface temperature, salinity and currents with available observations.

The comparison with observations is restricted to the equatorial and mid-latitude Pacific and Indian Oceans. In these areas the “memory” of the ocean has a significant impact on the atmosphere and thus on seasonal-to-interannual climate variability over Australia.

The technical details of ACOM2 (and a higher-resolution model, ACOM3) are described in Section 2, along with the way in which the two models were driven in these “standalone” experiments. Problems with the “observed” surface flux products we have used to drive the models are also described in Section 2. Despite their limitations, these products were expected to be a better representation of the “true” forcings applied to the real ocean than those provided by the coupled model, after several months of running in "forecast" mode - i.e. data-free coupled running, starting from observed initial conditions. Therefore the runs described here can provide information that complements the work of *Wang et al* and *Zhong et al*., in the following ways:

- We anticipate that these runs should provide a closer simulation of the observed mean seasonal cycle of surface and subsurface fields (for non-data assimilation runs). This is explored in Section 3.

- Due to use of observed forcing, correlation between observed and modelled SST anomalies in the ocean-only runs was expected to be better than from the coupled model, outside the equatorial Pacific Ocean. This, plus some analysis of SST dynamics in these regions, provides some indications of limits of possible SST predictability in these regions. These aspects are described in Section 4, which also gives a few comparisons of interannual subsurface variations with (limited) observational data.

We also briefly mention results from a run with the higher-resolution ACOM3 model with identical surface forcing in section 4, where they are instructive (the number of grid points in ACOM3 is approximately 15 times larger than in ACOM2; therefore it is currently not feasible to use ACOM3 in an operational seasonal prediction system).

In section 5 ACOM2 and the old ocean model (ACOM1) are compared during the data assimilation cycle. Statistics from the data assimilation procedure provide an estimate of the model errors.

A Summary in Section 6 briefly assesses ACOM2 compared to others reported elsewhere, in intercomparisons of coupled climate models (*Meehl et al*., 2001). The Appendix contains technical details about model configuration and choice of parameters.

# 2. MODEL DESCRIPTION

## 2.1 Model grids and special features

The global ocean model is based on the Modular Ocean Model (MOM2; *Pacanowski*, 1995). Zonal resolution is 2°. Within 8° of the equator the meridional model resolution is 0.5°, the meridional resolution decreases to 1.5° at the poles. The model has 25 levels, eight of which are in the uppermost 120 m of the model ocean.

ACOM2 applies the Chen et al. mixed-layer model (*Chen et al.,* 1994; level version courtesy of R. Kleeman, BMRC (*Power et al.*, 1995)) with additional improvements in ACOM2 made available by S. Wilson, CSIRO Atmospheric Research (*Wilson,* 2000). In addition, ACOM2 contains a simple parameterisation for tidal mixing in the Indonesian area (*Schiller et al.*, 1998), which improves the simulation of SST and heat flux exchange across the ocean-atmosphere interface. It was shown by *Schiller et al.* that this parameterisation improves the heat uptake of the ocean in the Indonesian Archipelago and therefore improves agreement with observed surface fluxes. ACOM2 also contains a scheme to simulate the inflows of warm and salty water masses from the Red and Mediterranean Seas into the Indian and Atlantic Ocean. A more detailed description of ACOM2 can be found in Appendix.

Some of the subsequent sections also use results from the global ACOM3 model. The model has a much higher horizontal (0.5º zonally and 0.33º meridionally) and vertical resolution (36 levels with a 10m resolution near the surface). This model contains the same special features as discussed above for ACOM2 (apart from relaxation of water-masses at the outflows of the Red and Mediterranean Seas). Due to its eddy-permitting resolution sub-grid mixing parameterisations are biharmonic rather than laplacian (as in ACOM2).

## 2.2 Surface forcing fields

This subsection describes the standard forcing fields for the main model run; modified surface forcing fields from other model runs are discussed in the appropriate sections.

Monthly mean FSU wind stresses in the Pacific and Indian Oceans were blended with 3-day mean NCEP wind stress deviations inside 30º N - 30º S in the two oceans. NCEP data were used elsewhere. FSU wind stresses were preferred, since they avoid systematic errors in stresses near the equator that are found in NCEP data. In the tropical and subtropical Indian and Pacific Oceans the wind stresses used to force the model were the sum of the monthly mean FSU wind stress plus the deviations of the NCEP winds from their monthly average. As a result, sub-monthly wind stress variability was solely determined by NCEP winds, whereas any monthly or longer average was determined by FSU winds. The two ocean regions were blended with pure NCEP winds outside this area by a simple linear interpolation with an approximate blending zone of 10º in all directions. The only exception is a narrow gap of approximately 5º longitude between the two Indian and Pacific Ocean FSU data sets. Unfortunately, this gap is along the Indonesian Throughflow area. The gap was filled by interpolation of the two blended FSU/NCEP data sets from the adjacent Indian and Pacific Ocean areas.

Surface heat fluxes and evaporation, apart from incoming shortwave radiation, are calculated by coupling ACOM2 to an atmospheric boundary-layer model (ABLM; *Kleeman and Power* (1995)). The use of an atmospheric boundary-layer model (ABLM), while still reasonably simple to interpret, takes proper account of surface heat and freshwater fluxes during the period investigated. The ABLM consists of a single-layer model atmosphere (boundary-layer as well as a portion of the cloud layer) that is in contact with the surface. Wind fields at the 850 hPa level are assumed to be representative of the circulation in the atmospheric boundary layer and are prescribed (NCEP).

Air potential temperature is treated as a prognostic variable, while air relative humidity is taken from a 3-day averaged climatology (NCEP). The air temperature tendency equation includes the effects of horizontal and vertical advection, horizontal diffusion of transient eddies, turbulent sensible heat exchange with the surface, plus a term representing the radiative cooling at the top of the atmospheric boundary layer. The model atmosphere also predicts land temperatures (with a very short time constant), which allows investigation of atmospheric transport processes from land to ocean. Surface heat fluxes (using FSU/NCEP surface winds rather than 850 hPa winds) are diagnosed from the ABLM. Use of the ABLM leads to improved simulations of SST and its anomalies. Note that in all experiments shown below, SST has not been prescribed but has been calculated with fluxes provided by the ABLM. The ABLM is not used in the coupled version of ACOM2 and BAM.

The upward sensible and latent eddy heat fluxes are parameterized with traditional bulk formulas (see *Kleeman and Power* (1995) for details). ACOM2 includes an observationally based parameterisation of seasonal light-penetration into the ocean (NASA CZCS data). This allows for a penetration of solar shortwave radiation beyond the first model layer, which has been found to have significant influence on SST.

Wind velocities, relative humidity and cloud cover are input to the ABLM. The main difference between the original ABLM model by KP and our modified version is the use of 3-day mean input data for relative humidity rather than a fixed value of 0.8. Furthermore, we used the simulated evaporation (latent heat) together with precipitation from NCEP to calculate freshwater fluxes. Although NCEP data are frequently used to drive ocean-only models, these model-based fluxes also have significant errors, in particular on sub-monthly timescales. In a recent paper, *Schiller and Godfrey* (2002) investigated the performance of ACOM2 on intraseasonal timescales, but used CDIAC MSU precipitation data and NOAA's OLR as a proxy for tropical solar shortwave radiation, which have been proven to have sufficiently high accuracy on these timescales (e.g. *Shinoda and Hendon*, 1998). The new data significantly improved the near-surface performance of ACOM2 in the Indian Ocean on these timescales. However, intraseasonal variability is beyond the scope of this report and is not further investigated here.

The model was spun up for 20 years from a state of rest. Initial conditions of the three-dimensional temperature and salinity fields were taken from the *Levitus* (1982) climatology. During the first ten years the model was forced with a monthly wind stress climatology based on the blended product described above. During the second decade of the spinup run wind stresses were the blended 3-day mean forcing fields. The spinup was performed with a tight relaxation of SST to monthly mean Reynolds SST (*Reynolds and Smith*, 1994); similarly, sea-surface salinity was relaxed to monthly mean sea-surface salinity (*Levitus*, 1982). Climatologies of the associated fluxes for the last five years of the model spin-up were stored and used as flux corrections in the experimental runs discussed in this paper. The flux corrections of surface heat and freshwater fluxes have a seasonal cycle and are additive values without any dependence on the actual model SST (during the model experiment). This procedure is required because the simple atmospheric boundary layer model produces a flux climatology inconsistent with ocean model fluxes. This approach also guarantees that the model's climatological SST and sea-surface salinity (SSS) are always close to observations. The experiments started in January 1982 and finished in December 1998. 3-day mean fields were stored from the model run. Note that the following discussions about surface heat and freshwater fluxes always include the flux corrections.

As mentioned above, the focus of this study is on mid-to-low latitude ocean dynamics. This uncoupled version of the model does not have an ice model, which limits its reliable physics to areas outside the polar regions.

# 3. LONG-TERM MEAN AND SEASONAL CYCLE

## 3.1 Surface fields

### 3.1.1 Sea-surface temperature (SST) and heat flux

Sea-surface temperature on seasonal-to interannual timescales is determined by horizontal and vertical advection and net surface heat flux. The latter contains a component that allows part of the incoming solar shortwave radiation to penetrate into the ocean rather than being completely absorbed at the surface.

Figure 1 depicts the annual mean SST and their differences with the observation-based Levitus climatology. In the tropics the differences are very small. This would be expected from the seasonal flux correction that has been applied to the surface heat fluxes to keep the model's SST close to observed seasonal climatologies. There are some larger differences, but they are restricted either to mid-latitudes or to western boundary regions where upwelling and strong advection coincide with strong heat uptake by the ocean, in agreement with observations. Due to its coarse resolution ACOM2 does not properly capture these features.

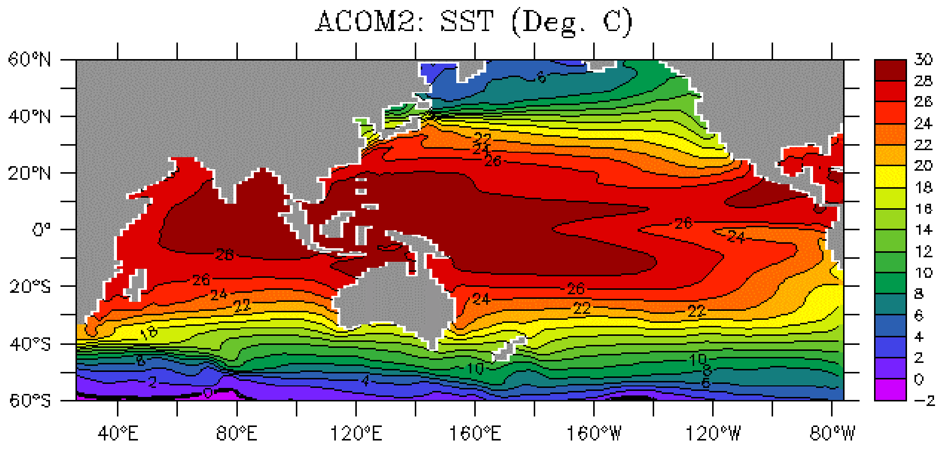

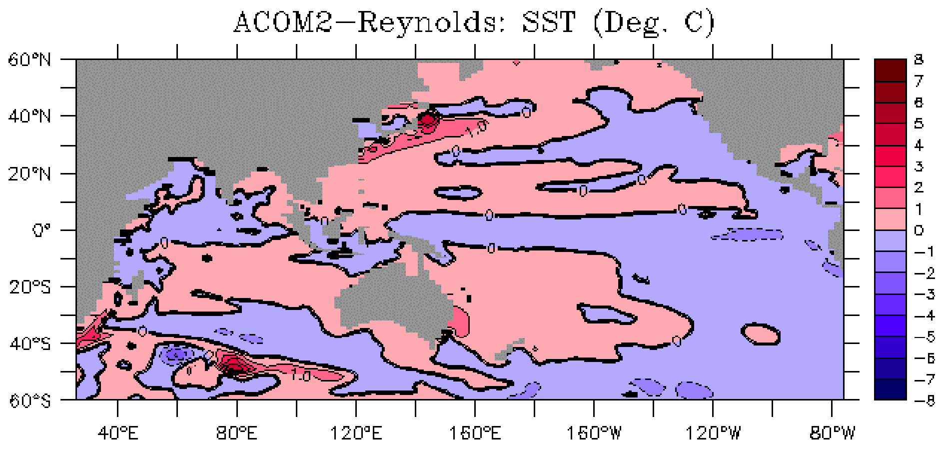

**Figure 1 (previous page): Annual mean sea-surface temperature in ACOM2 (top) and its difference with Reynolds climatology (bottom). Units are in °C.**

Fig. 2a depicts the annual mean net surface heat flux in ACOM2 (the net heat flux is defined as the sum of solar insolation minus latent, sensible and longwave radiative heat fluxes). Apart from the east Pacific, net heat fluxes in the tropics are rather small. The tropical heat uptake by the model is generally too small (i.e. the model 's SST is too cold) compared to the Southampton climatology (Fig. 2b). Note that the differences are about 25 W/m**2 and might be associated with known inaccuracies in observed surface fluxes, particularly solar shortwave radiation. Larger differences occur in the southern subtropics, which might be associated with different wind fields that have been applied to both the model and the heat flux climatology.

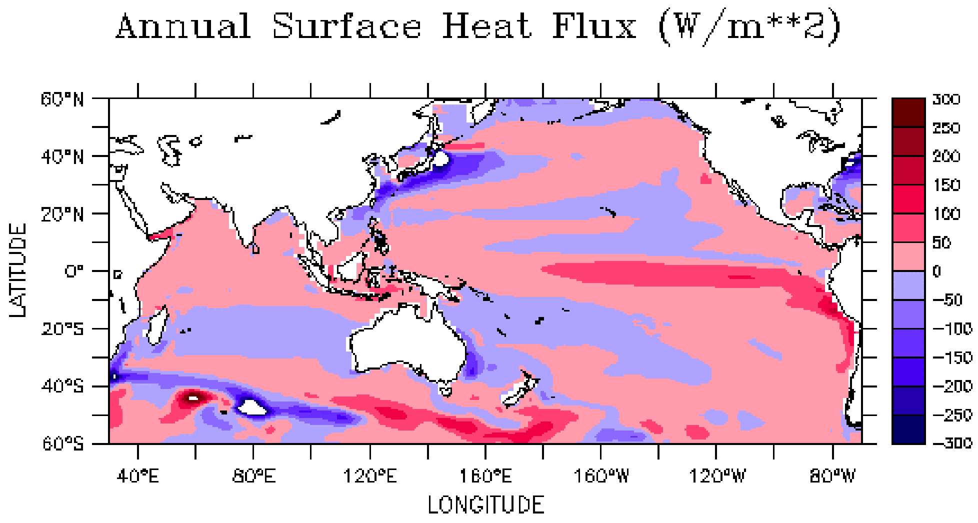

ACOM2

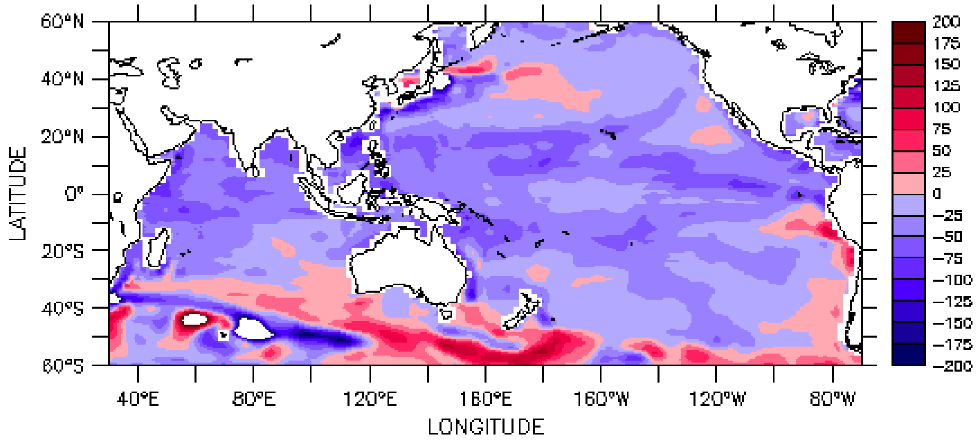

ACOM2 – Southampton

**Figure 2: Annual mean net surface heat fluxes in ACOM2 (top) and difference with the Southampton climatology (bottom). Units are in W/m**2.**

### 3.1.2 Sea-surface salinity

The annual mean sea-surface salinities (SSS) and their difference with the Levitus climatology are shown in Figure 3. ACOM2 reproduces the broad-scale features of high salinity in the subtropics and lower salinities in the tropics and high latitudes. A weak negative bias exists in the model for the southern subtropics and a strong positive bias in regions with strong seasonal precipitation like central America and the Bay of Bengal. The latter problem might be associated with errors in precipitation data used to force the model or due to errors in the Levitus data on smaller scales. The too salty areas also match up well with the too strong cooling fluxes in Fig. 2, such that too strong winds (latent heat fluxes) caused too strong cooling and too much evaporation there.

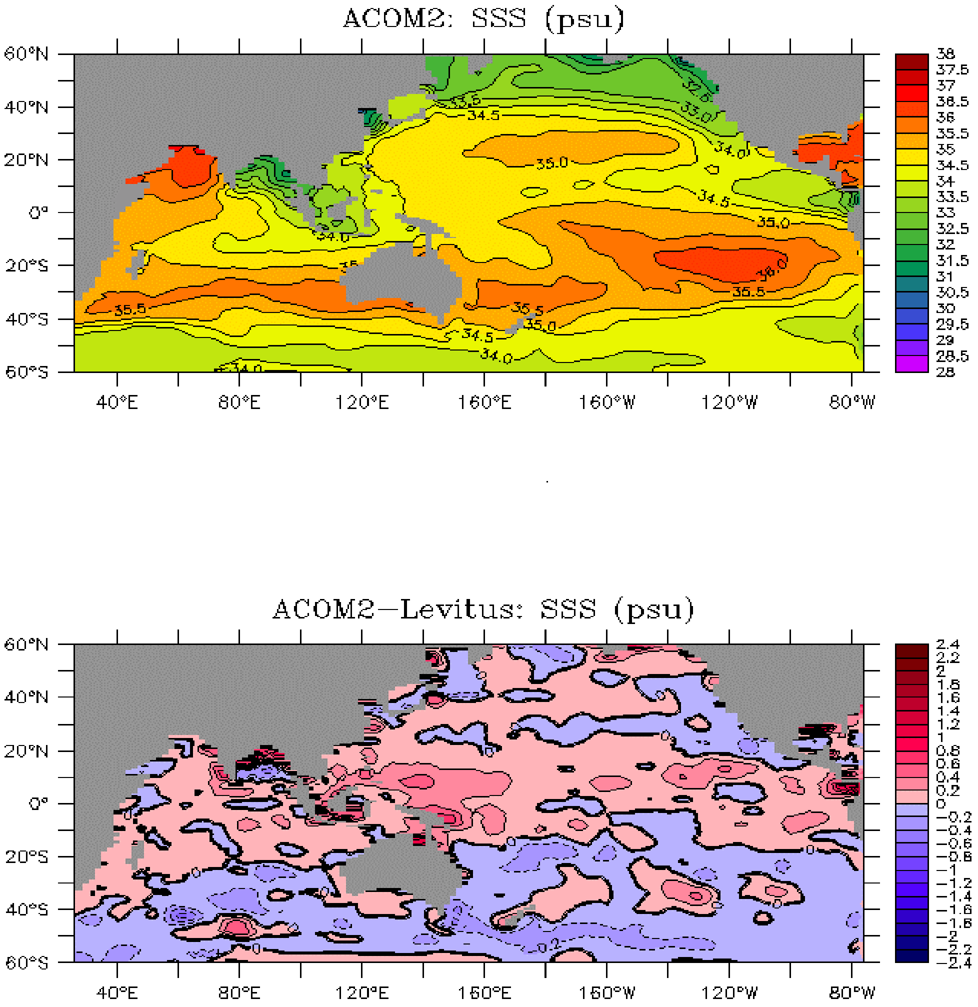

**Figure 3: Annual mean sea-surface salinity in ACOM2 (top) and its difference with the Levitus climatology (bottom). Units are in psu.**

## 3.2. Thermocline properties

### 3.2.1 Depth-integrated steric height

A useful test of ocean models - or more specifically, of the wind stresses used to drive them, at least in a long-term mean sense - is provided by comparing the long-term mean Depth-Integrated Steric Height (DISH) pattern from the model with observation. The Sverdrup relation should hold in both model and reality, and the difference between the Sverdrup and Ekman flows must be in close geostrophic balance with gradients of DISH everywhere in the ocean interior. Furthermore, geostrophic flow towards an eastern boundary must equal Ekman transports away from it, implying longshore gradients of DISH. Suppose all the geostrophic flow is confined above some depth Z, and the above two constraints hold exactly. In that case the long-term mean Depth-Integrated Steric Height relative to the depth Z is determined to within an additive constant throughout the globe, except in western boundary currents. It depends linearly on the applied long-term mean wind stress field, in a way that is independent of all ocean model parameters (*Godfrey*, 1989).

The upper two panels of Figure 4 show that - with the Florida State University wind stresses used here (drag coefficient chosen as 0.0015 everywhere) - the agreement in DISH relative to 1000 db between modelled and observed fields is very close. DISH was taken to be zero at (80° W, 20° S) in both products. The top panel is an average over 1990-1998 from the model output, while the middle panel is DISH evaluated from Levitus (1998) annual mean climatology.

The lower panel shows the difference between the two graphs. The difference is negative at the western sides of each of the subtropical gyres (off Japan, East Australia and South Africa). These small discrepancies could be improved if the drag coefficient were decreased by about 10% at these latitudes. However, on the equator the difference in DISH from Irian Jaya to Peru is about 60 $m^2$ in both model and observations, suggesting that the long-term mean wind stresses are about correct in the equatorial Pacific.

The strongest difference between model and observation lies near 10° N in the Pacific Ocean, where the depth of the trough in DISH to the north of the North Equatorial Countercurrent lies about 2° too far north in the model, and is exaggerated in depth. This is believed to be due to a systematic error in the wind stress field; the FSU product does not capture the details of the very sharp curls at this latitude.

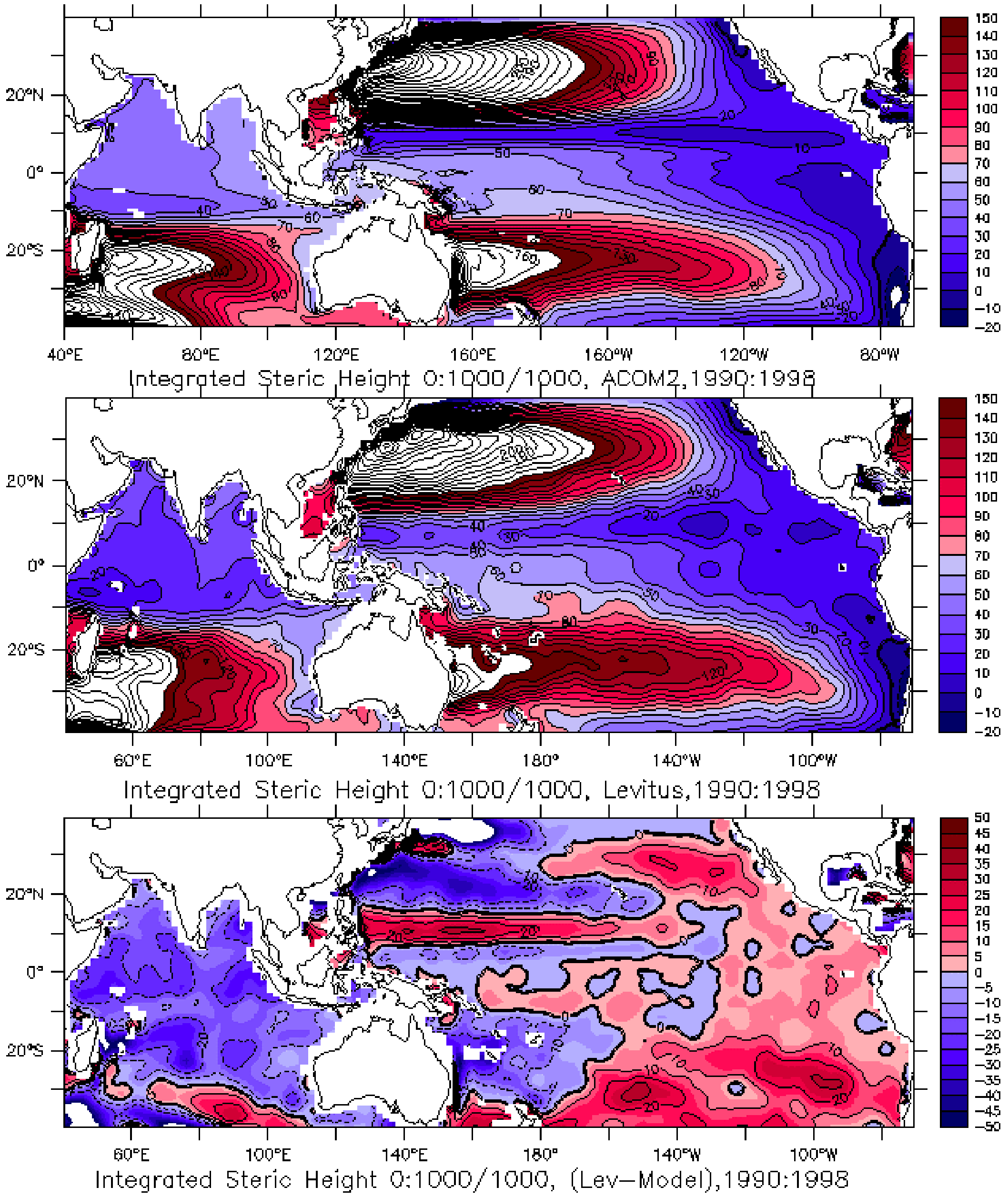

Integrated Steric Height 0:1000/1000, ACOM2,1990:1998

Integrated Steric Height 0:1000/1000, Levitus,1990:1998

Integrated Steric Height 0:1000/1000, (Lev–Model),1990:1998

**Figure 4: Long-term mean depth-integrated steric height from ACOM2 (top), Levitus climatology (middle) and difference Levitus minus model (bottom). Units are $m^2/s^2$.**

### 3.2.2 Depth of 20° isotherm

ACOM2 and Levitus depth of 20° isotherm

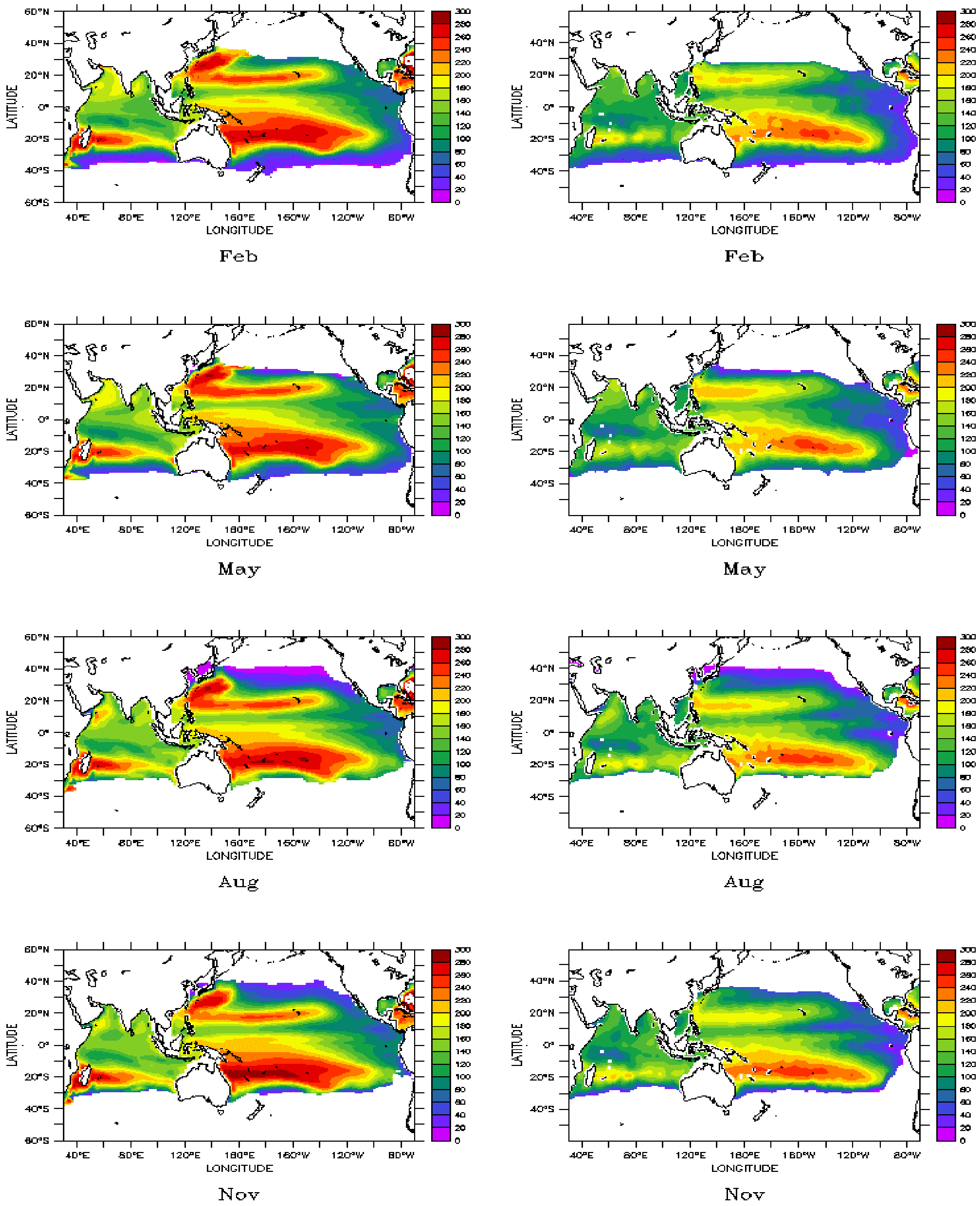

**Figure 5 (previous page): Seasonal cycle of depth of 20º isotherm. Left column: model, right column Levitus data. Units are in m.**

Sub-surface features such as the tropical thermocline can be characterised by the depth of the 20° isotherm (Fig. 5). In both model and observations maxima in D20 coincide with the centers of the subtropical gyres, exceeding 250m. A distinct minima exists in the equatorial Pacific between the North Equatorial Current and North Equatorial Countercurrent where Ekman-induced upwelling lifts D20 to about 180m. Although the model reproduces the observed seasonal cycle in D20, the actual D20 in the model is often more than 50m deeper than observed, i.e. the error in D20 can be as large as its seasonal amplitude. This feature is common to many ocean models; possible reasons are errors in the wind fields and/or the models mixing parameterisation. Note, however, that anomalies of D20 are simulated much more accurately (see section 4.5).

### 3.2.3 Heat content

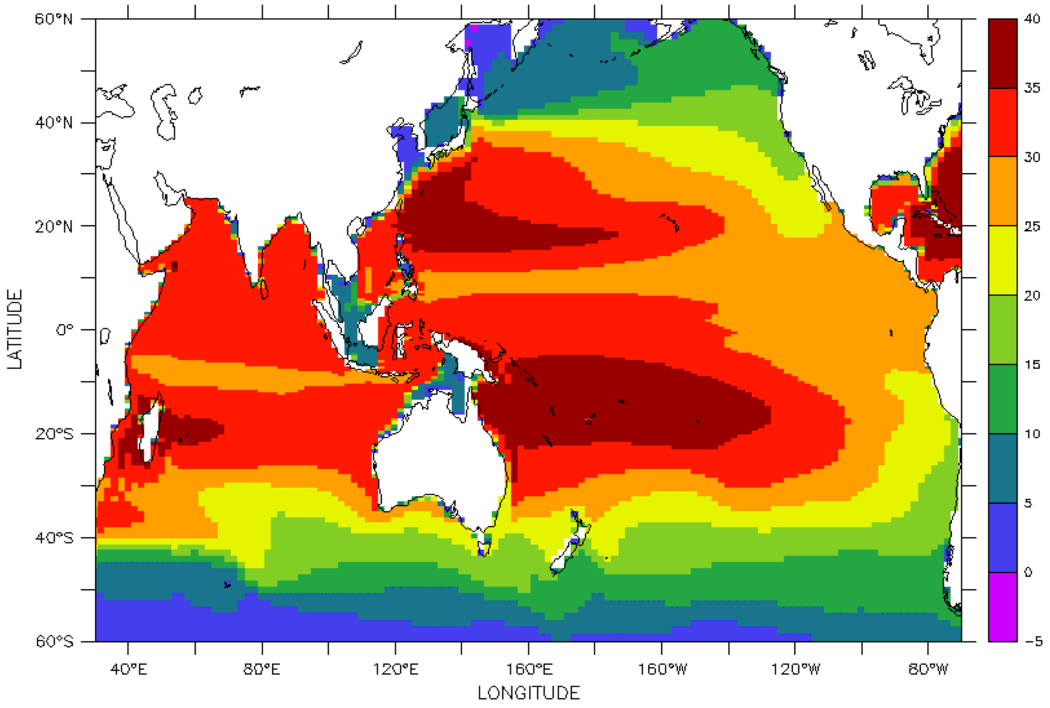

**Figure 6: Simulated annual mean heat content (integrated over top 400m). Units are Giga Joule/ m$^2$.**

The annual mean heat content in the upper 400m (Fig. 6) displays the long-term mean storage of heat in this depth range. The maxima coincide with the centres of the subtropical gyres where downwelling of relatively warm water deepens the thermocline. However, note the marked equatorward displacement of these maxima compared to their analogues in depth-integrated steric height (Fig. 4). These displacements are also seen in observed data (compare the right hand side of Fig. 5 with Fig. 4). Towards the poles reduced annual mean surface heat gain and convective mixing are responsible for smaller values in heat content. This figure serves as a reference for the more interesting seasonal cycle and comparisons with observations (Fig. 7).

The left (right) columns of Figure 7 show the mean seasonal cycle of heat content of the top 400m, from the ACOM2daily run compared to Levitus observations. The latter clearly has a somewhat larger amplitude than the former (we have not at this stage investigated the reasons for this). Nevertheless, both observed and simulated signals reflect significant changes in the seasonal cycle of upper ocean heat storage and dynamics. The four months shown depict the (delayed) influence of the seasons on heat content with negative deviations in the northern hemisphere during February and May (heat loss) and positive deviations in August/November (heat gain). The opposite cycle exists for the southern hemisphere. Two features are prominent in these figures: the eastern Indian Ocean shows a distinct semi-annual feature in upper ocean heat content associated with the occurrence of the Wyrtki jets. In May and November, the Wyrtki jets advect warm water along the equator to the east, causing positive deviations in heat content there. The other interesting feature is the region of the North Equatorial Current in the Pacific Ocean, where deviations from the seasonal cycle are opposite in sign to the heat contents of the surrounding water-masses. Large-scale features of model and Levitus data are in good agreement.

ACOM2 and Levitus Heat Content Deviations (GJ/m**2)

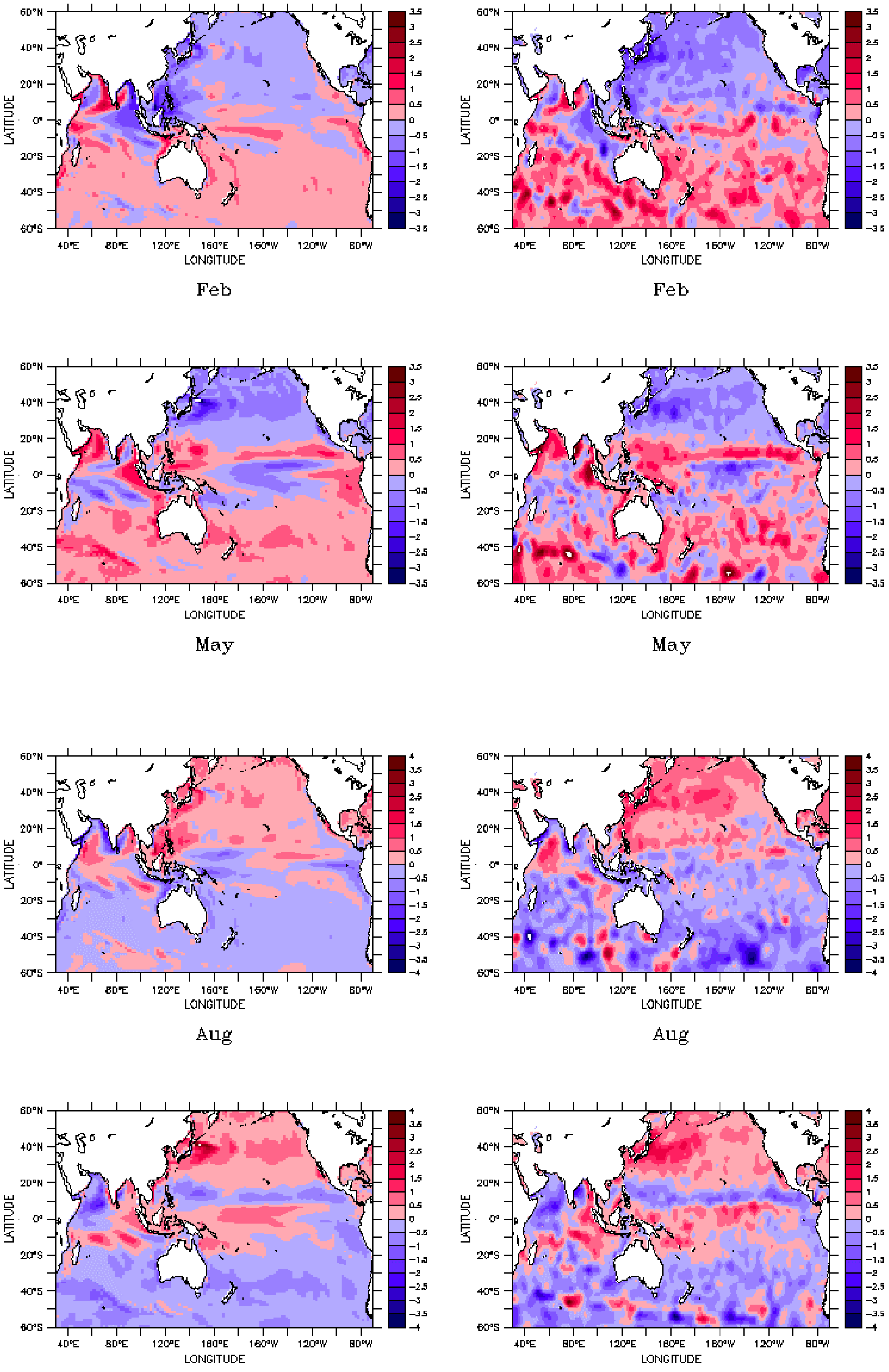

Feb Feb

May May

Aug Aug

Nov Nov

**Figure 7 (previous page): Seasonal cycle of deviations of heat content from annual mean. Left column: model, right column Levitus data. Units are Giga Joule/ m$^2$.**

### 3.2.4 Equatorial details

Equatorial dynamics plays a crucial role in determining Australia’s climate variability, in particular through ENSO. In this section, we focus on the equatorial Pacific, whereas in sections 3.3 and 3.4 we explore the seasonal circulation in the Indian Ocean.

By and large, the simulated thermocline temperature reflects the observations (Fig. 8; Fig. 9 shows the corresponding differences between model and observations). However, there is a systematic warm bias in the model that increases from the central to the eastern equatorial Pacific that reaches 8° C in the latter region between 100m and 200m depth. The thermostad in the eastern Pacific in the model is too weak compared to the Levitus data, where the vertical temperature gradients are smaller. The problem is believed to be associated with inaccurate forcing fields (winds) as well as deficits in model physics (see section 4.7 for further details).

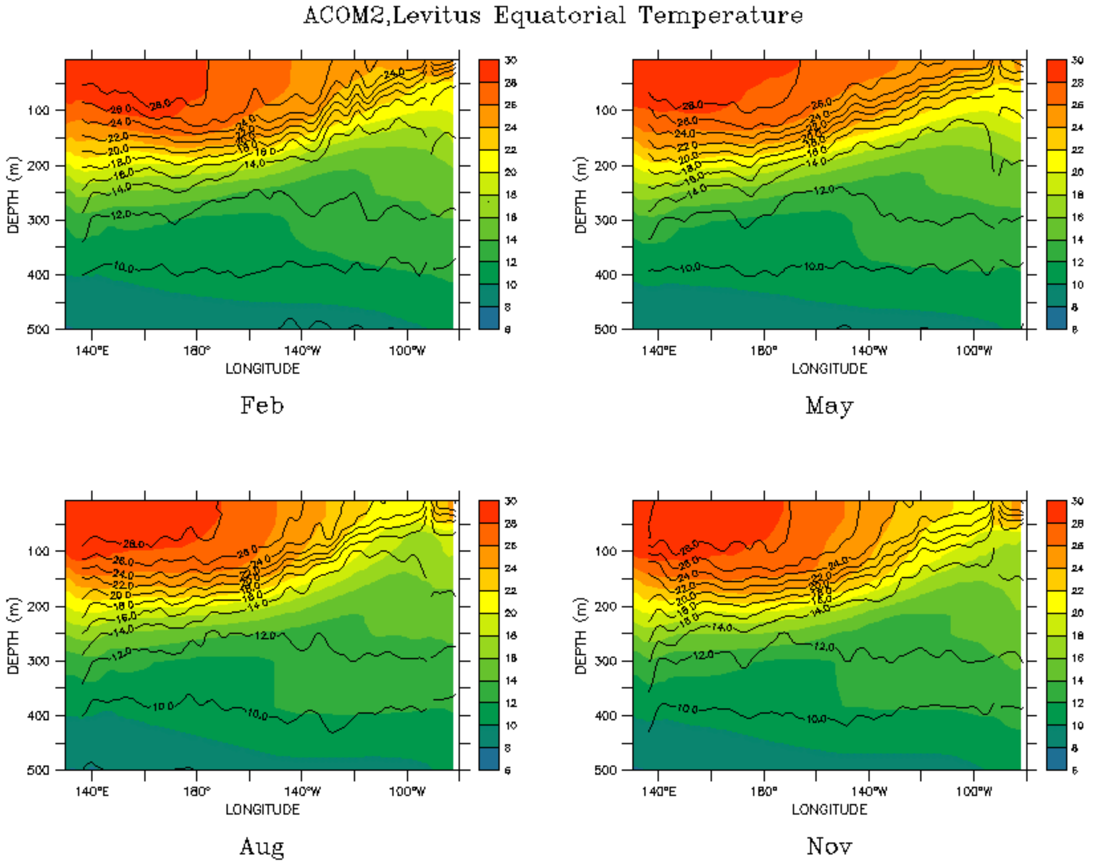

**Figure 8: Seasonal cycle of potential temperature in equatorial Pacific. Shaded: ACOM2, contours: Levitus data. Contour interval is 2° C.**

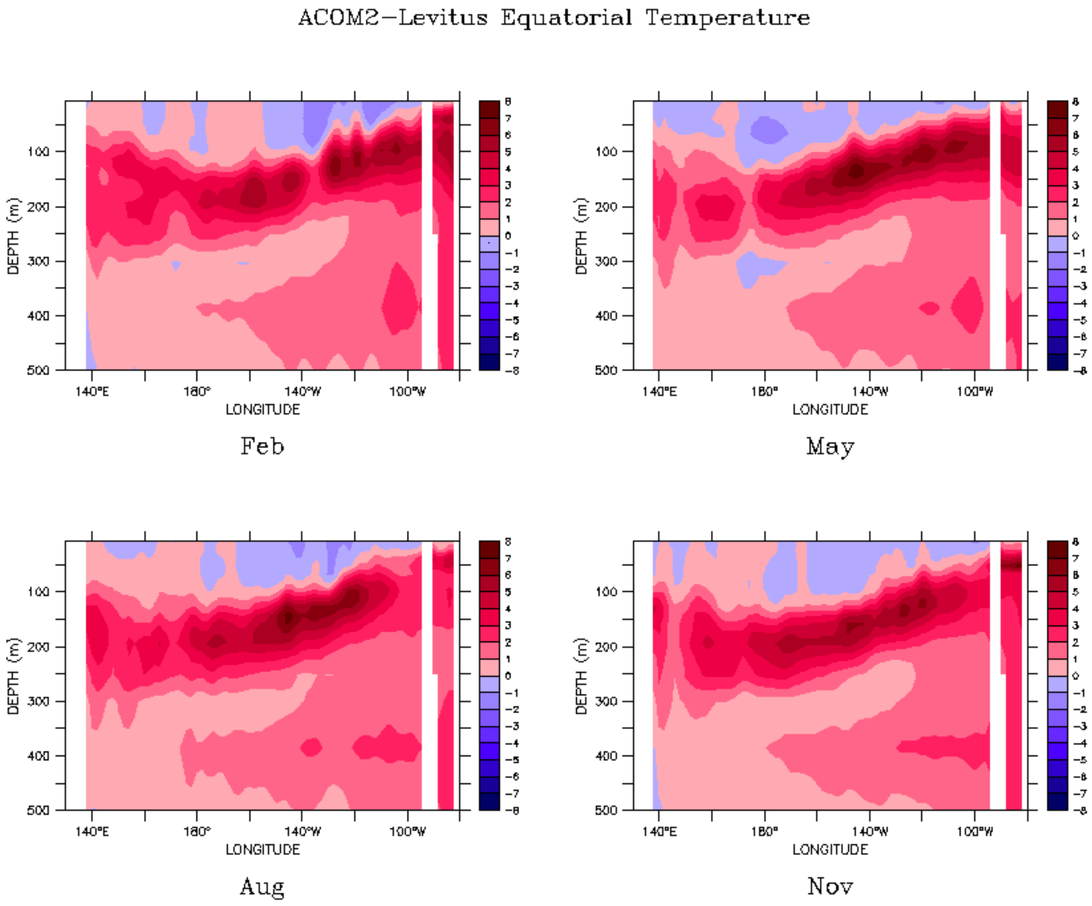

**Figure 9: Same data and region as in Fig. 8, but differences in potential temperature between ACOM2 and Levitus data. Contour interval is 1° C.**

The corresponding Fig. 10 of the seasonal cycle of salinity along the equator shows near-surface minima in the far western and eastern Pacific Ocean. The former is associated with strong rainfall and the latter is caused by coastal upwelling along the American continent and subsequent advection towards the equator. Salinity in the sub-surface Pacific Ocean is characterised by a maximum that extends right across the Pacific at a core depth between 100m and 200m. Simulated and observed salinity features agree reasonably well, although differences are obvious on smaller scales (Fig. 11). Salinity differences are largest in the far eastern Pacific, similar to the temperature differences shown in Fig. 8. In particular, the “tongues” of high salinity water apparently spreading westward and downward from 300m in the east Pacific has no analogue in the observations. Spurious model mixing that might contribute to these model-obs salinity differences is discussed in section 4.7.

The seasonal cycle of zonal velocities from model and TAO observations is shown for the east and far-east Pacific in Fig. 12. Below the surface, the circulation is dominated by the eastward Equatorial Undercurrent (EUC). Note that in the model the EUC is confined to a narrower depth-range with smaller than observed maximum velocities. For most of the year the circulation at the surface at both sites is westward (blue). However, between March/April to June there is a period of eastward flow at the surface. This is not seen in the model and most likely associated with errors in the wind fields (*Schiller et al.*, 2000).

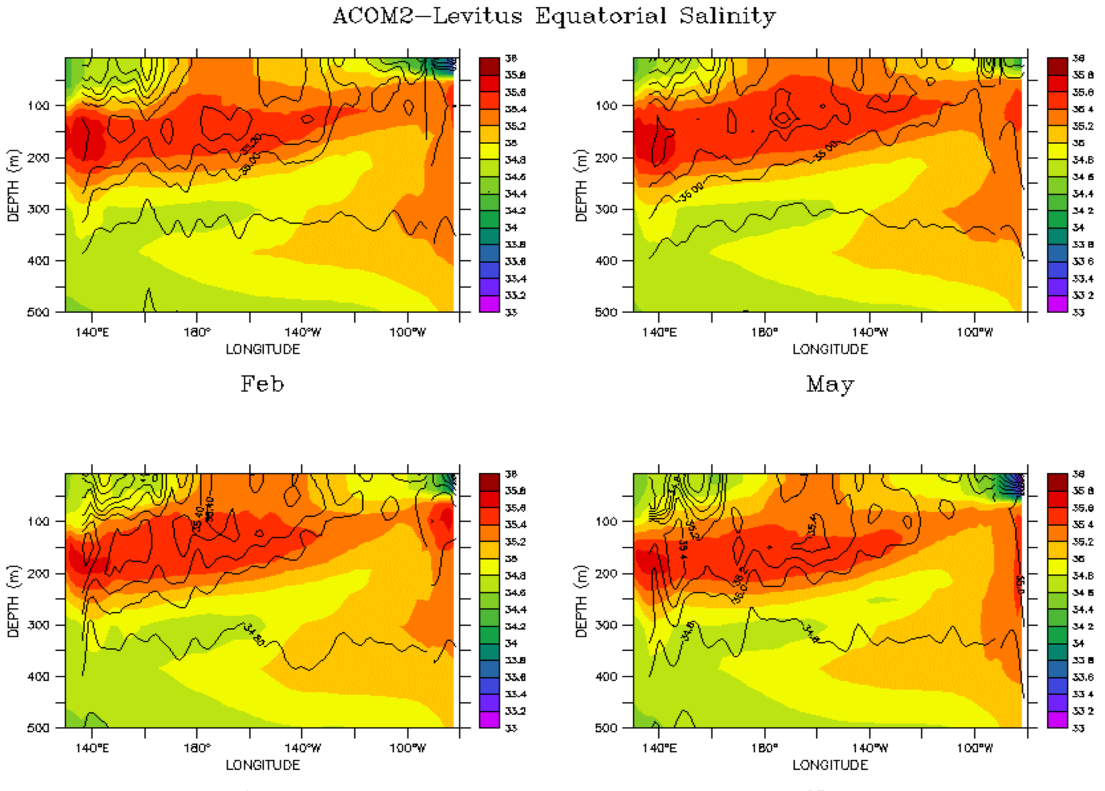

Figure 10: Seasonal cycle of salinity in equatorial Pacific. Shaded: ACOM2, contours: Levitus data. Contour interval is 0.2 psu.

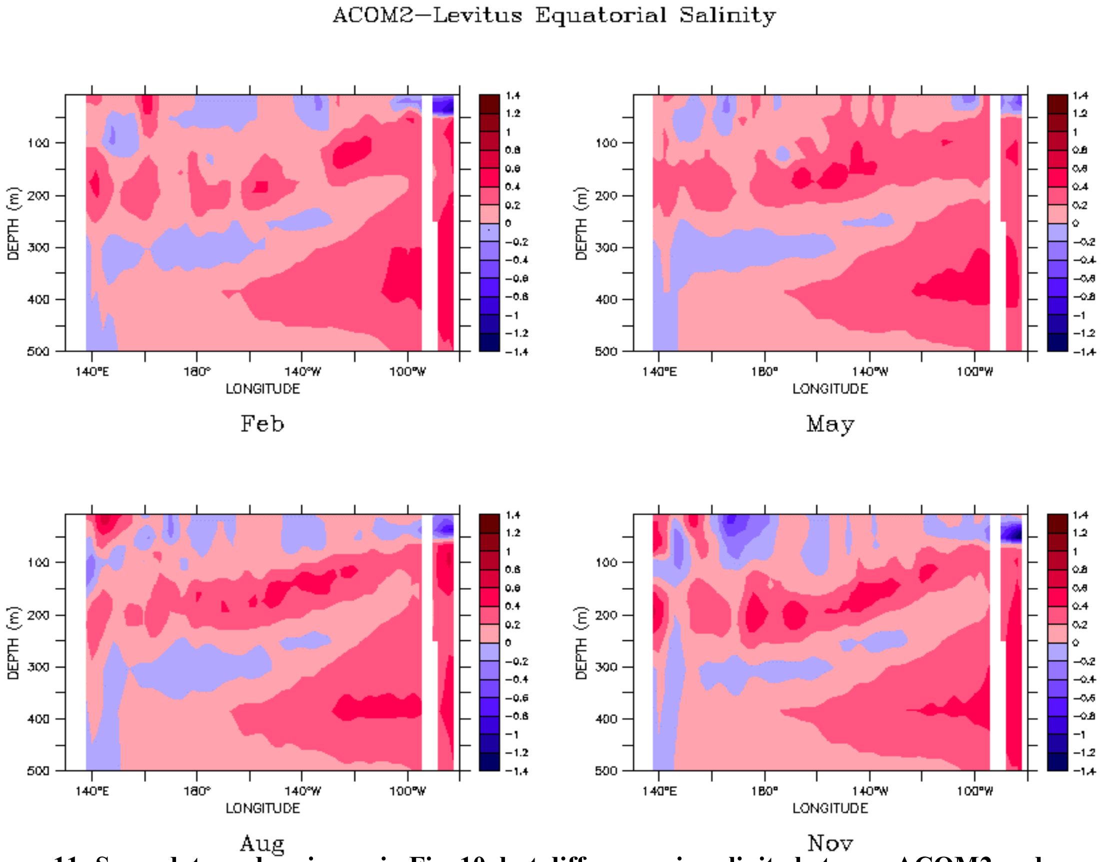

Figure 11: Same data and region as in Fig. 10, but differences in salinity between ACOM2 and Levitus data. Contour interval is 0.2 psu.

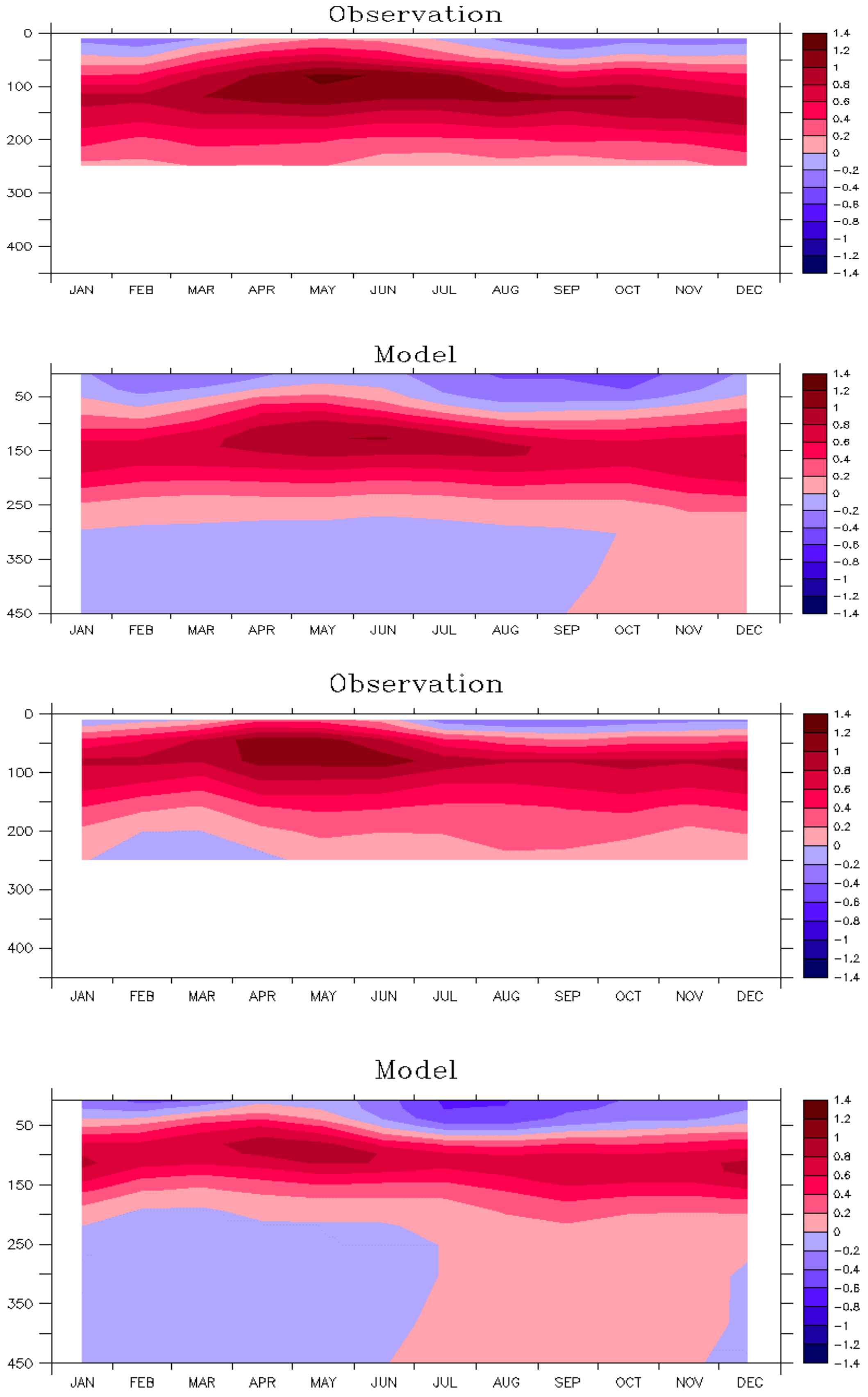

**Figure 12: Seasonal cycle of zonal velocity in equatorial Pacific: 0° N, 140° W (a, b); 0° N, 110° W (c, d). Contour interval is 0.2 m/s.**

## 3.3 Indonesian Throughflow

### 3.3.1 SST and D20 along XBT section IX1

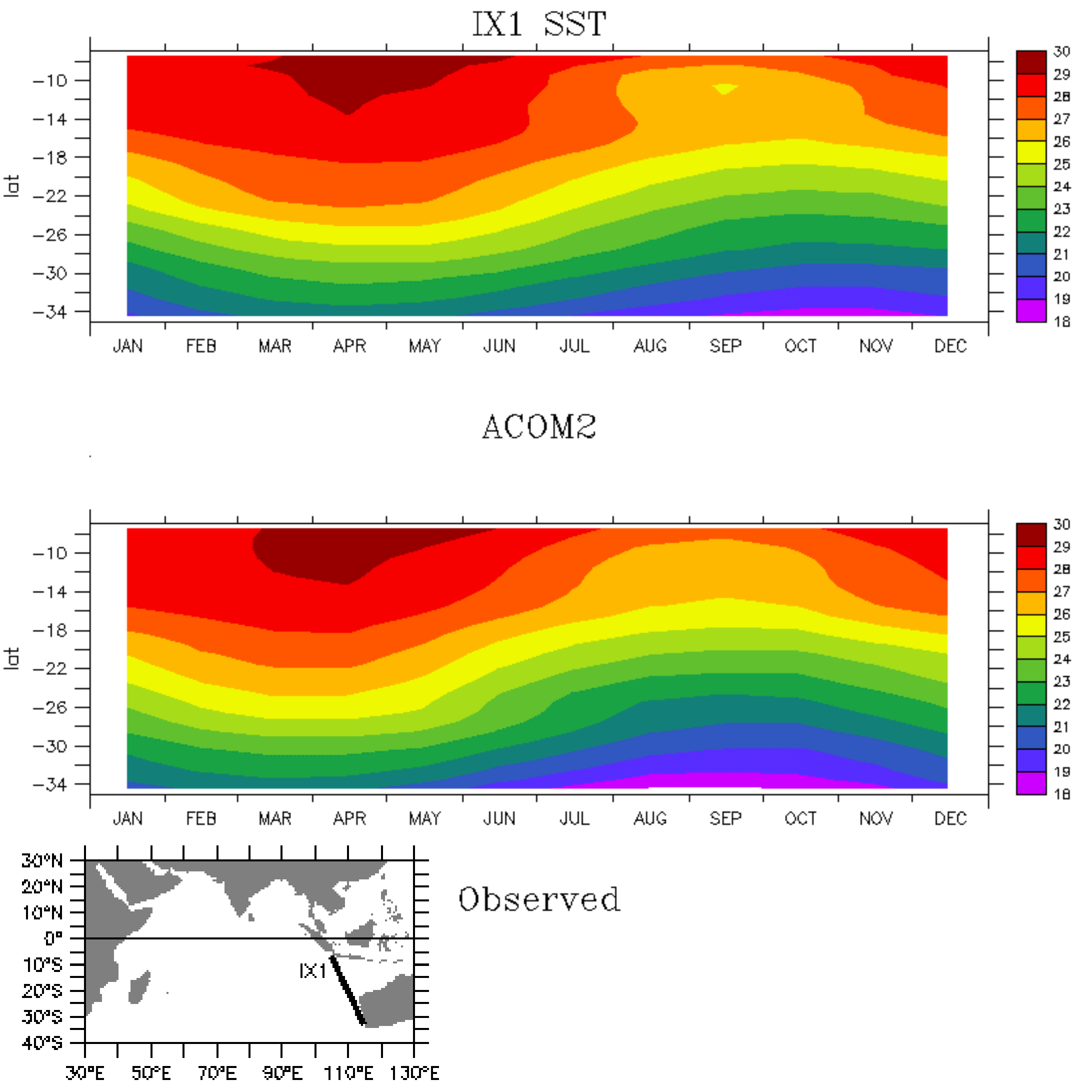

**Figure 13: Seasonal cycle of SST along XBT section IX1. Top: ACOM2, bottom: XBT data (*Meyers and Pigot*, 2000). Units are in °C. Small figure shows location of IX1 section.**

The Indonesian Throughflow (ITF) is a unique feature of the global ocean circulation as it links two oceans at low latitudes, allowing for the exchange of mass, heat and others tracers. Furthermore, the Leeuwin Current off Western Australia is strongly influenced by ENSO-induced variability that propagates through the ITF. In this section we explore some of the basic seasonal pattern of the ITF; section 4.8 addresses its interannual variability. Observed temperature and geostrophic transport estimates have been obtained for the XBT line Fremantle (Australia) to Sunda Strait (Java) as part of the Ship-of-Opportunity Program (*Meyers*, 1996; *Meyers and Pigot*, 2000). Fig. 13 shows a distinct seasonal cycle in SST along XBT section IX1. At its northern end temperatures are close to 30° C and are part of the Indian Ocean warm pool. The southern end of the section crosses the Leeuwin Current; due to heat release to the atmosphere SSTs are much lower there.

In contrast to observations, the simulated D20 shows a much stronger semi-annual component along the coast of Java (Fig. 14). This signal is caused by the South Java Current as an extension to the semi-annual Wyrtki jet along the equator. Most likely, the resolution of the northernmost bins of the XBT data (~1.5° meridionally) are too coarse to capture this signal. On the other hand, the model lacks sufficient horizontal resolution toward the southern end of the IX1 line (2° zonally) to resolve the Leeuwin Current off western Australia. As a result, the simulated D20 near the Australian coast is about 100m deeper than in the observations. In the centre of the XBT section the model by and large reproduces the observed seasonal cycle of D20 with typical differences of 20-30m. Note also the phase shift in the extrema.

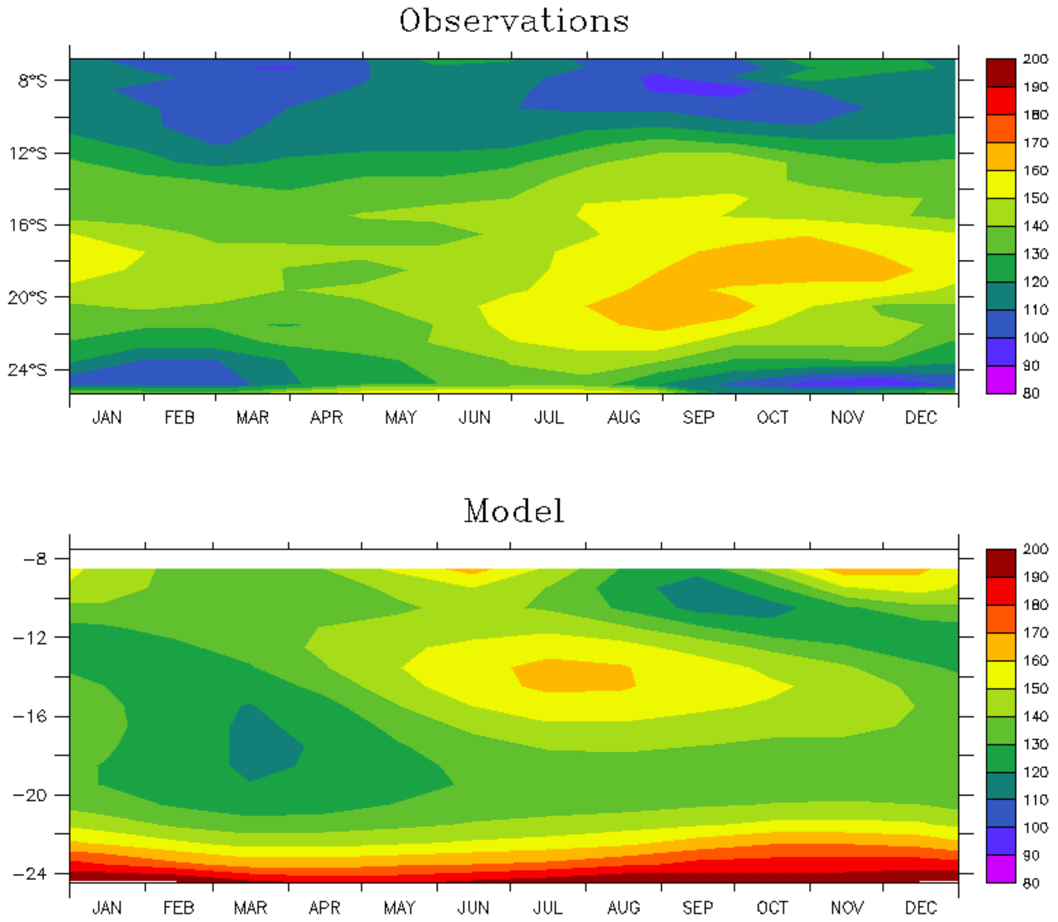

**Figure 14: Seasonal cycle of depth of 20° isotherm (D20) along XBT section IX1. Top XBT data, bottom: model. Units are in m.**

### 3.3.2 Transport along XBT section IX1

On annual mean, the ITF transports warm water from the Pacific into the Indian Ocean Observation-based estimates suggest that the total annual mean throughflow transport is about 5 – 10 Sv (Godfrey, 1996). Fig 15 shows the geostrophic components of the transports between the surface and 400m and 700m, respectively. The phases of both observations and model results show a semi-annual cycle, which appears one month later in the model than in the observations. Minima of the geostrophic throughflow occur in May/June (0-400m) and in April/May (0-700m); the maximum transport is reached in Sep (0-400m) and in July/August (0-700m). A secondary maximum exists in January/February for both transports. Observed and simulated annual mean (0-400m: model –3.9 Sv, obs. -3.2 Sv; 0-700m: model -3.1 Sv, obs. -3.8 Sv) and seasonal amplitudes are in reasonable agreement. Further details of the seasonal throughflow transports are discussed in *Schiller et al.* (1998).

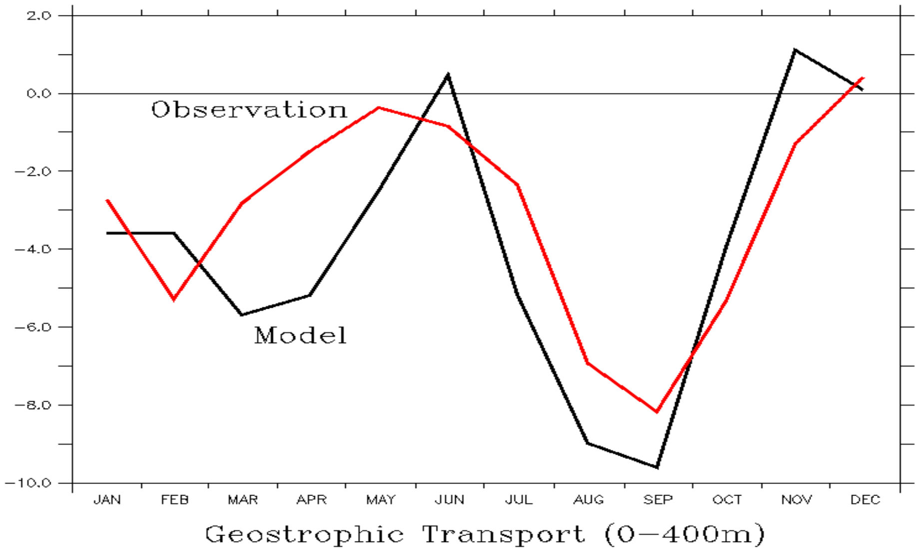

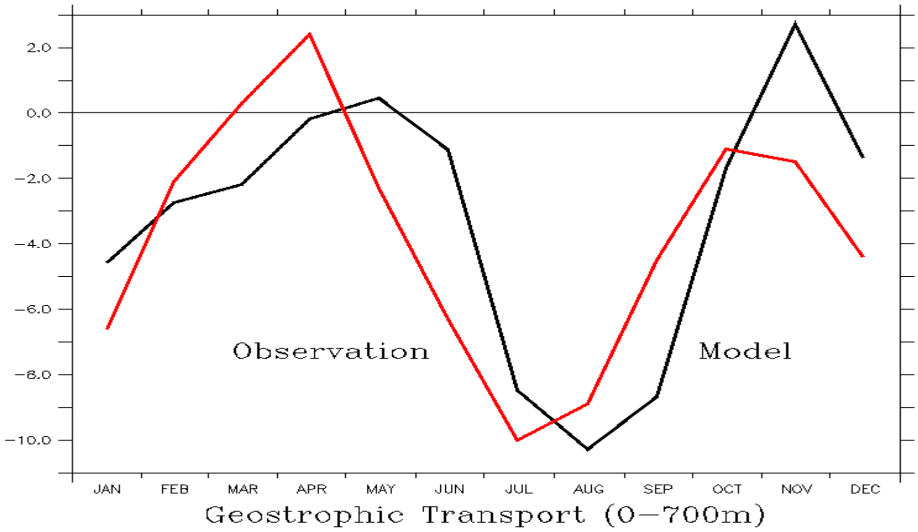

**Figure 15 (previous page): Seasonal cycle of geostrophic transport across XBT line IX1 for model and observations. Top: 0-400m, bottom: 0-700m. Units are in Sv (1 Sv =$10^6 m^3/s$). Negative values indicate flow from the Pacific into the Indian Ocean.**

## 3.4 Indian Ocean: SST and D20 along XBT section IX12

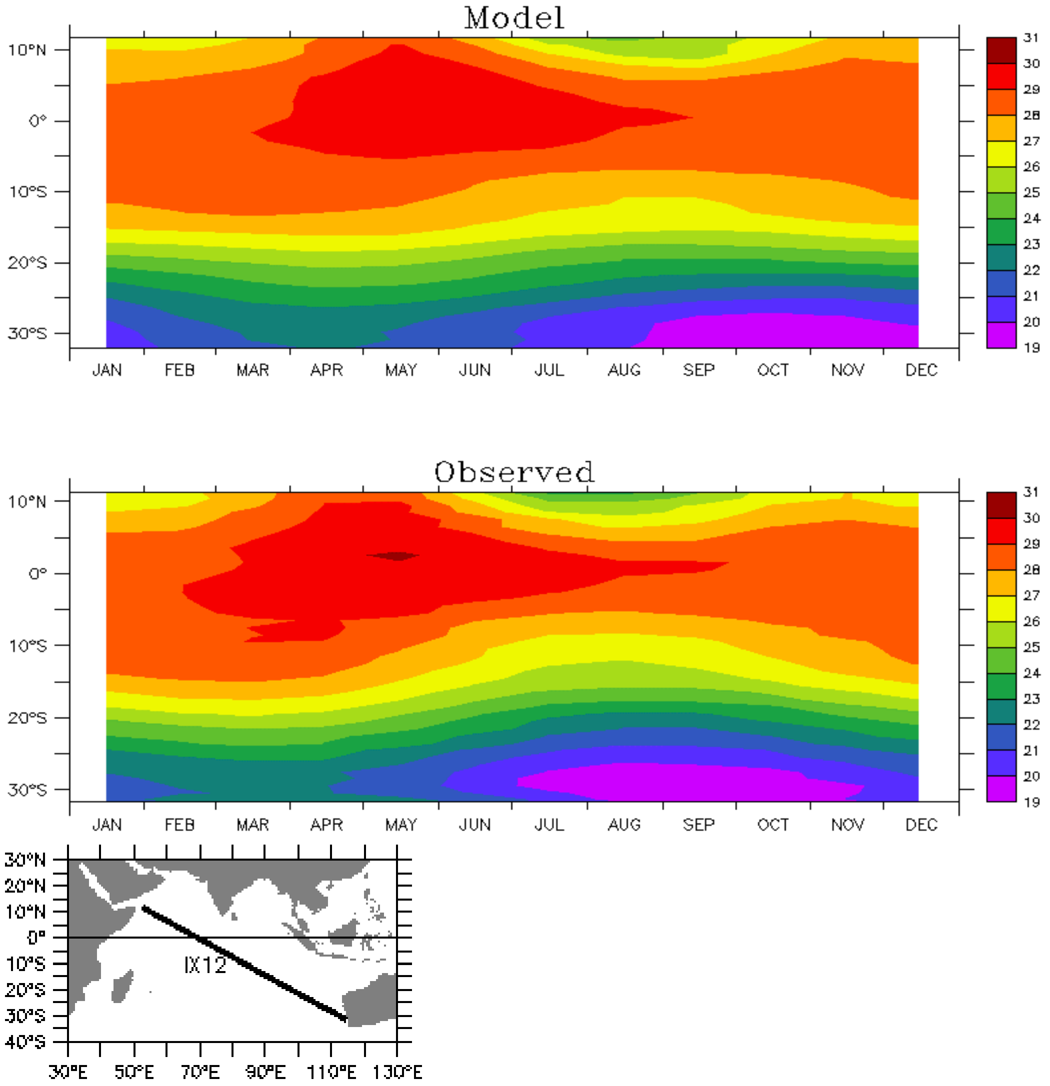

**Figure 16: Seasonal cycle of simulated (top) and observed (bottom, Reynolds data) SST along XBT section IX12. Contour interval is 2° C. Small figure shows location of section IX12.**

The XBT section IX12 crosses the Indian Ocean from Fremantle to the Horn of Africa and touches quite different circulation regimes such as the subtropics in the southern Indian Ocean and the equatorial and western boundary current regions. Therefore, seasonal SST changes considerably along the XBT section IX12 (Fig. 16): in the south the track intersects the cool Leeuwin Current, the equator is crossed at about 70° E at the rim of the Indian Ocean warm pool (T > 28° C). Especially during the Southwest Monsoon upwelling and surface cooling leads to lower SSTs in the Arabian Sea at the northern end of the track. Due to the seasonal flux correction, model and observations are in good agreement.

Simulated and observed seasonal variability of D20 is again quite similar, but the model's amplitude is smaller than observed, in particular at the coastal boundaries of the track (Fig. 17).

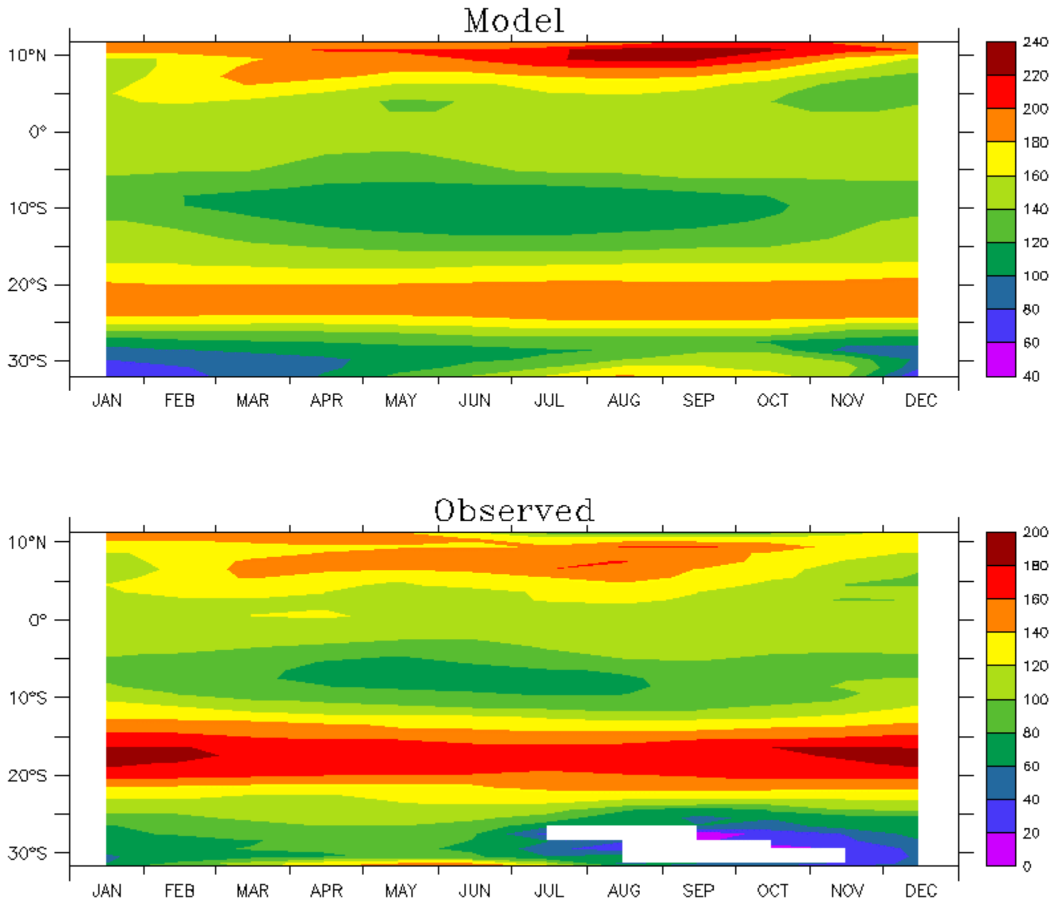

**Figure 17: Seasonal cycle of simulated (top) and observed (bottom, IX12 data) D20 along XBT section IX12. Contour interval is 20m.**

# 4. INTERANNUAL VARIABILITY

Direct observations are available for the global fields of sea level and SST, over nearly one and two decades respectively; these provide two tools for assessing the performance of the ocean model, when driven with an “observed” set of surface fluxes. We discuss these two ways of testing the model below. It is generally assumed that sea-level variability is mainly determined by known linear wave motions forced by wind stress, with other surface forcings (heat and freshwater fluxes) playing a relatively minor role (e.g. *Busalacchi and O’Brien*, 1980; *Kessler and Mc Phaden*, 1995). However, results shown in this report show that changes on small spatial scales can change the behaviour of the ocean on long time scales, even for sea-level. SST anomalies (SSTAs) additionally depend on all surface forcings, and are even more difficult to interpret. We therefore examine the model simulation of sea-level first, to extract as much information as we can before examining SST dynamics.

## 4.1 Correlation of observed and modeled sea-level anomalies

### 4.1.1 Local correlations of observed with modelled anomalies

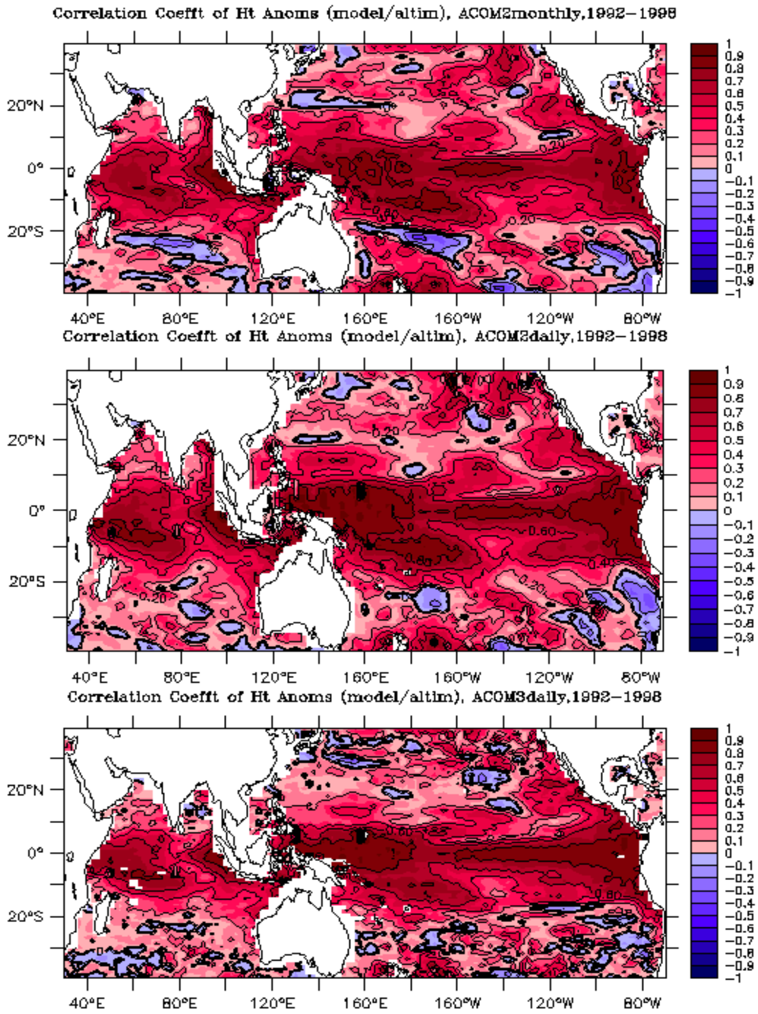

**Figure 18 (previous page): Each panel shows a map of the local correlation of seasonal anomalies of sea-level from a model run, with data from Topex/Poseidon observations (1992-1998). Model sea-level is taken as surface steric height relative to 500 db. The models are: a) ACOM2, driven with monthly mean FSU wind stresses with a drag coefficient 0.0015 (ACOM2monthly). b) ACOM2, run with winds as above except intramonthly wind variations added from the NCEP reanalysis data (ACOM2daily). c) ACOM3, run as in b) above (ACOM3daily).**

Figure 18 shows 3 maps of the correlation of model-generated anomalies in surface steric height relative to an assumed "depth of no motion" at 500m, with observed sea-level anomalies from Topex-Poseidon at the same point. The mean seasonal cycle has been removed from each timeseries, and the resulting anomalies are correlated over the period 1992-1998 common to the three runs used, and to the Topex-Poseidon data set. The correlations in Figures 18a,b,c show respectively the results from ACOM2 with monthly mean winds; ACOM2 with 3-day mean winds; and ACOM3 with 3-day winds. As anticipated, all three models perform well in the tropical strip of 10° S-10° N, with average correlations over this region of more than 0.6; they exceed 0.8 in places. Poleward of this tropical strip, correlations decrease markedly, to statistically insignificant values. Particularly west of South America in Figure 18b, the regions of negative correlation have a shape reminiscent of Rossby wave propagation. This may reflect a model problem; Ridgway (pers. comm.) has found prominent Rossby-wavelike features near 20° S in Pacific altimeter data. The pattern of errors at these latitudes is consistent with what might be expected if the model gave a wrong value for the westward speed of these waves. However, at the time of writing we have not been able to check this idea.

Fig. 18 shows that all 3 model products perform poorly near (10° N, 120° W) — substantially closer to the equator than the errors referred to above. This region lies at the eastern end of the Intertropical Convergence Zone, and wind stress climatologies (e.g. *Wyrtki and Meyers*, 1975) show that the winds have quite intricate variations on short length scales near here, due to strong winds through gaps in the Central American mountain chain (*Kessler*, 2002). These features will not be well-resolved by the sparse shipping traffic that provided the principal source for the FSU wind product; nor will they be well-modelled by NCEP. It is thus likely that the error is due to a problem with the wind product used. A similar problem was seen in connection with Fig. 4c. In general, correlations in Figure 18 are weaker all along 10° N than along 10° S, in the Pacific.

Comparison of Figures 18a and 18b shows that inclusion of 3-day mean winds markedly improves the correlation between modelled and observed sea levels. This is certainly true in the tropics, where the regions with correlations greater than 0.8 increase considerably in area. It appears to be true also at higher latitudes, though in this region the improvement does not alter the generally insignificant values of the correlations. Note that this is not due simply to having higher time resolution in both model and observations; the monthly means of the two runs with submonthly forcing are compared to observed monthly mean sea level anomalies.

Comparison of Figures 18b and 18c shows that use of the finer-resolution ACOM3 model makes very little difference to the correlations. Thus it seems that within the tropical strip, the primary limitation on model performance in simulating observed sea-levels is probably the quality of the wind stress product used.

There is a possibility that the correlations might be increased with the use of monthly mean winds, if the product were more faithful to "reality" than the FSU winds are. However, most available observational data — such as that from the Pacific TAO moorings — have already been used in creating the FSU winds, so such data usually cannot be used to test the accuracy of FSU winds. One exception is a mooring at (0° N, 80.5° E) south of Sri Lanka, in 1993-1994; we have compared FSU and mooring monthly mean wind stresses for the year of deployment (not shown). The TAO winds have been extrapolated to 10m height with a logarithmic profile, and both FSU and TAO stresses calculated with a drag coefficient of 0.0015. The differences are of the same order as typical interannual wind stress anomalies, indicating fairly substantial errors in FSU winds in the equatorial Indian Ocean.

A run is planned with a new wind stress product, based on data from the ERS1 and ERS2 scatterometers. This has, for example, revealed a patch of positive wind stress curl just north of the equator in the east Pacific, that had not previously been detected (*Kessler et al.*, 2001); it substantially increases the eastward flow in the Equatorial Undercurrent compared to previous products. We anticipate revisiting Figure 18, using model runs driven with this new stress product.

Regressions of model on observed height anomalies (similar to Figure 18; not shown) are typically very similar to the correlations of Figure 18, except in the tropics. Here regressions are somewhat greater than the correlations and they slightly exceed 1 in a few places, suggesting that the models are slightly overestimating the amplitude of the observed sea level anomalies.

### 4.1.2 Regressions of observed and modelled sea-level anomalies with NINO4 SSTs

The principal mode of global climate variability is due to the El Niño phenomenon, and a good index of this is the SST anomaly averaged over the equatorial mid-Pacific (5° S-5° N, 160° E-150° W), known as the “NINO4 Index”. We use NINO4 because this index correlates somewhat better with Australian rain than does the better-known NINO3 index, which uses the larger SSTAs found further east. Comparisons of the regressions of observed and modelled sea-level anomalies with the NINO4 index provide a good test of the model — and/or the ENSO-related wind stress variations used in driving the model — in simulating the ENSO mode of variability in sea level.

Figure 19b shows the regression of observed sea-level anomalies on NINO4 SSTs. The contour interval is 2 cm/1°C. Features seen in the equatorial Pacific are qualitatively much as one would expect, given that ENSO events are characterised by strong westerly wind anomalies in the western and central equatorial Pacific. Sea-levels are observed to rise in El Niño events along the equatorial Pacific east of the dateline; this rise has its maximum on the equator, falling off somewhat faster north of the equator than south. The width of this region is nearly 10° — rather wider than a Kelvin wave width of about 7°. Wings of positive sea level/NINO4 regression spread poleward along the west American coast, qualitatively as expected from the poleward propagation of coastal Kelvin waves. In the western equatorial Pacific, regions of reduced sea-level are seen with maximum amplitude at about 5° N and 5° S, with a pattern similar to that due to a first meridional mode, first vertical mode Rossby wave. A maximum of sea-level reduction is seen in the Indonesian seas. The reduced sea-levels propagate into the Indian Ocean via the Indonesian gap; sea-levels are reduced along the western Australian coast,

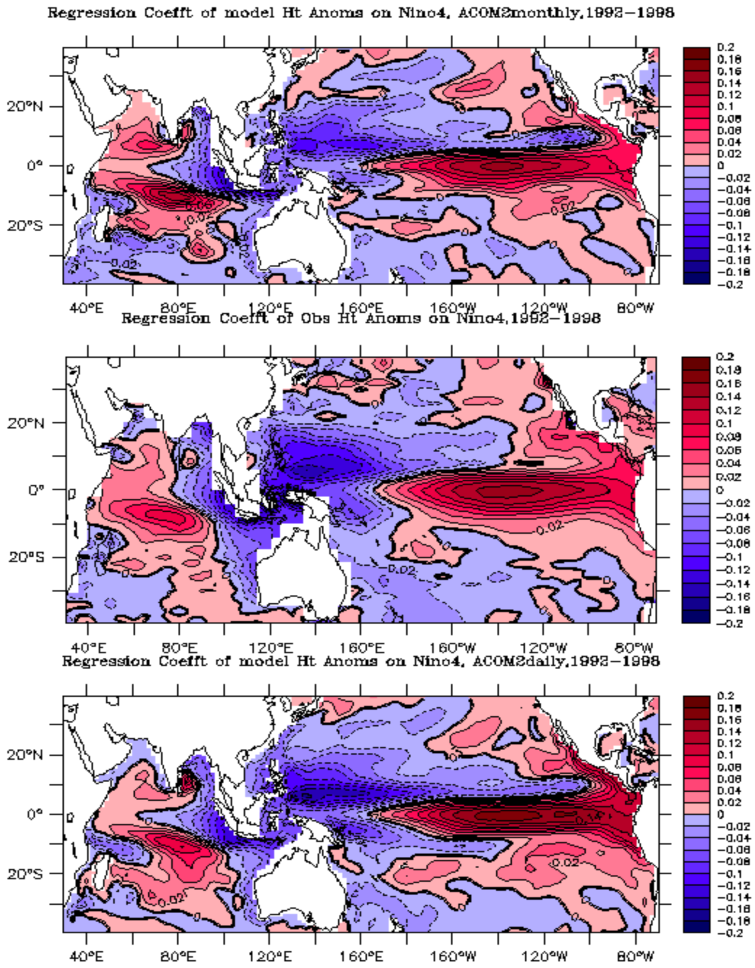

**Fig. 19: Regression coefficient of height anomalies on SSTA, averaged over the NINO4 region (5° S-5° N, 160° E-150° W). The central panel (19b) is for observed height anomalies from Topex-Poseidon; the upper and lower panels (19a,c) are for steric height relative to 500 db, from ACOM2monthly, ACOM2daily respectively. Contour interval is 2 cm/°C.**

as expected from Kelvin wave propagation along that coast (e.g. *Godfrey and Golding* 1981, *Clarke and Liu* 1994). Sea-levels also fall along the Indonesian coast; this is also expected, since ENSO events are accompanied by easterly wind stress anomalies along the eastern equatorial Indian Ocean as well as westerly anomalies in the central Pacific. The former wind anomalies drive upwelling Kelvin waves in the eastern Indian Ocean and along the south Indonesian coast. In the central Indian Ocean — particularly at 10° S — sea-levels rise in an ENSO event; this might also be ascribed to ENSO wind anomalies, if they generated downward Ekman pumping curl($\boldsymbol{\tau}$/f) at these longitudes. Sea-levels also fall throughout most of the South Pacific, and the southwest Indian Ocean.

Figures 19a,c show the regressions of modelled sea-level anomalies on the NINO4 index, from runs with FSU monthly winds and the same winds with daily variations interpolated from the NCEP wind stress product. Both model runs (and especially Figure 19c, with daily winds added) are remarkably successful in simulating the large-scale features of observed regression coefficients, both in spatial pattern and amplitude. A particularly surprising feature is the degree of agreement, feature by feature, between the patterns of Figures 19b and 19c poleward of 20° in all three oceans — North Pacific, South Pacific and South Indian. However, closer inspection reveals several important discrepancies.

- At 5-10° N and near 10° S in the Pacific, Figures 19a,c show bands of reduced sea level that are not present (or are markedly weaker) in the observed pattern, Figure 19b.

- The model results show a sharp “nose” of negative correlation protruding westward along the equatorial Indian Ocean, that is not nearly so pronounced in the observed pattern of Figure 2b. There is also enhanced occurrence of positive regressions near (10° S, 80° E) and near (7° N, 65° E) compared to Figure 19b. These three events are all consistent with the interpretation that ENSO-related easterly wind anomalies in the east and central equatorial Indian Ocean are overemphasised in the FSU wind product, compared to “reality”. Inclusion of NCEP daily winds somewhat ameliorates this effect; note the more realistic amplitudes of sea-level regressions near (10° S, 80° E) and near (7° N, 65° E) in Figure 19c, compared to Figure 19a. This issue can again be explored with a run using the satellite-based winds.

- The minimum sea-level anomaly in Indonesia is absent from the two model results. This result might be due to problems with interpreting altimeter data in the island-studded Indonesian region, but it might be worth checking against steric height data from XBT lines to see if such features are seen in these data also.

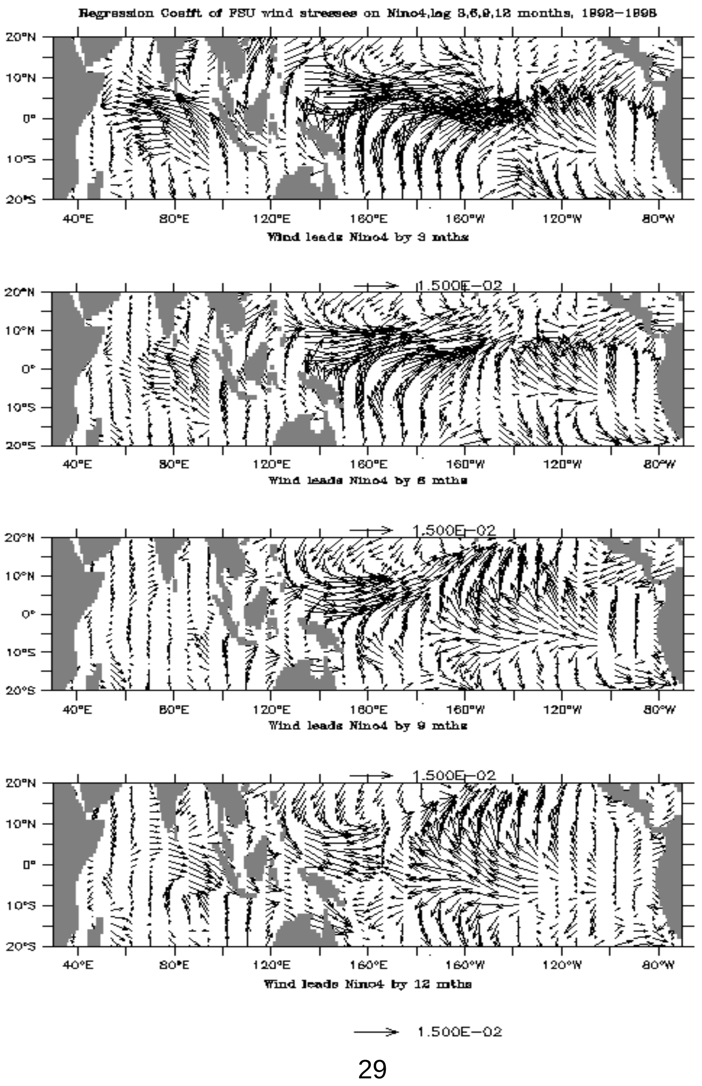

**Fig. 20 (previous page): Vector regressions of wind stresses on NINO4 SSTA, for stresses leading NINO4 by 3,6,9,12 months. The scale vector is 0.0015 N/m$^2$/°C.**

Simple linear theory suggests that errors in Figures 19a,c relative to Figure 19b are likely to be due to persistent errors in Ekman pumping due to the wind products used, relative to "reality". While we do not know what "reality" is, we have sought clarification for these features by forming the regression of the FSU wind stress anomalies we used on the NINO4 index (Figure 20), at lags of 3,6,9 and 12 months prior to the NINO3 index (lag increasing downwards). The figure uses data from the same period (1992-1998) used in Figures 18 and 19. Strong wind stress anomalies are seen in the east Pacific near 10° N, associated with strengthened Trades crossing central America, for 9 months prior to the maximum of an El Niño event. Similarly, strengthened Trades are seen in the east equatorial Indian Ocean for 6 months prior to the maximum of an El Niño. It is possible that these features are not adequately represented in the FSU product; for example, no major shipping lane comes near (10° N, 120° W). Too-strong Ekman divergences in the FSU data set could account for the first dot point above, and paucity of shipping data might also explain the second dot point. Study of satellite wind data will be useful for exploring such issues, as indicated in *Kessler* (2002).

## 4.2 Correlations of observed and modelled SST anomalies

### 4.2.1 Local correlations of observed with modelled SST anomalies

Figure 21 is the equivalent of Figure 18, except that the correlations are now between modelled SST anomalies (SSTAs) and those from the Reynolds data set at the same spot (*Reynolds and Smith*, 1994). The timeseries are all limited to the same period, 1992-1998, shown in Figure 18. Figure 22 shows the same correlations, evaluated for the entire 17-year duration of each run, 1982-1998.

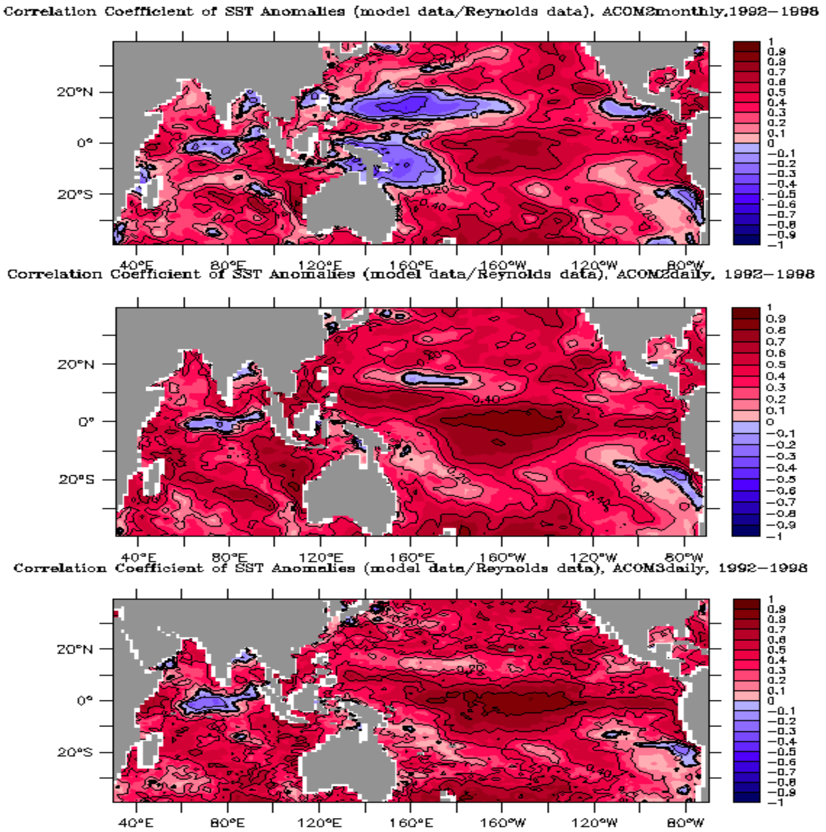

Correlation Coefficient of SST Anomalies (model data/Reynolds data). ACOM2monthly,1992–1998

Correlation Coefficient of SST Anomalies (model data/Reynolds data), ACOM2daily, 1992–1998

Correlation Coefficient of SST Anomalies (model data/Reynolds data), ACOM3daily, 1992–1998

**Figure 21 (previous page): As for Figure 18, except that each panel shows correlations of model SST anomalies with observed (Reynolds) SST anomalies, for the period 1992-1998.**

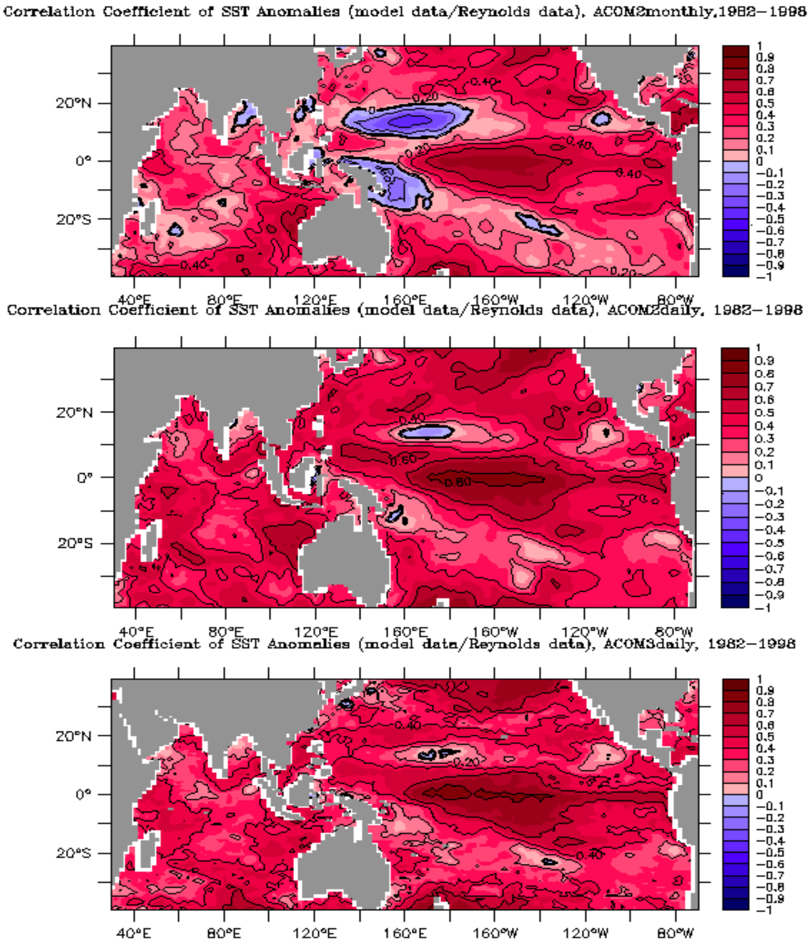
Correlation Coefficient of SST Anomalies (model data/Reynolds data). ACOM2monthly,1982–1998

Correlation Coefficient of SST Anomalies (model data/Reynolds data). ACOM2daily, 1982–1998

Correlation Coefficient of SST Anomalies (model data/Reynolds data), ACOM3daily, 1982–1998

**Figure 22: As for Figure 21, but covering for the period 1982-1998.**

A region of negative correlation can be seen in all 3 panels of Figure 21 in the equatorial Indian Ocean that is absent in Figure 22. A second such region is seen near 20° S off South America. We will discuss these features later. Apart from this, Figures 21 and 22 are very similar, implying that the local correlation patterns are quite stable with time, as discussed by (e.g.) *Reason et al.* (2000). Comparison of Figures 21 and 22 with the corresponding panels of Figure 18 shows that the correlations in the tropical strip are everywhere lower for SSTA than for sea-level anomaly. One striking difference is that Figure 21a and 22a show large regions in the western Pacific and central Indian Ocean where SSTA correlations are in fact negative; there is no analogue in Figure 18a.

However, comparison of Figs 21a, 22a with Figs 21b, 22b shows that SSTA correlations are higher virtually everywhere when 3-day winds are included, especially for the period 1982-

1998. Thus wind variability on timescales of a month or less (omitted in Figures 21a, 22a) seems to play a major role in setting SST throughout the tropics (and at higher latitudes). Unfortunately there is little prospect of these short timescale wind effects ever being “forecastable” on timescales longer than a few weeks. It may therefore be that Figures 21a, 22a are better representations of the likely patterns of SSTA predictability, with the best coupled models. However, we have not explored the possibility that simply adding intraseasonal variability with the right RMS amplitude (but no attention to phase) may improve the correlations.

One further point to be made with regard to Figures 21 and 22 is that the correlation pattern with 3-day winds from ACOM3 (Figure 21c, 22c) is not very different from that in Figure 21b, 22b. It would thus seem that substantially higher grid resolution in ACOM3 does not strongly affect the ability of the model to simulate observed large-scale patterns of SSTAs in the open ocean, when both models are driven with the same flux product. However, the subsurface climatologies of the ACOM2 and ACOM3 models (the latter are not shown here) are quite different, which could affect the rate of drift of each model when coupled to the same AGCM. Thus the similarity of Figures 21b, c and 22b,c does not imply that ACOM2 and ACOM3 will perform similarly in coupled models.

We do not know the reasons for the region of negative correlations in the central equatorial Indian Ocean in all three panels of Figure 21. However, we note that the Indian Ocean appears to have been more active from 1992 onwards than from 1982 to 1992 (note the large 1994 and 1997 “Indian Ocean Dipole events”, e.g. *Saji et al*., 1997). Perhaps the monthly mean wind stresses (or the shortwave radiation, see below) associated with these events are systematically misrepresented in the FSU data set. Once again, exploration of the ERS satellite stress and wind product is called for both for its effects on ocean dynamics and on evaporation.

One more run of the ACOM2 run was performed, with different rainfall and shortwave radiation products than those used in Figures 21 and 22.In the earlier runs, shortwave radiation and precipitation were both taken from the NCEP data sets. In the new run, the precipitation is from the MSU data set, and the shortwave radiation (between 15° N and 15° S, in the Pacific and Indian Oceans west of the dateline) is from an algorithm due to *Shinoda and Hendon* (1998), using Outgoing Longwave Radiation data. Elsewhere, shortwave radiation is blended into the NCEP data set. These changes result in better simulation of observed SSTA variations during composite Madden-Julian Oscillation events (*Schiller and Godfrey*, 2002). The run covered the period 1982-1994.

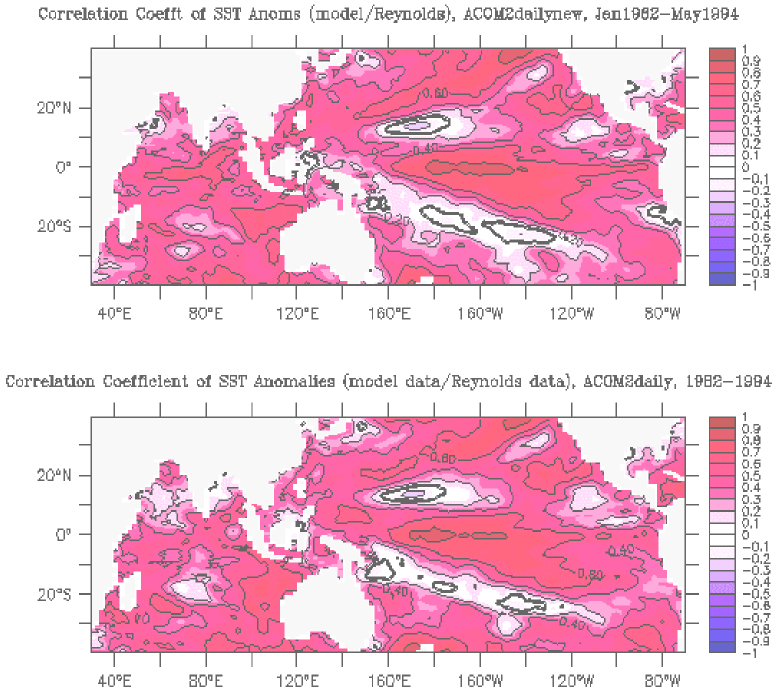

**Figure 23: The lower panel is as for Figures 21b or 22b, but for the period 1982-1994. The upper panel shows the same quantity, from a run with improved algorithms for shortwave radiation and precipitation, but winds as in ACOM2daily (see text).**

Figure 23a is the equivalent of a panel of Figure 21b or 22b, for the period 1982-1994, from the “Shinoda-Hendon” run. Correlations are now up to 0.7 in parts of the central Indian Ocean. This suggests that inclusion of the new shortwave radiation and/or the new precipitation substantially improve SSTA simulation in the Indian Ocean. The correlations become negative in the Pacific, east-southeast of New Guinea and near 170° E, 12° N — features not seen in either Figure 19b or Figure 20b. There is sufficient difference between Figures 21b and 22b to raise the possibility that these features are primarily due to time-variation of the correlation coefficients, rather than to the changed shortwave and precipitation data sets. To test this possibility, the equivalent of Figures 21b and 22b was recalculated (Figure 23b) for the same period 1982-1994 used in Figure 23a. The result is sufficiently similar to Figure 23a to conclude that most of the different features of Figure 23b compared to Figures 21b, 22b are due to the period chosen, rather than to the precipitation and shortwave data sets used. However, there is a marked increase in correlation over the equatorial Indian Ocean.

### 4.2.2 Correlations and regressions of observed and modelled SST anomalies with NINO4 SSTs

The existence in Figure 21a, 22a of quite large regions of negative or very low correlations is rather surprising. In the Pacific, these regions lie rather close to the Intertropical Convergence

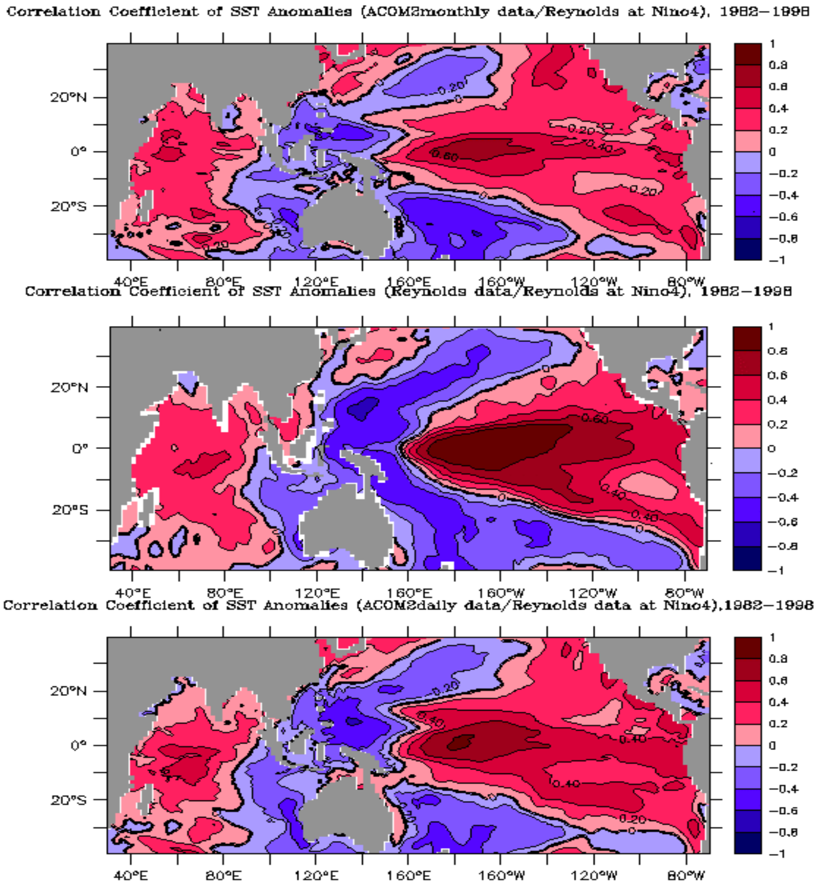

**Figure 24: Correlations of SST anomalies with observed average SSTA in the "NINO4" region. The top (bottom) panels show the correlation of ACOM2 monthly (ACOM2daily) SSTA with Reynolds NINO4 SSTA, over 17 years. The middle panel shows Reynolds SSTA correlated with Reynolds NINO3 SSTA.**

Zone and the South Pacific Convergence Zone. Some light on the origin of these regions is given by Figure 24 and 25. Figure 24b (25b) shows the correlation (regression) of Reynolds monthly mean SSTA on NINO4 SSTA at each point. They can be regarded as estimates of the correlation (regression) of observed SSTA with ENSO. Figures 24a,c (25a,c) show the correlation (regression) of the observed NINO4 SSTA index with modelled SSTA at each point in the basin, for the ACOM2 run with monthly mean stresses (Figures 24a and 25a), and with daily winds from NCEP interpolated (Figures 24c and 25c).

The correlation patterns of Figs 24a,c are broadly similar to those of Figure 24b, with a broad "boomerang-shaped" region of negative correlation whose "point" lies over the far west Pacific, sandwiched between two regions of positive correlation. However, the patterns are somewhat less smooth in the model results than in the observations; and the size of the region of negative correlation with ENSO is underestimated in the model results. Note particularly the spurious "nose" of positive correlation near 10° N, 160° E in both Figures 24a, 24c, and a similar, though weaker, feature near 10° S. The regions of negative point-by-point correlations in Figures 21a, 22a lie fairly close to regions where the correlation with ENSO has the wrong

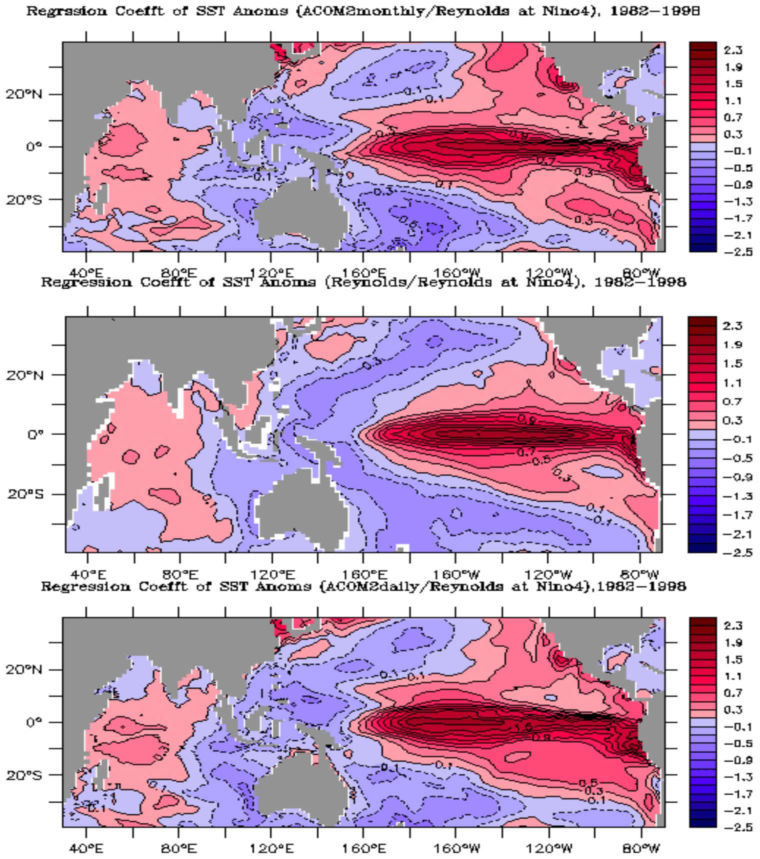

Regrssion Coefft of SST Anoms (ACOM2monthly/Reynolds at Nino4), 1982–1998

Regression Coefft of SST Anoms (Reynolds/Reynolds at Nino4), 1982–1998

Regression Coefft of SST Anoms (ACOM2daily/Reynolds at Nino4),1982–1998

**Figure 25: As for Figure 24, but showing regressions of SSTA on NINO4 SSTA**

sign in Figure 24a, relative to Figure 24b. Such problems could arise if, for example, the ENSO-related wind stress anomalies used to drive the model had systematic shifts relative to “reality”; we have discussed this possibility already in section 4.1, in connection with model reproduction of sea level anomalies. Interestingly, the spurious “nose” of negative sea level regression seen in Figures 19,c relative to Figure 19b has no clear analogue in Figures 24(25)a,c relative to Figures 24(25)b.

The regression patterns of Figure 25 contain more detail than Figure 24 for assessing model performance. It can be seen that in both model runs — i.e. with and without inclusion of submonthly wind variation — the observed pattern is quite well-simulated. The warm region in the equatorial Pacific extends too far west in Figure 25a compared to Figure 25b, and the “nose” referred to earlier is present in both Figures 25a, 25c.

We have made no formal attempt to test whether the differences between observed and model patterns in Figure 25 are statistically significant, but with the possible exception of the “nose”, it seems quite likely that they are not significant.

### 4.2.3 Seasonal variations in correlations of SSTA with NINO4

*McBride et al.* (2002; referred to below as McHN) show that the seasonal variations of the correlations of SSTA with the NINO4 index — briefly, the seasonal variations of the "boomerang" of Figures 24b and 25b — are substantial, and that these effects are potentially important for predicting Australian climate variability. It is therefore of interest to explore these seasonal variations in the output of the ACOM2 model, when driven with our two "observed" wind stress products. We show the regression patterns only, for January, April, July and October (Figures 26-29). Specifically, Figure 26 shows the correlation of all January values of NINO4 SSTA with simultaneous (January) SSTAs at each point; similarly for Figs 28-29.

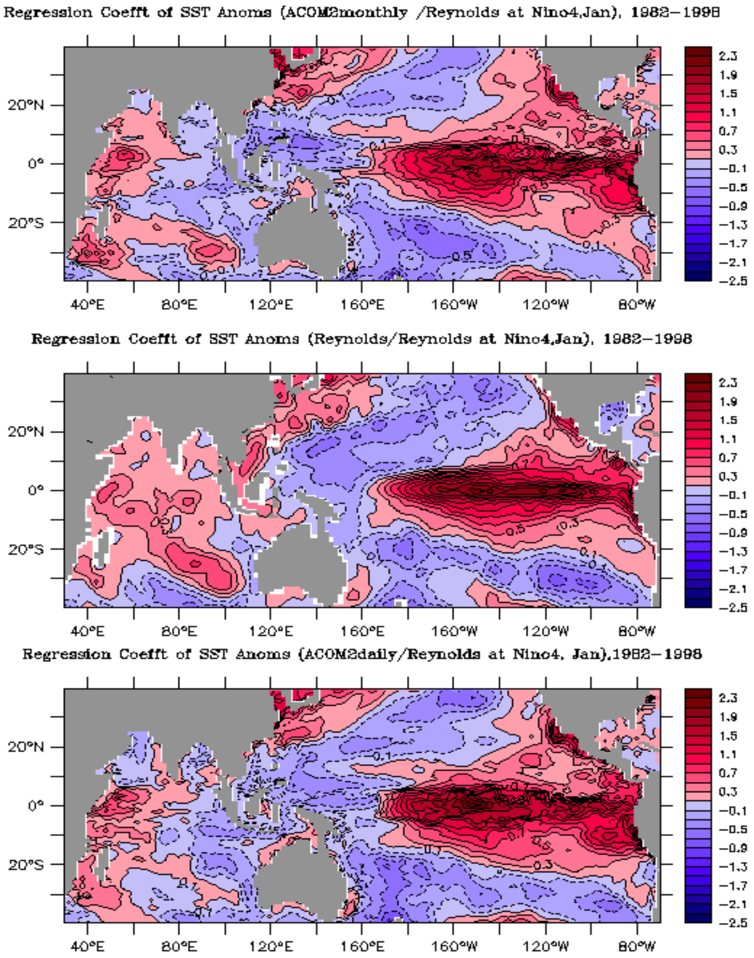
Regression Coefft of SST Anoms (ACOM2monthly /Reynolds at Nino4,Jan), 1982–1998

Regression Coefft of SST Anoms (Reynolds/Reynolds at Nino4,Jan), 1982–1998

Regression Coefft of SST Anoms (ACOM2daily/Reynolds at Nino4, Jan),1982–1998

**Figures 26: As for Figure 25, but with data from a single month only: all Januarys.**

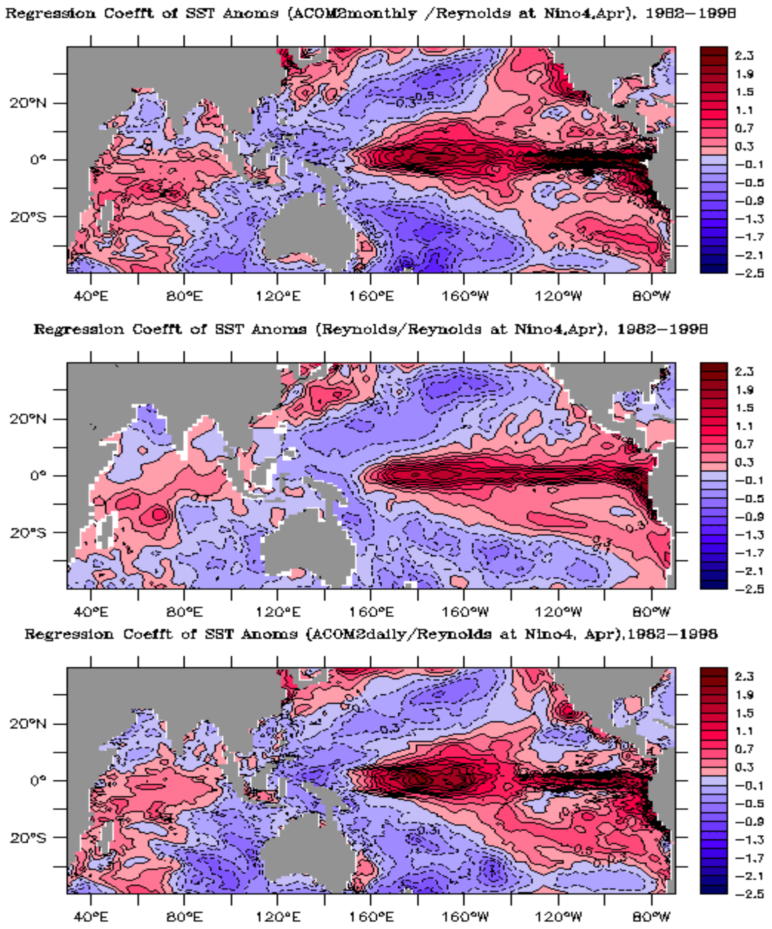

**Figures 27: As for Figure 25, but with data from a single month only: all Aprils.**

In each of Figures 26-29, the central panel is the regression of observed SSTA with NINO4. Figures 26b (28b), which correspond to austral summer (winter) respectively, should be compared with Figures 21a (22a) of McHN. While our figures are regressions and McHN’s are Empirical Orthogonal Functions, the agreement is close over the domain shown by McHN.

McHN note that in austral summer (winter), SST anomalies associated with El Niño events are positive (negative) in the Indonesian region. These effects are clearly seen in Figures 26b, 28b. They suggest that this may be linked to the fact that Indonesian winter rain is strongly related to ENSO, but summer rain is not. It is therefore of interest to see how well the ACOM2 model performs in simulating these seasonal variations in the “boomerang”. The model simulates the winter SSTA regression patterns quite well over Indonesia (compare Figures 28a,c with Figure 28b). However, the model completely misses the summer region of observed positive regressions over Indonesia, the South China Sea, and most of the eastern tropical Indian Ocean (compare Figures 26a,c with Figure 26b).

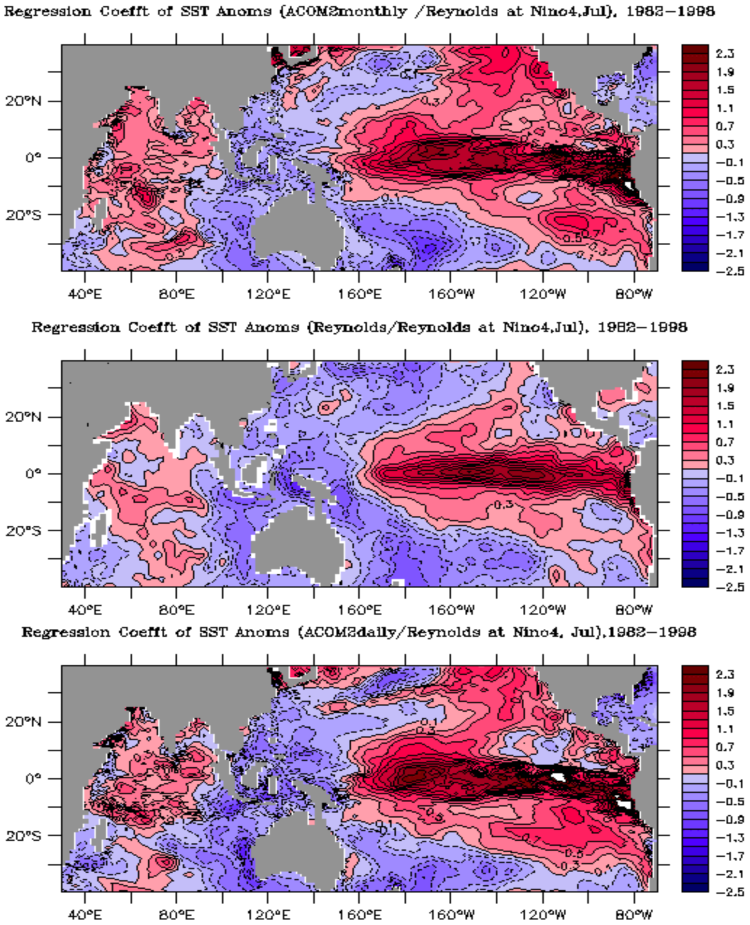
Regression Coefft of SST Anoms (ACOM2monthly /Reynolds at Nino4,Jul). 1982–1998

Regression Coefft of SST Anoms (Reynolds/Reynolds at Nino4,Jul). 1982–1998

Regression Coefft of SST Anoms (ACOM2daily/Reynolds at Nino4, Jul).1982–1998

**Figures 28: As for Figure 25, but with data from a single month only: all Julys.**

Several other differences can be noted between model and observation in Figures 26-29. However, we will not persue them further in this report, due to the suspected inadequacies of the winds used to force the model. We will return to this issue when the ACOM2 model has been rerun, with ERS monthly mean winds combined with interpolated NCEP sub-monthly winds.

Regression Coefft of SST Anoms (ACOM2monthly /Reynolds at Nino4,Oct), 1982–1998

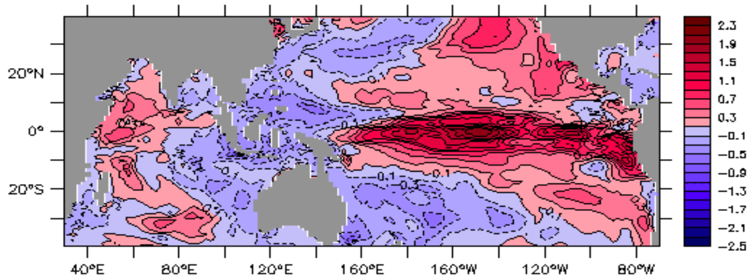

Regression Coefft of SST Anoms (Reynolds/Reynolds at Nino4,Oct), 1982–1998

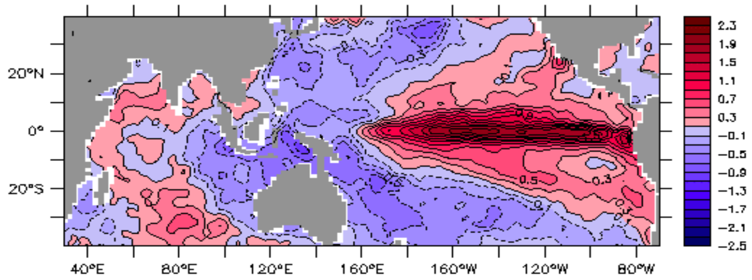

Regression Coefft of SST Anoms (ACOM2daily/Reynolds at Nino4, Oct),1982–1998

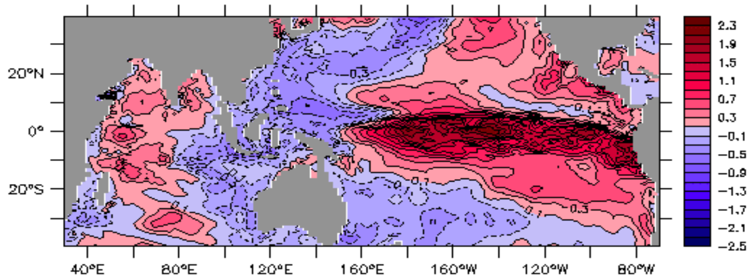

**Figures 29: As for Figure 25, but with data from a single month only: all Octobers.**

## 4.3 Sea-surface temperature during the 1997-98 El Niño and Dipole Mode events

One of the strongest El Niño events of the 20th century occured in 1997/98. Almost simultaneously, a “Dipole Mode” event developed in the Indian Ocean. The subsequent three subsections (SST, SSH and D20) deal with the simulated and observed evolution of this particular event in both oceans. The remainder of this section deals with time series analysis in the Pacific Ocean, Indian Ocean and Indonesian Throughflow, respectively. Here and below, all model data is from the “ACOM2daily” run.

Figure 30 displays the spatial and temporal development of the 1997/98 SST anomalies in the Indo-Pacific Ocean; Fig. 31 shows the corresponding differences between model and observations. In August 1997, first positive SST anomalies appeared in the central and eastern equatorial Pacific, which increased in amplitude and area until the end of 1997. At about 0° N, 140° W simulated peak anomalies exceeded 7° C. Until the end of 1997 simulated SST anomalies in the eastern equatorial Pacific were slightly larger than observed, whereas the situation was reversed in the far-east Pacific (Fig. 31a, b).

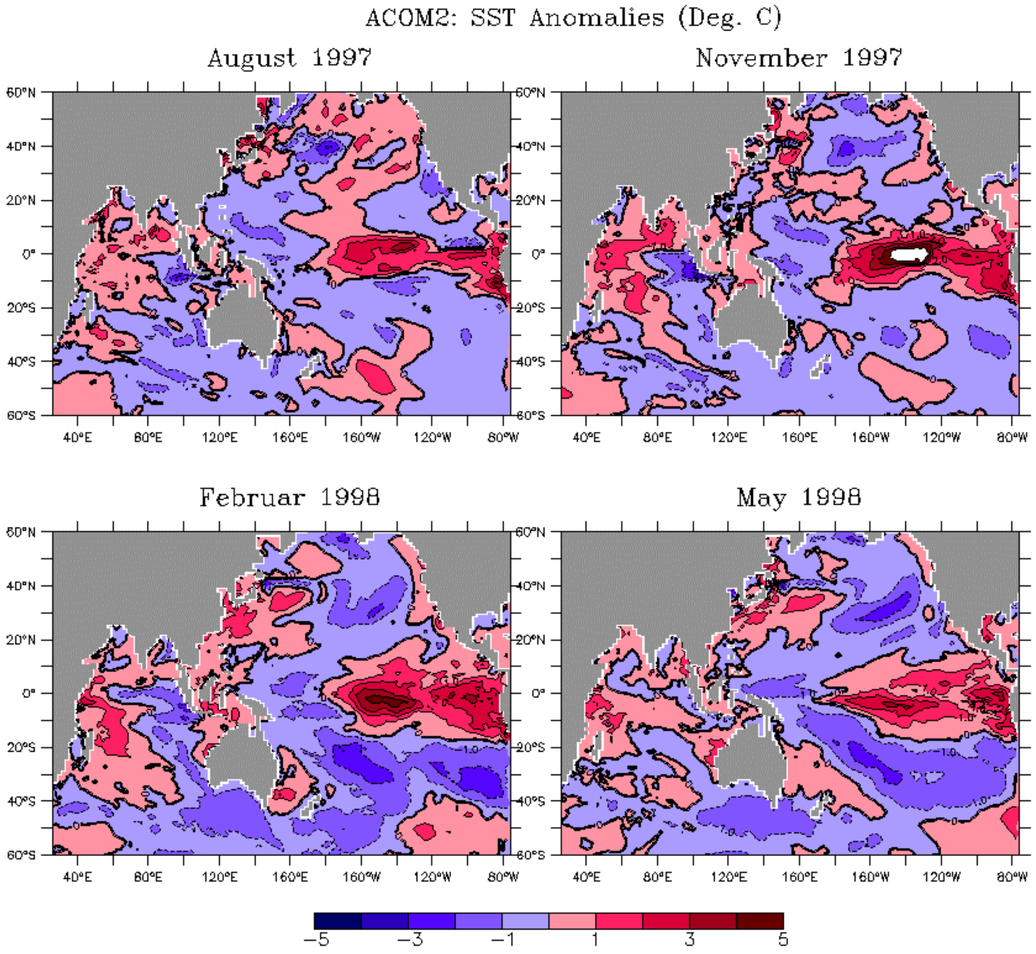

**Figure 30: 3-monthly interval of SST anomalies for period August 1997 to May 1998. Units are in °C.**

At about the same time wind-induced upwelling and associated cold anomalies developed in the eastern Indian Ocean; the same easterly wind stresses (and anomalies) plus heat fluxes into the ocean caused positive SST anomalies in the western equatorial Indian Ocean. Note that the anomalies in the Indian Ocean were much weaker (about 1-3° C) than in the Pacific Ocean. As wind anomalies eased, both equatorial oceans slowly return to their normal states, although warm anomalies in the eastern Pacific persisted well into 1998. During this period and in this area the model was up to 2° C too warm (Fig. 31c, d).

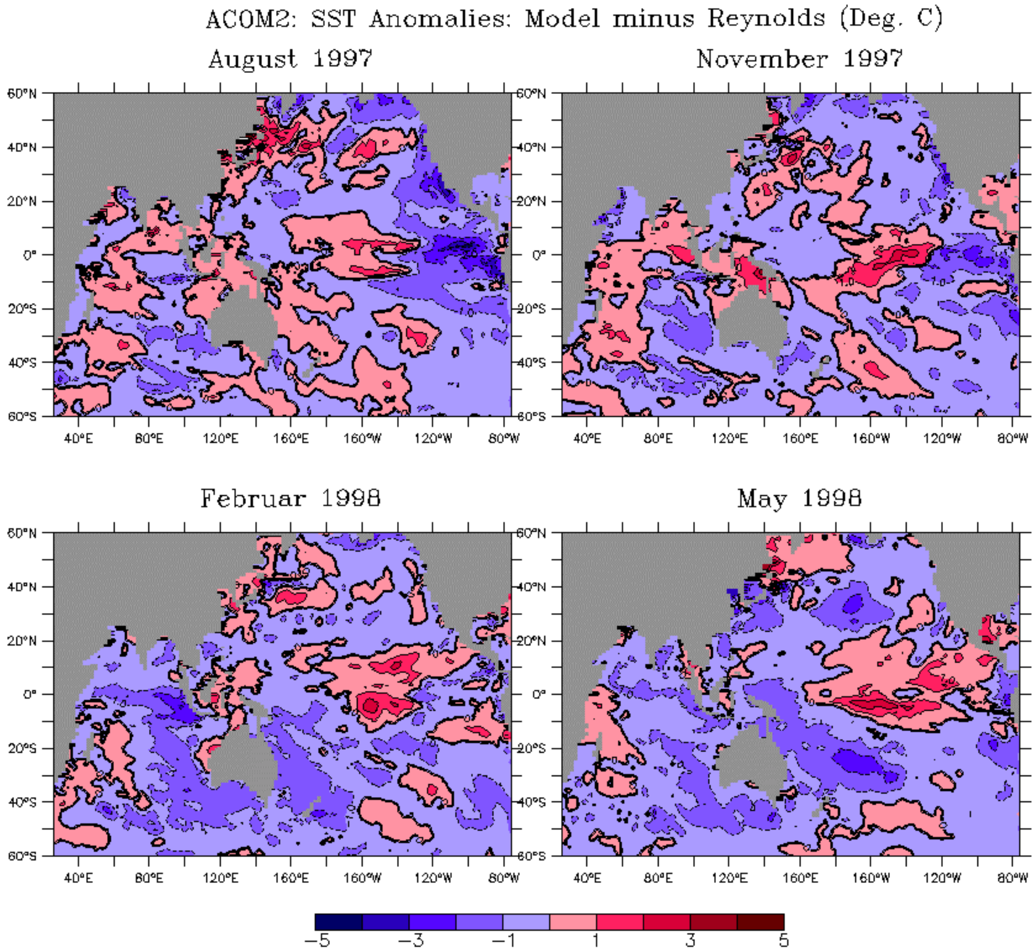

**Figure 31: Differences in SST anomalies for period August 1997 to May 1998 between model and Reynolds observations (*Reynolds and Smith*, 1994). Units are in °C.**

## 4.4 Sea-surface height during the 1997-98 El Niño and Dipole Mode events

Sea-surface height anomalies contain information about the integral circulation of the upper ocean. Fig. 32 displays the RMS difference between model and TOPEX/Poseidon satellite observations. Apart from eddy-rich regions that are not resolved by the model, such as the western boundary current regions (Kuroshio, East Australian Current, Somali Current) and a zone in the southern Indian Ocean the RMS error is typically 5-10cm, indicating a reasonable agreement between model and observations, whose RMS variations compared to *in situ* tide gauges are typically about 4cm (*Chelton et al.*, 2001). However, variability in the Pacific due to large El Niño events is about 20-30 cm and at other times is about 10-20 cm, so the RMS differences between observed and modeled SSH still represent a significant error.

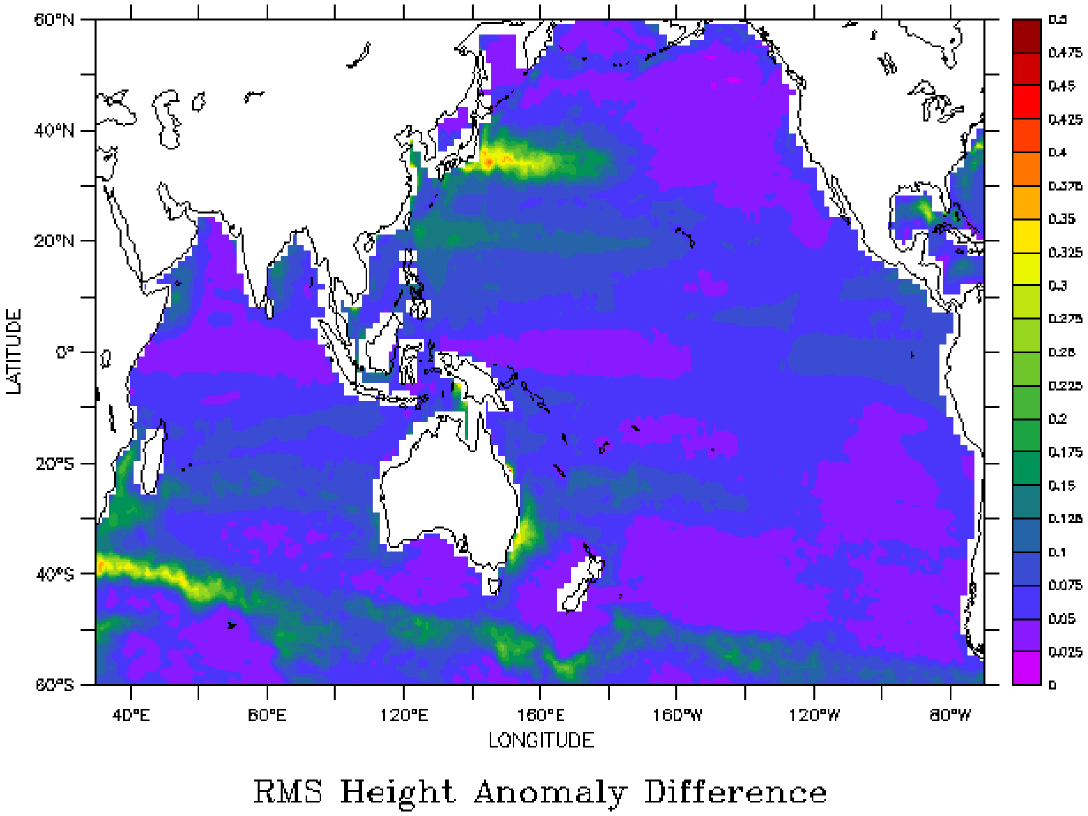

**Figure 32: RMS Differences in SSH anomalies between model and TOPEX/Poseidon satellite observations. Contour interval is 2.5 cm.**

Figure 33 displays the simulated (left column) and observed (right column) cycle of SSH anomalies for the 1997/98 period. Although the model slightly underestimates the observed SSH amplitudes by typically 5cm, there is much better agreement between simulation and observation for SSH anomalies than there is for SST anomalies. This is a well-known feature of many ocean models and reflects the uncertainties associated with atmospheric forcing fields (in particular surface heat fluxes) that predominantly impact on SST rather than SSH (which is mainly driven by surface wind stresses). Note, however, the distinct differences in May 1998 in the area of the North Equatorial Current /North Equatorial Counter Current. Only recently use of satellite wind products has improved the simulation of this feature (which is not properly resolved in the wind forcing used here). The differences between Figures 18b,c must largely reflect the differences between Figures 33 (left and right columns).

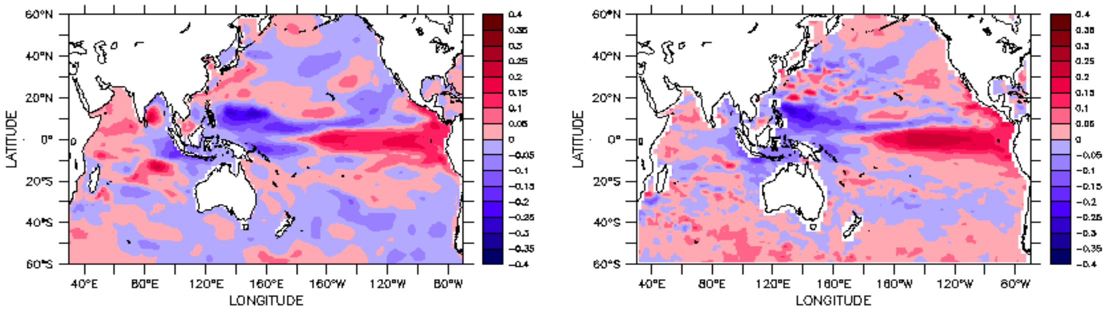

Aug 1997 Aug 1997

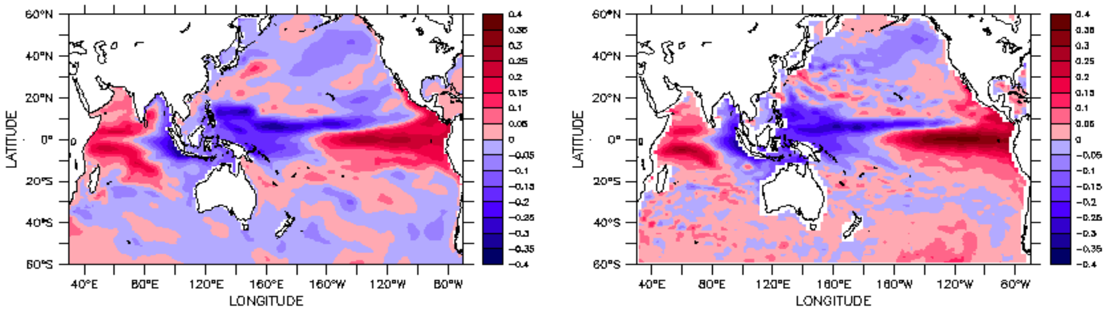

Nov 1997 Nov 1997

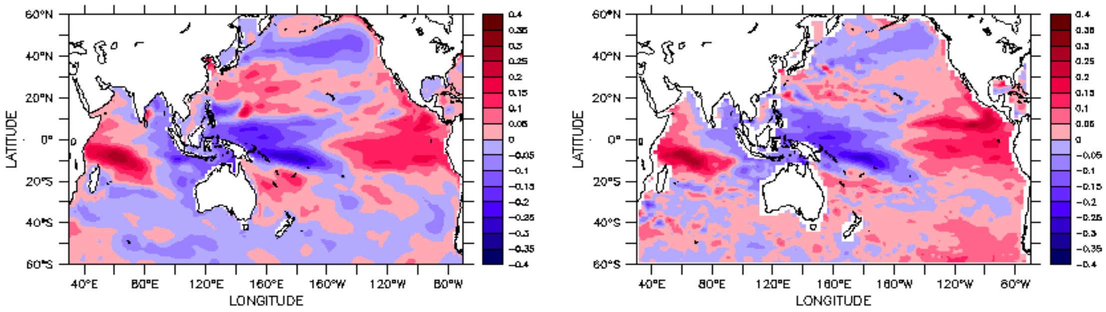

Feb 1998 Feb 1998

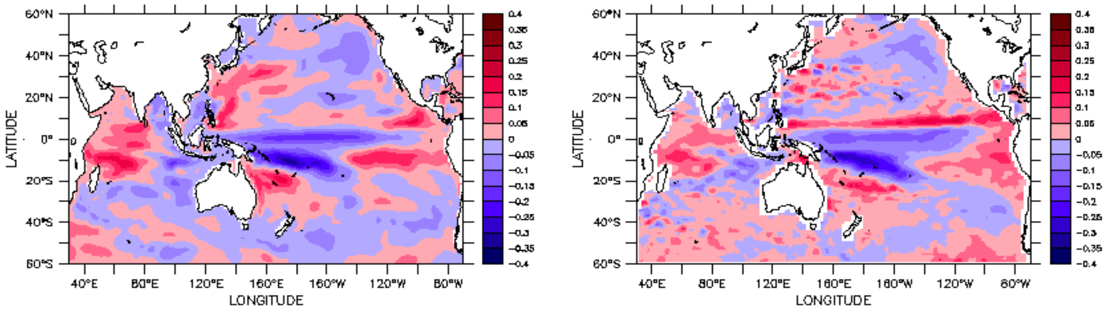

May 1998 May 1998

**Figure 33: 1997/98 SSH anomalies for model (left column) and TOPEX/Poseidon satellite observations (right column). Units are in m.**

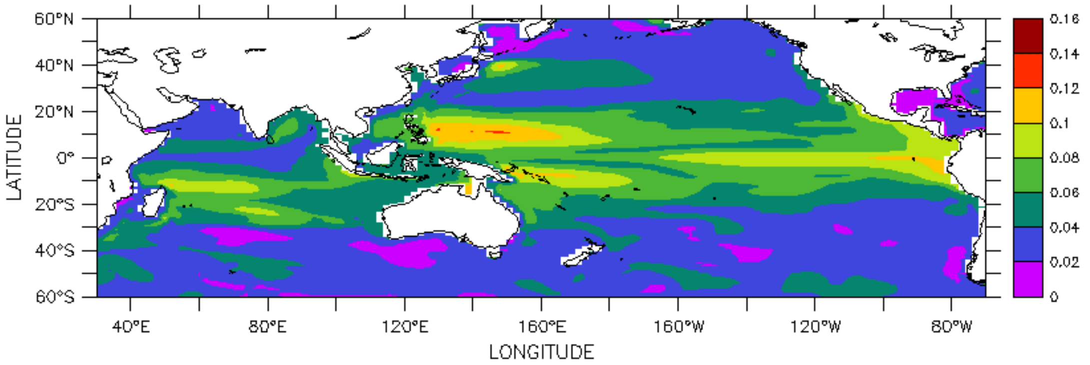

Model SSH standard deviation

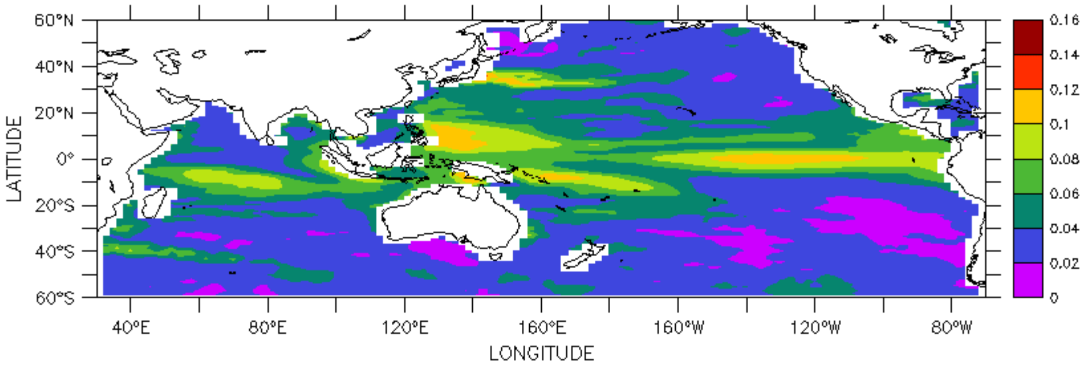

Observed SSH standard deviation

**Figure 34: Simulated and observed standard deviations of SSH anomalies (same data sets as in Fig. 33). Units are in m.**

Note that the model overestimates SSH variability in the western Pacific north of the equator (Fig. 34), but slightly underestimates variability in the central and eastern Pacific (apart from a small strip off Peru).

## 4.5 Depth of 20° isotherm during the 1997-98 El Niño and Dipole Mode events

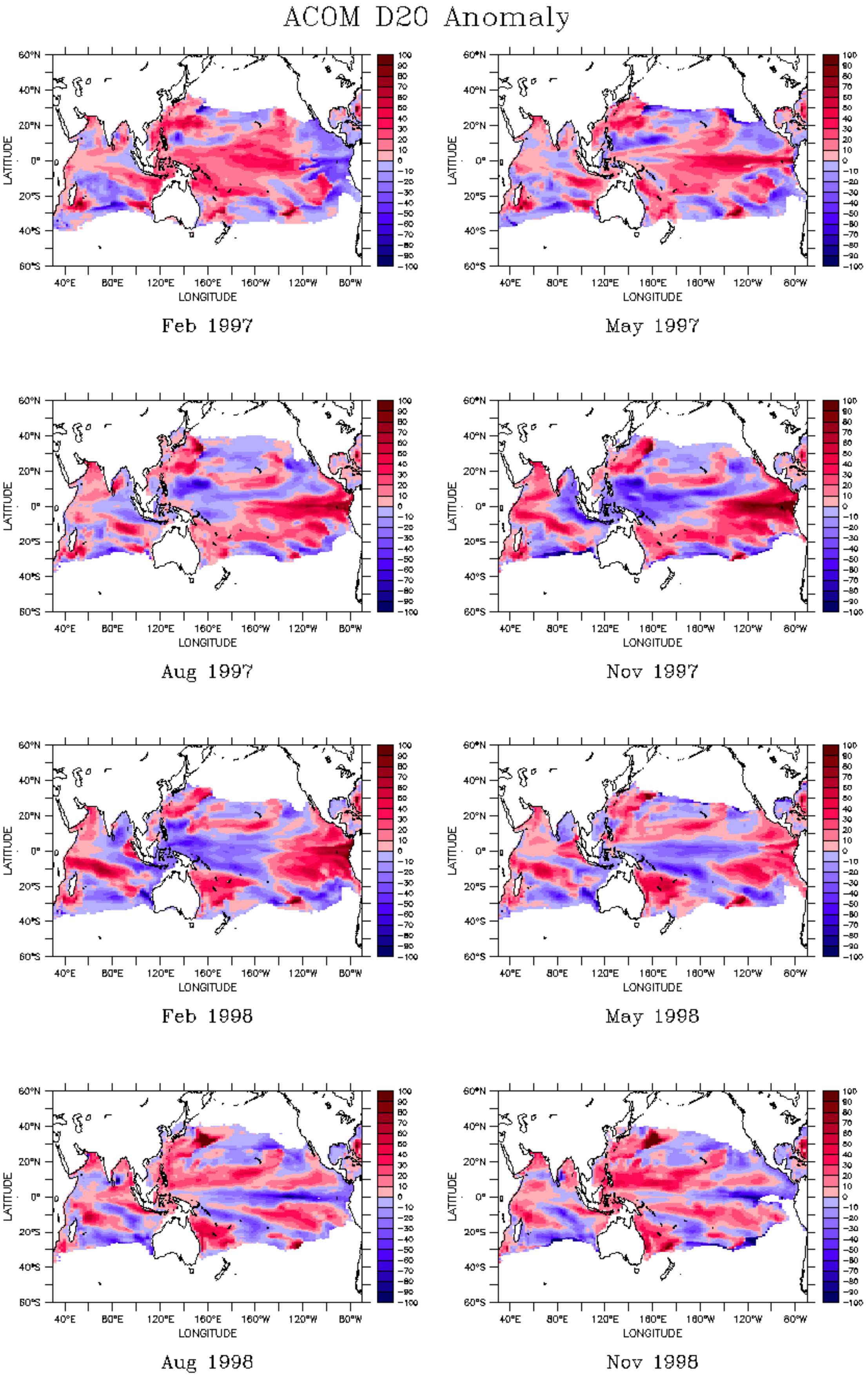

Feb 1997

May 1997

Aug 1997

Nov 1997

Feb 1998

May 1998

Aug 1998

Nov 1998

**Figure 35 (previous page): 3-monthly interval of D20 anomalies for period February 1997 to November 1998. Units are in m.**

Interannual variability in the tropical ocean is associated with changes in the depth of the thermocline. An appropriate proxy for thermocline variability is the depth of the 20° isotherm. Fig. 35 displays the temporal evolution of D20 anomalies for the period February 1997 to November 1998 from the ACOM2daily run. First signs of the developing El Niño become apparent in the far eastern Pacific in May 1997. The anomalies continue to grow until November 1997 (>120m). At the same time a weaker, but large-scale negative anomaly in thermocline depth develops in the western Pacific. In early 1998, the conditions in the equatorial Pacific slowly return to normal and are replaced by a weak La Niña in late 1998.

In the Indian Ocean a "Dipole Mode" develops simultaneously to the events in 1997 in the Pacific Ocean, but anomalies in D20 are much weaker (40-80m). Furthermore, south of the equator in the Indian Ocean the development and slow westward progression of a downwelling Rossby wave can be seen (*Webster et al.*, 1999).

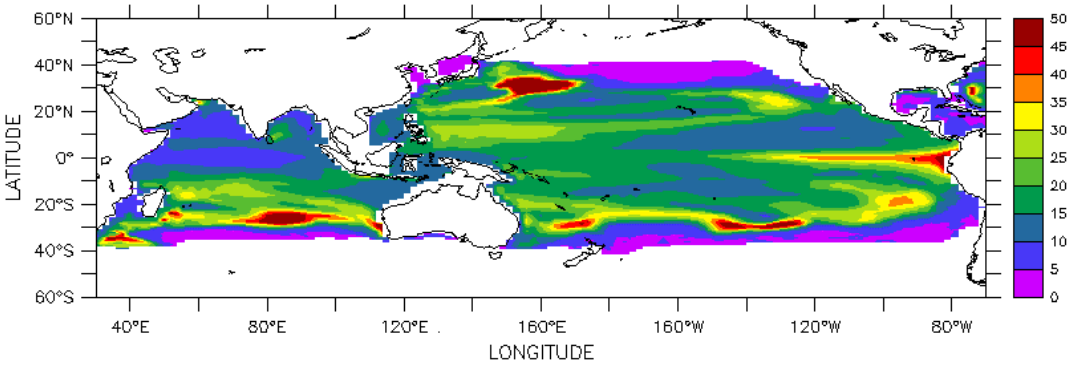

D20 standard deviation 3 day forcing

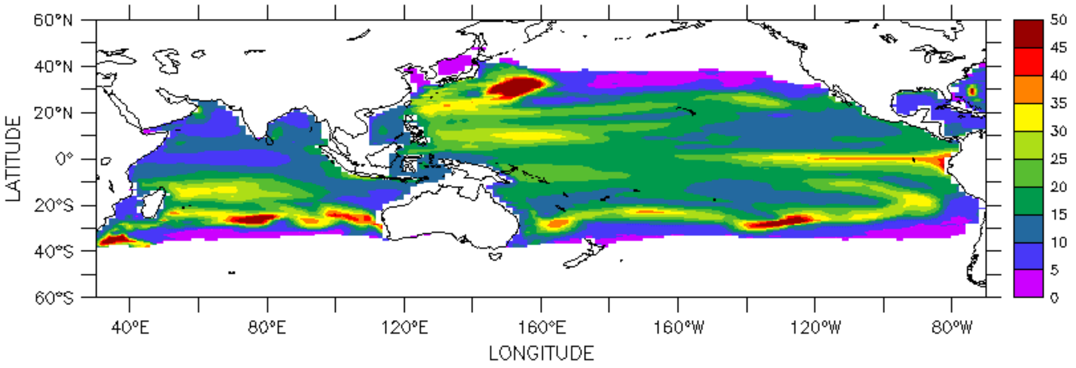

D20 standard deviation monthly forcing

**Figure 36: Standard deviation of D20 anomalies for 3-day mean forcing (top) and monthly mean forcing (bottom). Units are in m.**

Fig. 36 reveals that the long-term variability in D20 is only weakly dependant on the forcing fields. Slightly larger variability is found in the east Pacific in the 3-day mean run, whereas in the west Pacific and subtropical Indian Ocean the monthly mean run exposes a stronger variability. Differences are of the order of about 5m in D20 variability.

The simulated anomalies are validated with data from the TOGA/TAO array in the equatorial Pacific Ocean. Fig. 37 displays time series of D20 anomalies for model and observations at two sites in the eastern (140º W) and far eastern (110º W) equatorial Pacific. The two outstanding features at 140º W relate to the 1988-89 La Niña event (shallow thermocline, i.e. negative anomalies) and the 1997-98 El Niño event (deep thermocline), followed by a weak La Niña event. D20 anomalies at 110º W show similar signals, but with larger variability, in particular in the model results. The weaker agreement of model and observations is also reflected in the correlation between these quantities, which is r = 0.76 at 110º W and r = 0.86 at 140º W. Details of physical mechanisms acting in the far east Pacific are discussed in section 4.7.

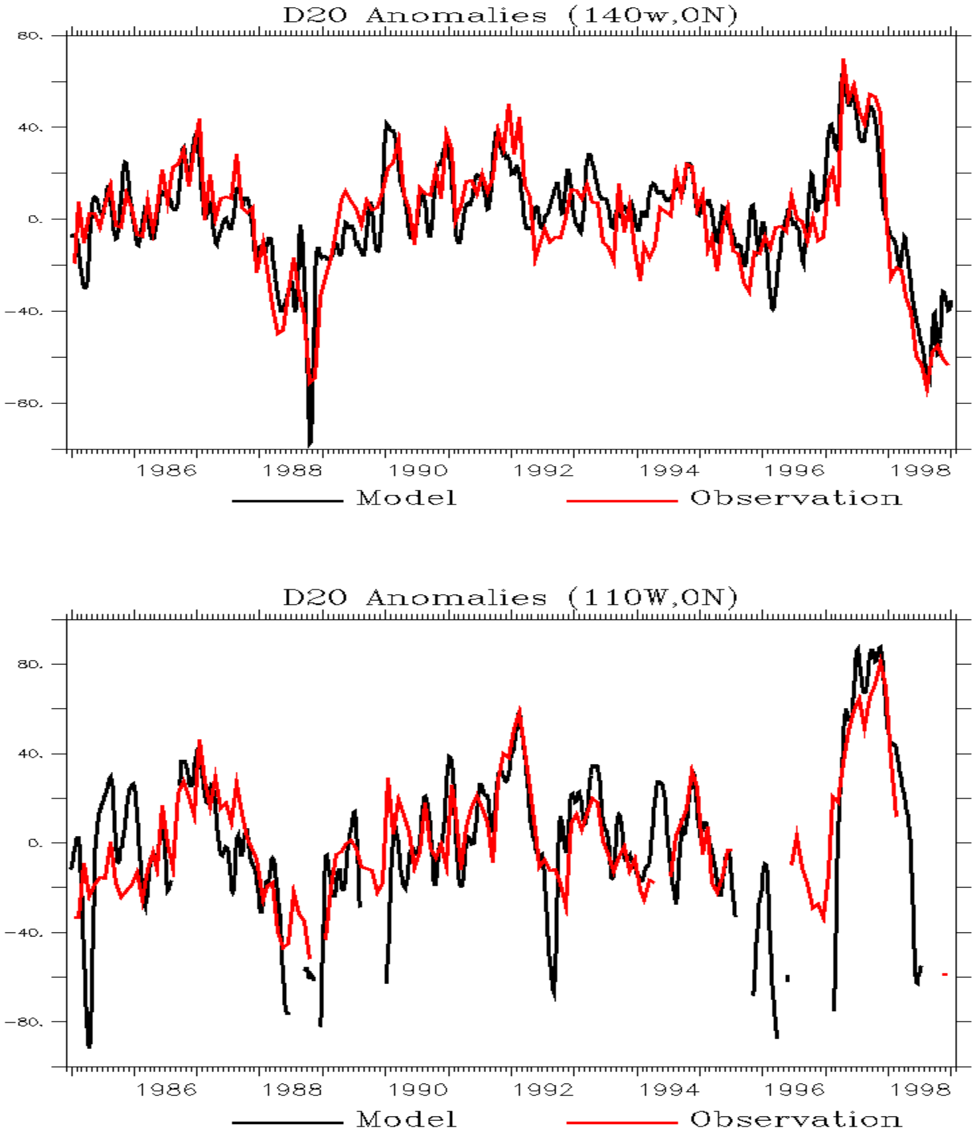

**Figure 37: Time series of observed (Tao array) and simulated D20 anomalies. Top: 0° N, 140° W, bottom: 0° N, 110° W. Units are in m. Missing model data are associated with SSTs less than 20º C.**

## 4.6 Time series in the equatorial Pacific

This section deals with time series of temperature and zonal velocities in the equatorial Pacific. Observations are based on the TOGA/TAO array. Note that no sufficiently long time series of zonal velocity was available at 156° E or any other equatorial station in the western Pacific. Amplitudes and phases of simulated temperature and zonal velocity anomalies agree reasonably well with observations, but the thermocline in the model is generally about 50m deeper than in the observations (Figs. 38, 39, 41). Further details about interannual dynamics of the ACOM2 model, including heat and momentum budgets, can be found in *Schiller et al.* (2000).

Because many features of these figures are discussed in other sections of this report, no detailed analyses is performed in this section. The figures shown here serve as a reference for other model runs.

### 4.6.1 Temperature anomalies in west Pacific (0N, 156E)

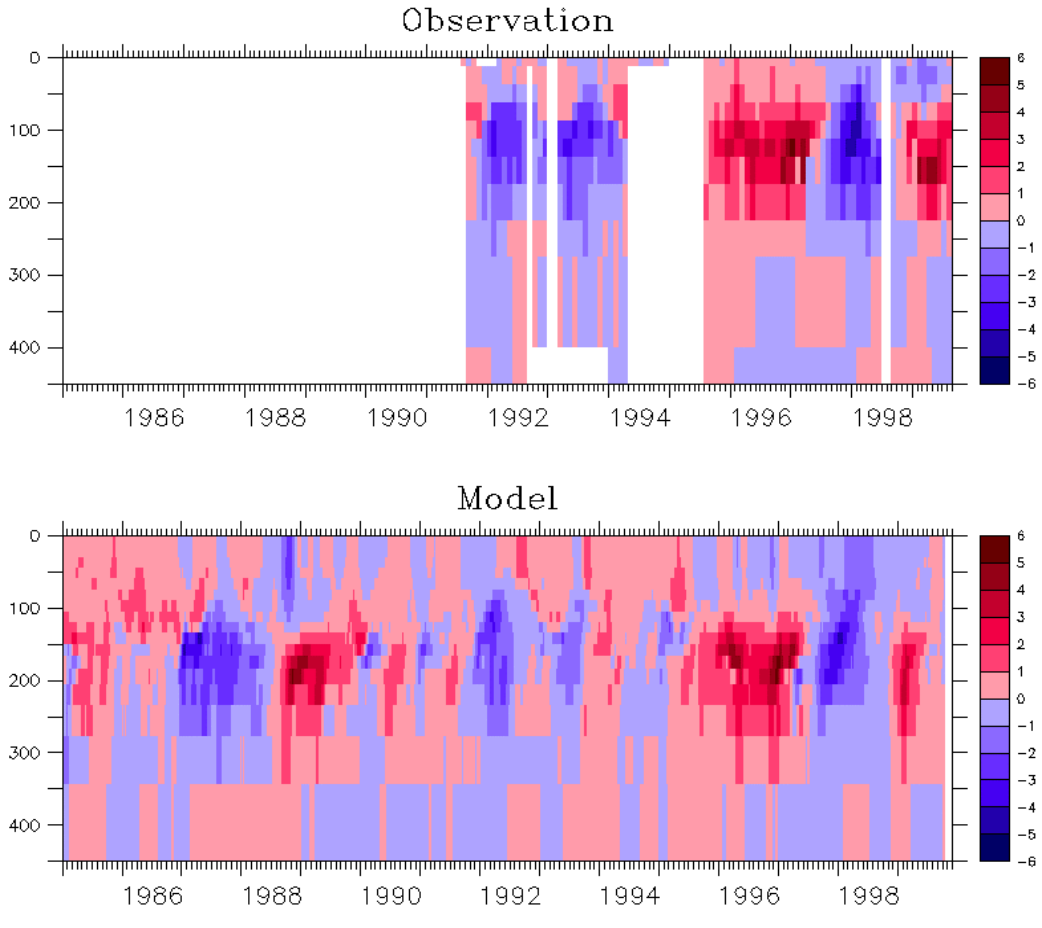

**Figure 38: Monthly mean potential temperature anomalies at 0° N, 156° E. Top: observations (TAO array; *Hayes et al.*, 1991), bottom: model. Units are in °C. Model data have been smoothed with a 33-day running mean filter.**

### 4.6.2 Temperature and zonal velocity anomalies in east Pacific

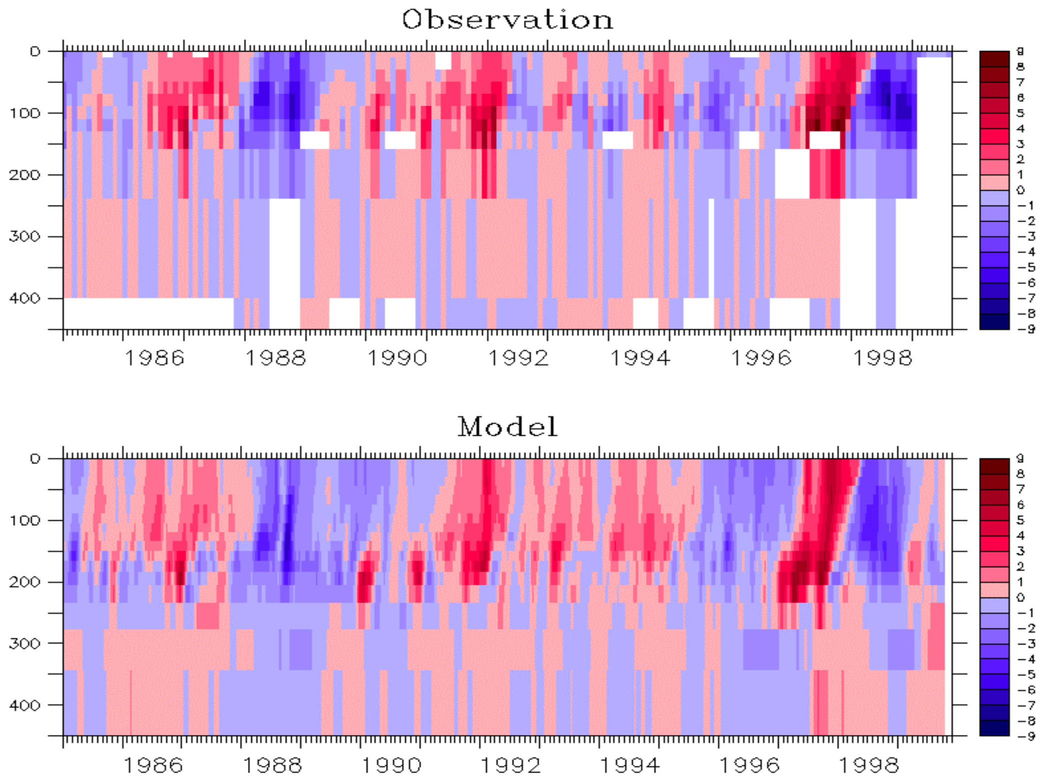

Figure 39: Monthly mean potential temperature anomalies at 0° N, 140° W. Top: observations (TAO array), bottom: model. Units are in °C.. Model data filtered as in Fig. 38.

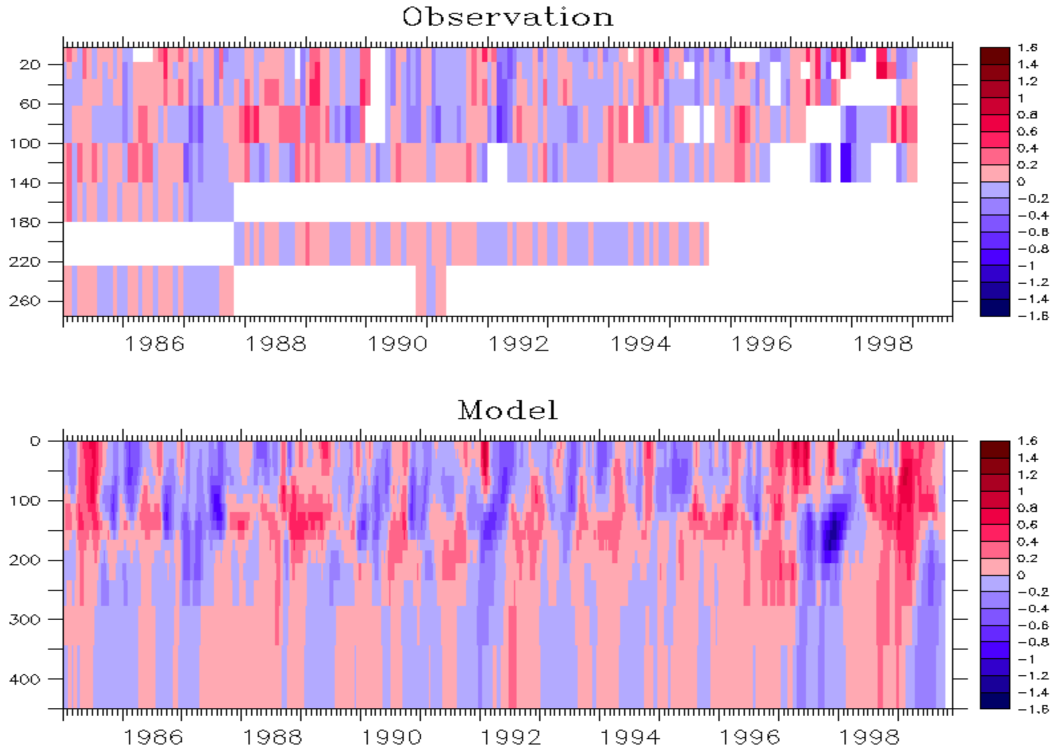

Figure 40: Monthly mean zonal velocity anomalies at 0° N, 140° W. Top: observations (TAO array), bottom: model. Units are in m/s. Model data filtered as in Fig. 38.

### 4.6.3 Temperature and zonal velocity anomalies in far eastern Pacific

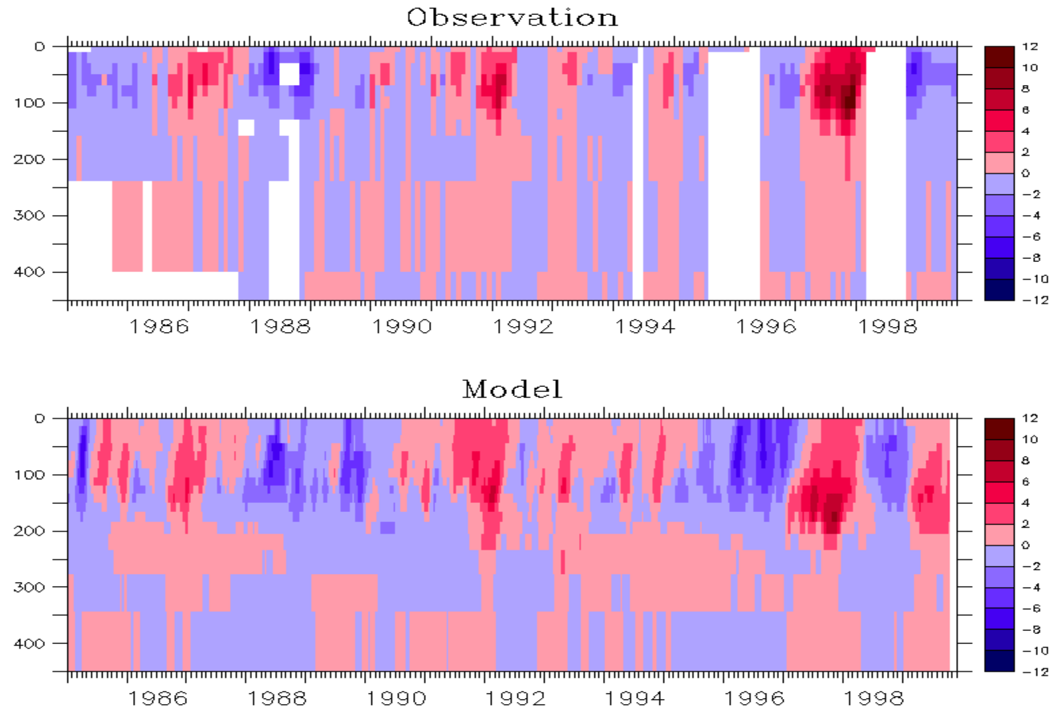

**Figure 41: Monthly mean potential temperature anomalies at 0° N, 110° W. Top: observations (TAO array), bottom: model. Units are in °C. Model data filtered as in Fig. 38.**

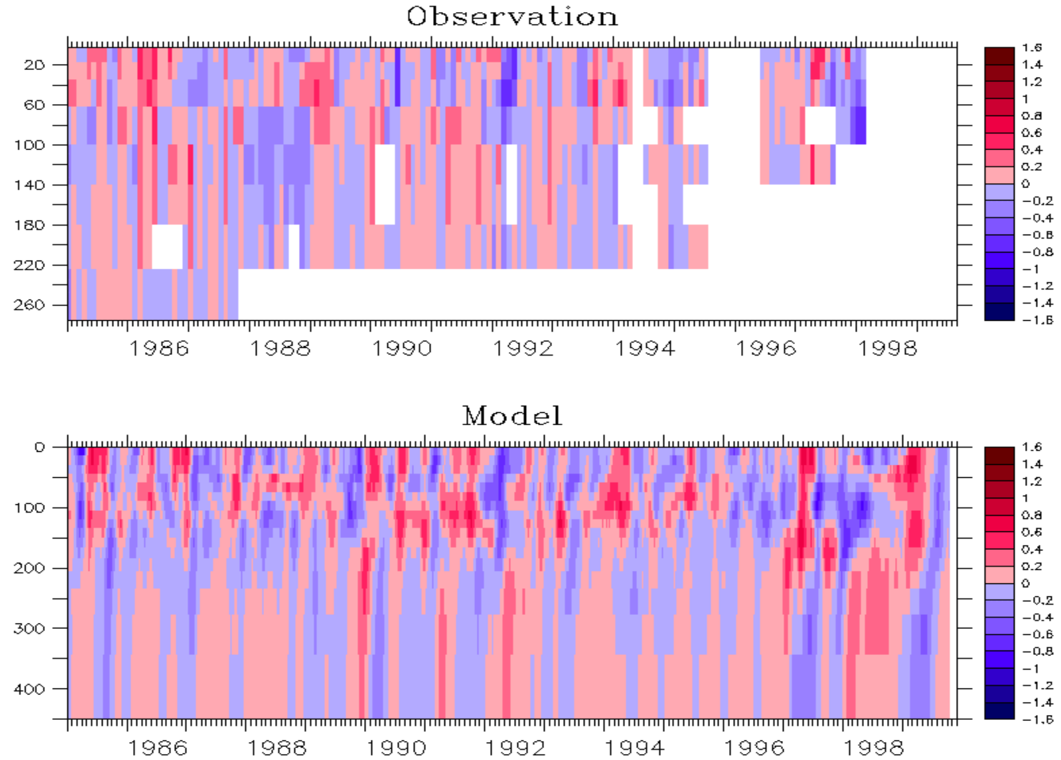

**Figure 42: Monthly mean zonal velocity anomalies at 0° N, 110° W. Top: observations (TAO array), bottom: model. Units are in m/s. Model data filtered as in Fig. 38.**

## 4.7 Spasmodic formation of deep internal mixed-layers in the eastern equatorial Pacific Ocean

As is well-known, water-mass transformations in the intense shears of the Equatorial Undercurrent play a major role in controlling the temperatures of upwelled water in the east Pacific. However, so far as we are aware, researchers have generally assumed that this process is confined to the waters that move rapidly upward towards the surface in the central Pacific. There are reports that deep internal mixed-layers are found in models in the far east Pacific, but these have been assumed to be a spurious model artefact.

In this section, we discuss these model features in some detail. However, before proceeding it may be noted that since writing the paragraphs below this one, we have tested the model against the only adequate data source that we know of: namely temperature data from the TAO mooring at 95°W. These observations (see http://www.marine.csiro.au/~kessler/model/model-n-tao-waterfallplots-3-jul-94.gif, plus later plots with the date replaced by 2-aug-94; 1-sep-94; 1-Oct-94; 31-oct-94) do not show the sharp development of a very intense thermocline, as seen in Figs 43 and 44 below. Thus while enhanced internal mixing of the type found in the model may occur in the reality, it is almost certainly overestimated in this model. We plan to explore whether these unrealistic features can be controlled by changing the parameterisation of mixing as a function of Richardson number, and will report the results to BMRC.

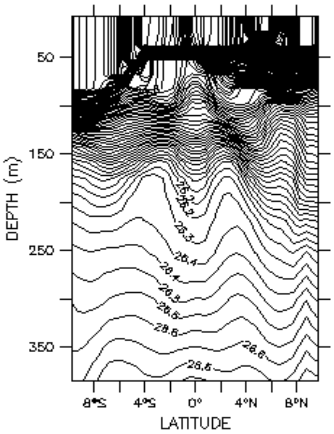

Pot. Density, 84W, June 1983

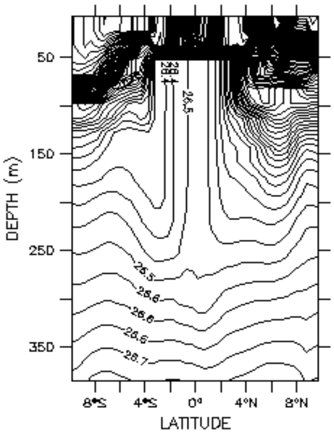

Pot. Density, 84W, Nov 83

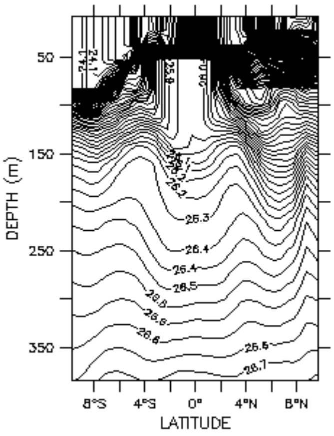

Pot. Density, 84W, Sep 83

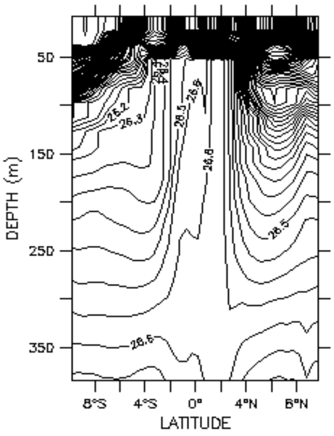

Pot. Density, 84W, Jan 84

**Figure 43 (previous page): Cross-equatorial sections of potential density at 86º W for July 1983 (top left), November 1983 (top right), September 1983 (bottom left) and January 1984 (bottom right). Contour interval is 0.1 kg/m$^3$.**

In the version of the ACOM2 model reported here, we find that internal mixed-layers, up to 200m deep or more, develop spasmodically in the eastern equatorial Pacific. Figure 43 shows potential density sections across the equator, at 86° W. The data are from the "ACOM2monthly" run, and the four panels show density at 2-monthly intervals starting from July 1983.

In July 1983, the strong equatorial "bulge" of the isopycnals implies negative $\partial u/\partial z$ from 120m to 70m and positive $\partial u/\partial z$ from about 350m to 120m, through the equatorial thermal wind relation, $\beta\partial u/\partial z = (g/\rho)\partial^2\rho/\partial y^2$. Thus we anticipate a maximum eastward current at 120m at this time. However, no mixed-layers are apparent at 86° W in July 1983, below the surface mixed-layer.

By September 1983 an internal mixed-layer 80m deep has developed within about 1° on either side of the equator. This mixed-layer is denser than water on either side of it, suggesting that (if the equatorial thermal wind relation still applies) we would expect strong negative $\partial u/\partial z$; if so, we might expect low Richardson numbers, and intense mixing in this region.

By November 1983 the internal mixed-layer has deepened to over 200m, and its density has increased from 26.0 in September to 26.5 in November. By January 1984 weak density stratification has returned at the equator, though a 300m-deep body of water with a density of 26.6 can be seen near 2°N; by March 1984 (not shown) stratification is reestablished right across this section.

Further insight into the development of these internal mixed-layers is seen in Figure 44, which shows potential density along the equator at the same times as in Figure 43. The red vectors show zonal and vertical velocity, while water inside the green contours has a Richardson number of 0.25 or less, implying intense vertical mixing.

In July 1983, a region of internal mixed-layers and subcritical Richardson number is seen west of 94° W, between about 100m and the base of the (very intense) thermocline. Strong zonal currents are seen; in particular, there is a maximum current at about 120m at 86° W, as anticipated from the corresponding panel of Figure 43. Two months later, internal mixed layers have developed near 86° W, at the eastern end of a region of subcritical Richardson numbers and essentially uniform density of 26.0-26.1 that is 1000 km long, about 100m deep and (from Figure 1) about 200 km wide. At 94° W, the western edge of the low-Richardson number region coincides with a break in the mixed-layer and 15m deep "thermocline". The surface mixed-layer shallows from 45m to 30m (i.e. by one vertical grid interval, in our model), everywhere west of 96° W. Water is presumably being entrained into this mixed-layer both from above and below.

**Figure 44 (next page): Cross-equatorial sections of potential density at 86º W for July 1983 (top left), November 1983 (top right), September 1983 (bottom left) and January 1984 (bottom right). Contour interval is 0.1 kg/m³ (black lines). The red vectors show zonal and vertical velocity, while water inside the green contours has a Richardson number of 0.25 or less, implying intense vertical mixing.**

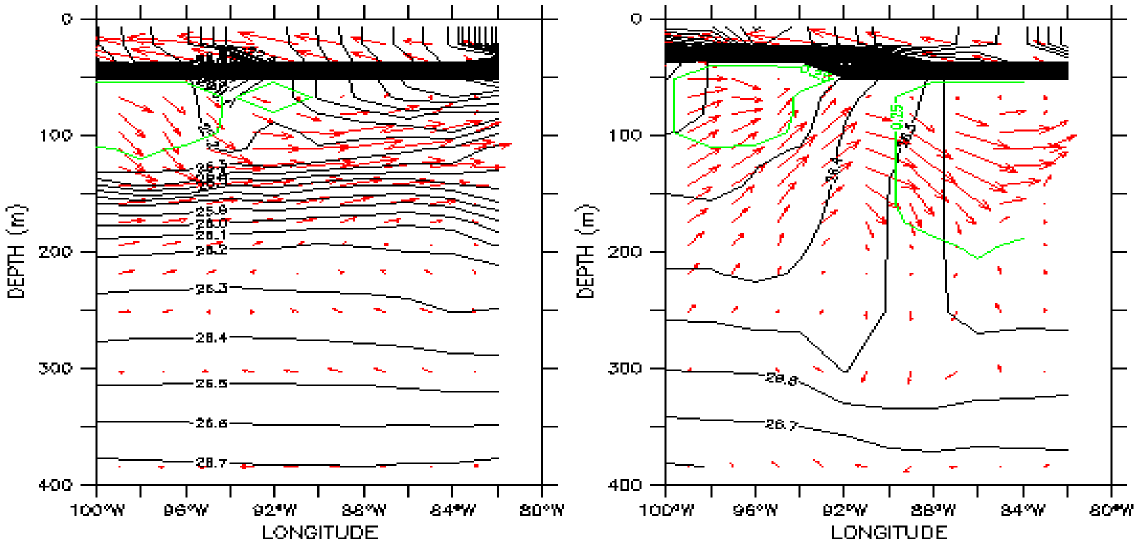

T,u,w along equator, Jul 83 T,u,w along equator, Nov 83

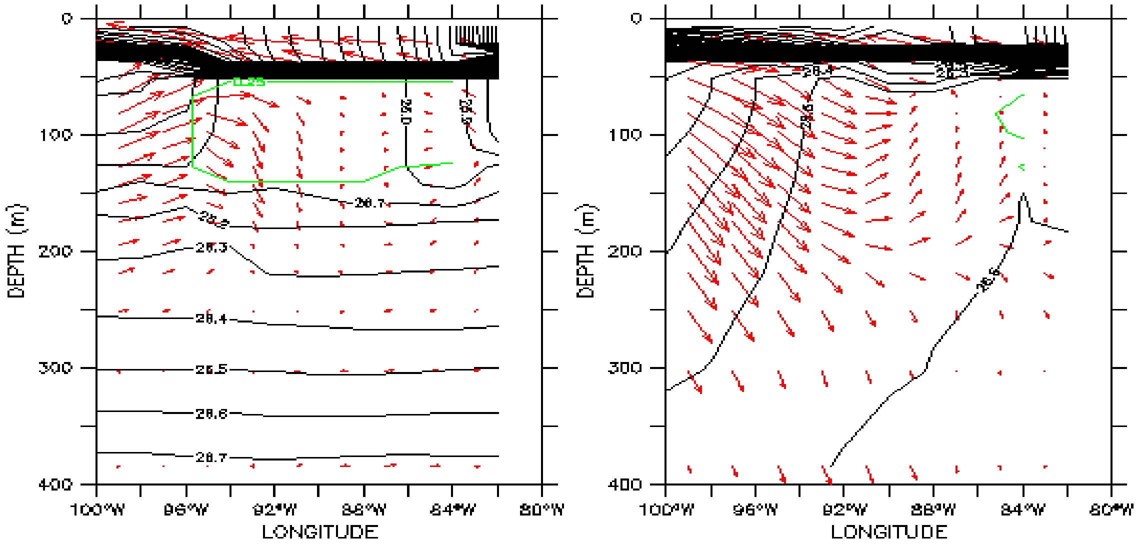

T,u,w along equator, Sep 83 T,u,w along equator, Jan 84

Two months later (November 1983), the break in the mixed-layer has moved about 300 km eastward, to 93° W. The internal mixed-layer is now over 200m deep; the peak of mixing has passed, indicated by the fact that water of constant density extends well below the region of active mixing (subcritical Richardson number). The density of the mixed water has now increased to 26.5. Two months later still (January 1984), the surface mixed-layer depth has decreased to 30m almost throughout the region, but stratification is returning below. The large mass of water with density of 26.5 seen above 200m has a temperature of 13°-14.5° C (not shown), quite similar to that of the well-known “thermostad” of the east Pacific (e.g. *Lukas*, 1986). The density variations associated with this range of temperature variations is largely compensated by salinity.

One consequence of an event such as that of Figures 43 and 44 is that density in the far east Pacific increases markedly; so steric heights must decrease. It is well-known that at least in steady state, the “depth-integrated steric height” (P(x,y)) obeys a relation close to $\partial P/\partial x = \tau^{(x)}/\rho g$, with  the zonal wind stress. Thus at the start of La Nina events when zonal winds are strong, P must have a large difference between east and west Pacific, implying low P values in the east Pacific. But P can be expressed as:

$$P = -\int_{-z}^{0}\int_{-z}^{z} (\rho(z')/\rho)\, dz'dz = -\int_{-z}^{0} z\rho(z)/\rho)\, dz$$

This suggests that the mixing events found in Figures 43 and 44 may be associated with the large (easterly) zonal winds found at the start of La Niña events.

To test this hypothesis, the green line in Figure 45 shows the density difference Δρ between 70m and 120m at (0°, 86° W). Δρ is zero in late 1983, as expected from Figures 43 and 44,

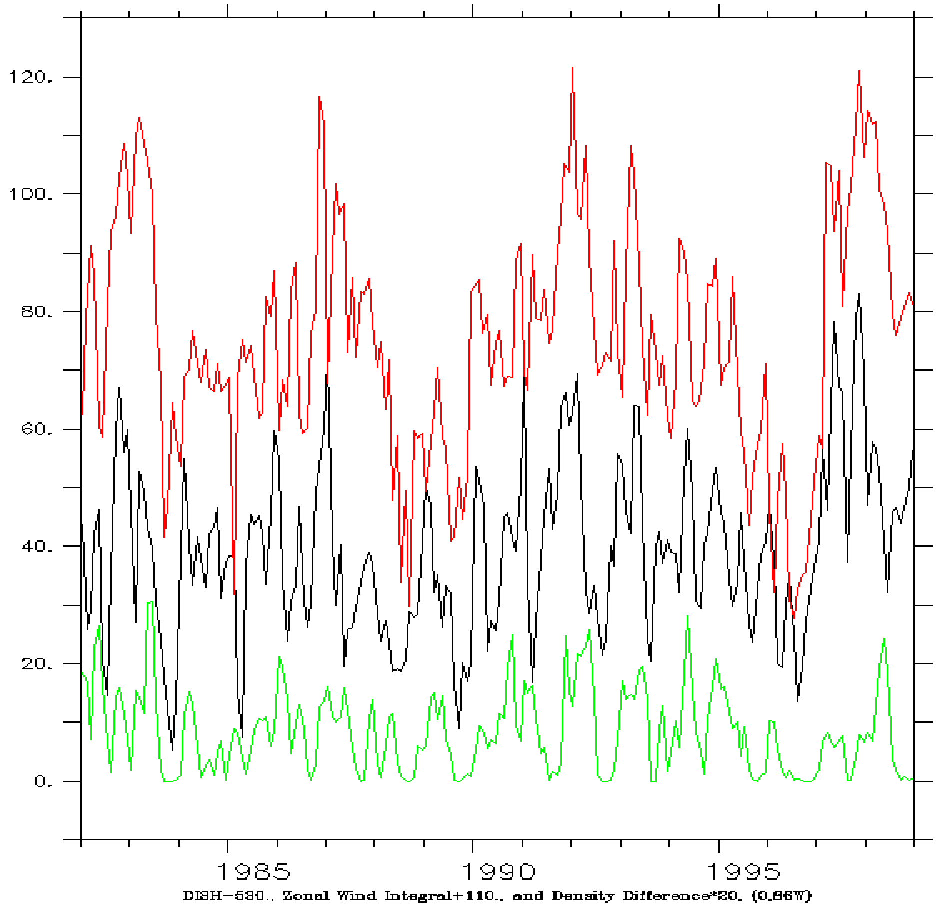

**Figure 45: Green line: density difference Δρ between 70m and 120m at (0°, 86° W); units are in kg/m$^3$*20.  Black line: depth-integrated steric height P(86°W, 0°)-530; units are m$^2$. Red line: $\int \tau(x)\, dx/\rho g$, integrated across the Pacific; units are m$^2$.**

down to below 120m. Inspection of Figure 45 shows that such events are quite common. For the green line, the left-hand scale is in kg/m$^3$*20 (the factor 20 has been applied for convenience of comparison with P).

The black line shows the quantity [P(86°W, 0°)-530] m$^2$ (the additive constant of –530 m$^2$ is arbitrary, and is again chosen for convenience). Evidently, there is a strong tendency for occurrences of low P to coincide with occurrence of near-zero density differences $\Delta\rho$.Thus times when internal mixed layers are at least 50m deep tend to coincide with times of low P(86°W, 0°), as hypothesised; though counterexamples can be found on comparison of the two time series.

Finally, the red line shows $\int \tau(x)\ dx / \rho g$ , integrated across the Pacific. There is a very close correspondence between P and this wind integral, with the latter leading the former by 1-2 months (as might be expected from Kelvin wave dynamics).

It thus appears that — in the ACOM2 model at least — fluctuating zonal winds along the equator cause formation of deep internal mixed-layers in the far eastern equatorial Pacific. These events seem to represent a significant source of water mass formation. It is tempting to speculate that the model may in fact be simulating a real physical process, namely the formation of “13° C water” (*Lukas*, 1986). In the model, the time-average formation rate of this water is of order 10 Sverdrups (1 Sv = 10$^6$ m$^3$s$^{-1}$). The eastern equatorial Pacific model errors in climatological mean temperature and salinity (Figs. 8, 10) may reflect errors in representing water-mass change processes in this region.

## 4.8 Indonesian Throughflow

In this section model results along the XBT section IX1 (see Fig. 13 for location) are validated with observations of SST, D20 and geostrophic transport anomalies. Anomalous circulation features of the Indonesian Throughflow can be advected downstream with the Leeuwin Current and impact on climate and Rock Lobster fisheries off south-western Australia (*Griffin et al.*, 2001).

### 4.8.1 SST and D20 anomalies along XBT section IX1

Figures 46 and 47 show Hovmoeller diagrams of observed and simulated SST and D20 anomalies. SST anomalies are quite well simulated by the model, although the mean amplitude seems to be larger in the model than in the observations. The phases of major events such as the 1982-83, 1986-87, 1997-98 El Niños and the 1984-85, 1988-89 La Niñas are well captured by the model in both SST and D20 anomalies.

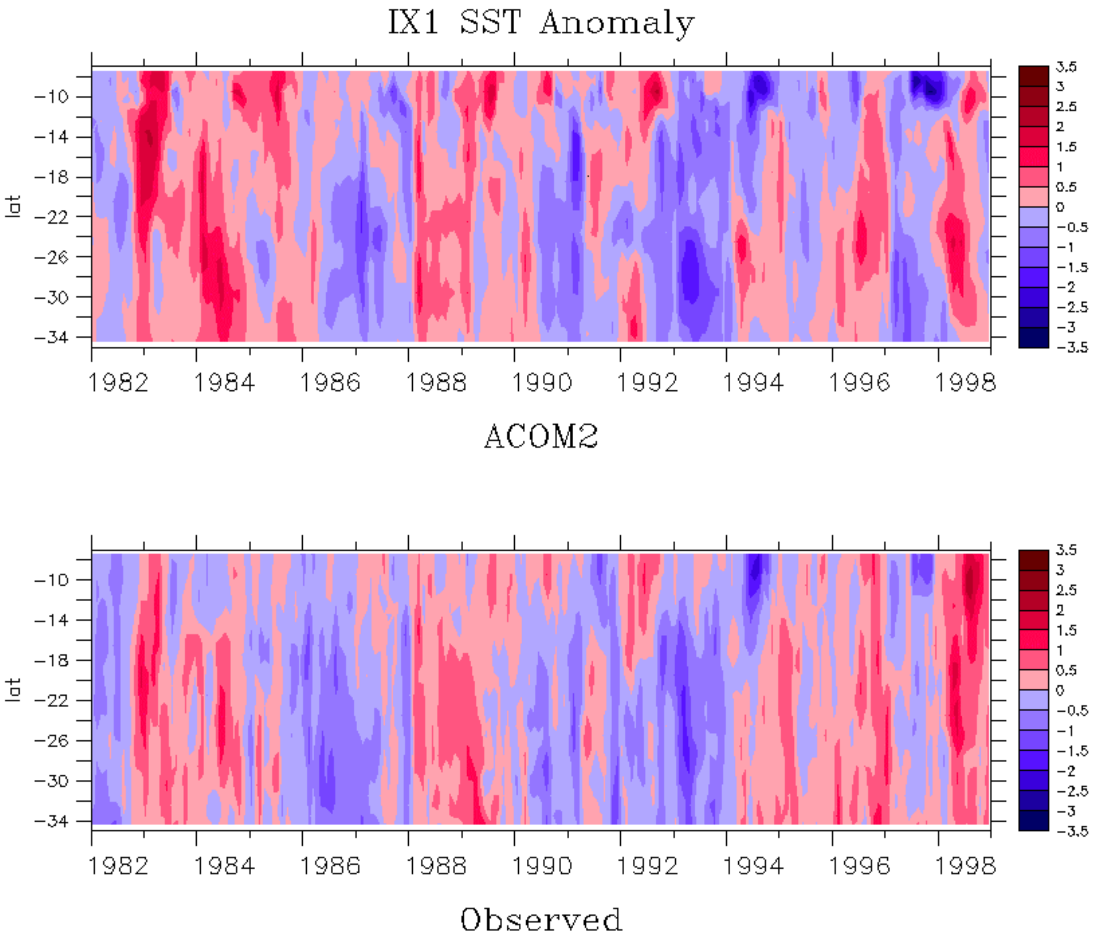

**Figure 46: SST anomalies along XBT section IX1. Top: model, bottom: observations (Reynolds data). Units are in °C.**

Whereas amplitudes in SST anomalies are quite coherent along the section, large signals in D20 anomalies are confined to the Australian coast, indicating the propagation of interannual signals from the Pacific via the ITF into the southern parts of the Leeuwin Current (*Clarke and Liu,* 1994; *Meyers*, 1996). Note that the simulated anomalies of D20 anomalies are much larger than observed. This might indicate a problem in the model (see also the bias in the seasonal cycle of D20 in Fig. 14), although temporal smoothing of the observations contributes to the discrepancies as well. Note, however, that D20 is a difficult quantity to interpret as one approaches the subtropics, since it begins to get very shallow there and can surface. Since D20 can be within or near the mixed-layer small errors in the temperature profile can lead to large errors in D20.

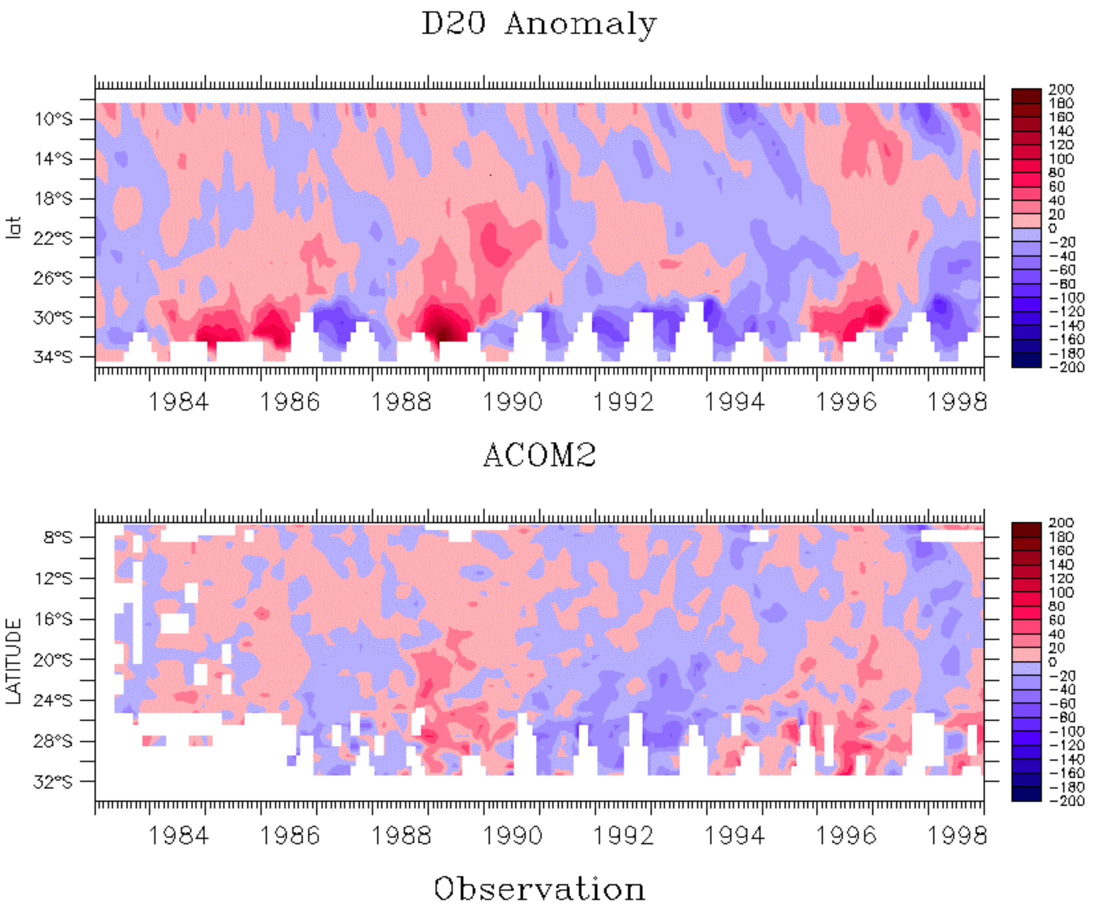

**Figure 47: D20 anomalies along XBT section IX1. Top: model, bottom: observations. Units are in m.**

### 4.8.2 Transport variability along XBT section IX1

Observed and simulated geostrophic transport anomalies are displayed in Fig. 48. Here we focus on the 0-400m depth range; the corresponding time series for the 0-700m depth is much shorter and less informative. We first note that interannual anomalies are about as large as their seasonal cycle (Fig.15). The agreement between model and observations is almost non-existent, as expressed in the correlation coefficient (r = 0.1). Furthermore, simulated amplitudes are typically about twice as large as observed and variability is also quite different (standard deviations are 5.2 Sv for the model and 2.6 Sv for XBT data). A possible explanation for these discrepancies might be differences in the large-scale "real" and "observation-based" wind stresses; the latter has been used to force the model.

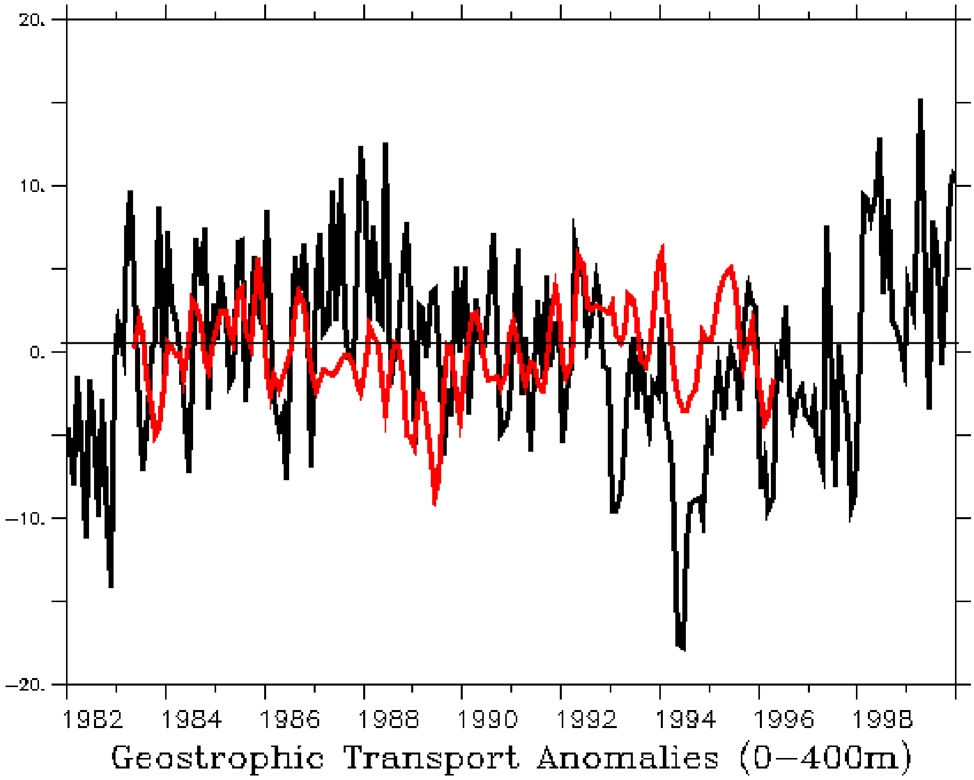

**Figure 48: Geostrophic transport anomalies (0-400m) along XBT section IX1. Black: model, red: observations. Units are in Sv.**

## 4.9 Indian Ocean: SST, SSH and D20 anomalies along XBT section IX12

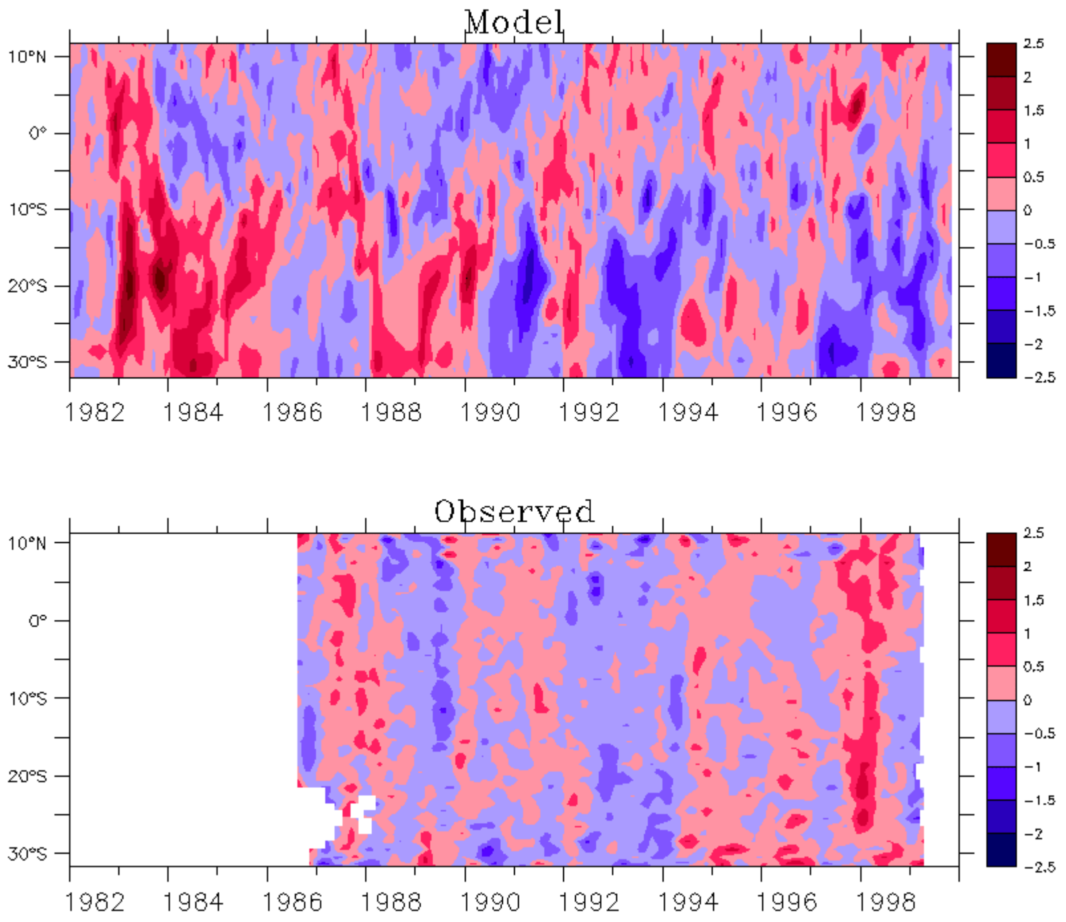

**Figure 49: Simulated and observed (Reynolds data) SST anomalies along IX12 section. Contour interval is 0.5° C.**

Quite similar to the IX1 section, simulated SST anomalies along section IX12 (see Fig. 16 for location) are significantly larger than observed (Fig. 49). Also there is less agreement in the phases of individual events, such that the simulated warm SST anomalies in 1988-89 and the cold anomalies in the early 90s and in 1997-98 are barely visible in the observations. The main reason for these discrepancies seems to be the strong dependence of Indian Ocean SST dynamics on surface forcing fields (winds, and particularly solar shortwave radiation). As these observation-based quantities are known to contain significant errors the resulting SST anomalies show differences to the observed SST. Another reason might be deficiencies in the model's upper ocean physics.

The agreement improves for quantities that describe integral and subsurface properties such as SSH and D20 anomalies (Fig. 50). Amplitudes and phases of observed and simulated SSH anomalies agree surprisingly well, while the interannual variability of the annual Rossby wave seen in the model is missing in the observations (*Masumoto and Meyers*, 1998).

**Figure 50 (next page): IX12 section. Top: observed and simulated SSH anomalies. Contour interval is 0.05m. Bottom: simulated and observed D20 anomalies. Contour interval is 20m.**

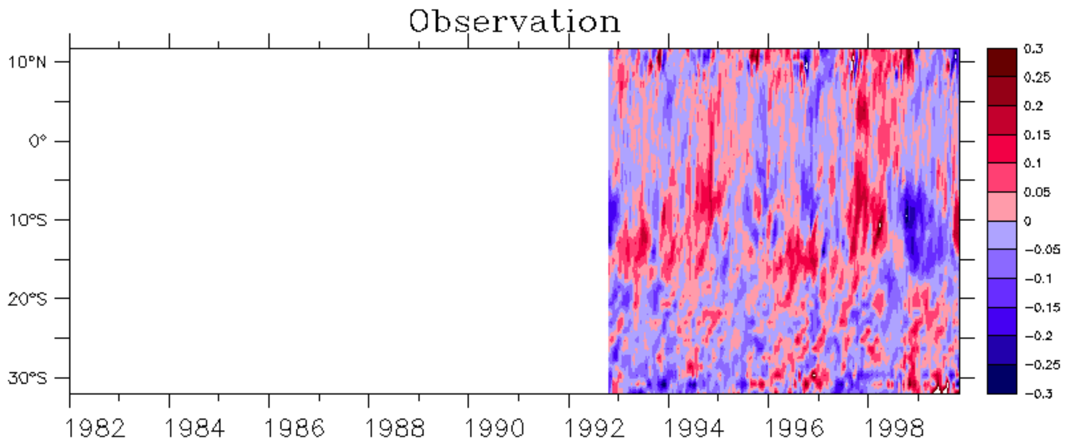
Observation
10°N
0°
10°S
20°S
30°S
1982
1984
1986
1988
1990
1992
1994
1996
1998
0.3
0.25
0.2
0.15
0.1
0.05
0
−0.05
−0.1
−0.15
−0.2
−0.25
−0.3

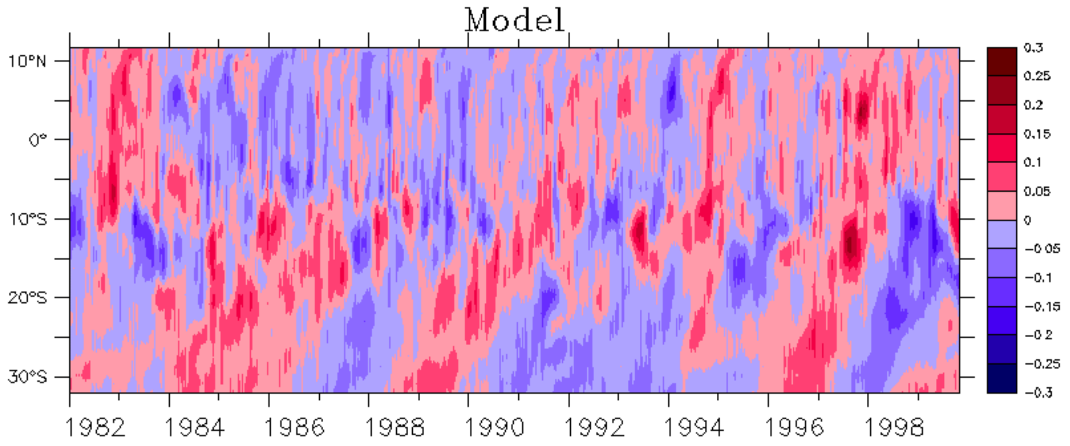
Model
10°N
0°
10°S
20°S
30°S
1982
1984
1986
1988
1990
1992
1994
1996
1998
0.3
0.25
0.2
0.15
0.1
0.05
0
−0.05
−0.1
−0.15
−0.2
−0.25
−0.3

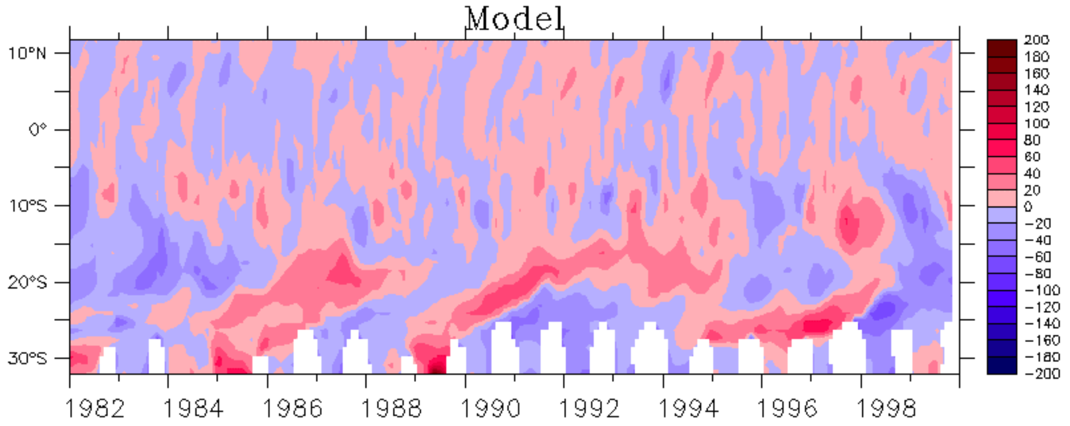
Model
10°N
0°
10°S
20°S
30°S
1982
1984
1986
1988
1990
1992
1994
1996
1998
200
180
160
140
120
100
80
60
40
20
0
−20
−40
−60
−80
−100
−120
−140
−160
−180
−200

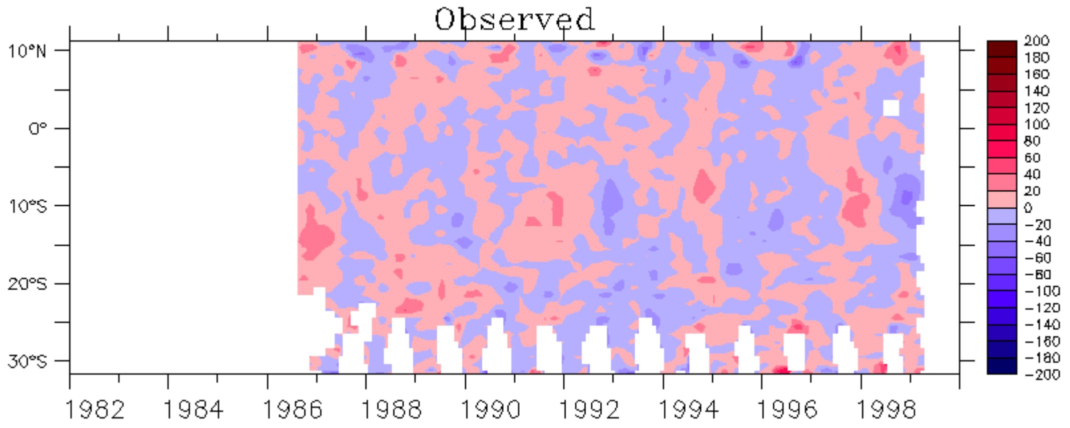
Observed
10°N
0°
10°S
20°S
30°S
1982
1984
1986
1988
1990
1992
1994
1996
1998
200
180
160
140
120
100
80
60
40
20
0
−20
−40
−60
−80
−100
−120
−140
−160
−180
−200

# 5. COMPARISON OF THE ACOM2 MODEL WITH THE OLD ACOM1 MODEL

This section addresses differences between the new and old ACOM model. First, the assimilation statistics between the two models are compared. Improved statistics based on model data from ACOM2 provides better initial conditions for coupled forecast runs. The second part of this section describes the mean states of the ocean models as part of the coupled ocean-atmosphere system.

## 5.1 Comparative statistics from the assimilation

Every 10 days the assimilation is performed by combining the observations with the model's background field. The model background field is a 10 day forecast from the previous analyses using FSU stresses. Just before the observations are inserted we calculate the departures of the background from all observations (ones that pass quality control, QC). This gives a measure of how well the model background agrees with the independent observations (independent since they have not yet been assimilated). We consider statistics regarding the QC , i.e. the percentage of observations that fail (quality control is performed by comparing the observations against the model background). A better model would lead to lower observations failing the quality control and to smaller background errors. Figure 51 shows the data rejection statistics for the NINO3 and NINO4 regions and the Equatorial Pacific Ocean as a whole. In all cases the ACOM 1 model is rejecting more data than ACOM 2, which suggests the former model has greater systematic error in the equatorial region.

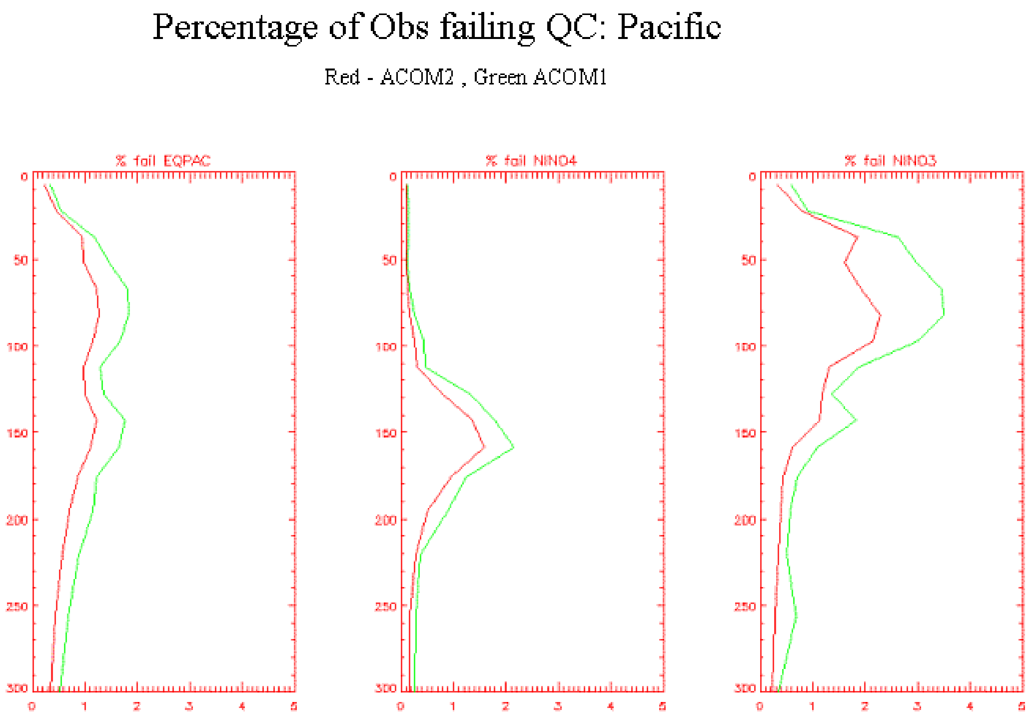

**Figure 51 (previous page): Percentage of data rejected as a function of depth for (left) the equatorial Pacific (5S-5N); (middle) the NINO4 region 150E-150W, 5S-5N; and (right) the NINO3 region 150W-90W, 5S-5N. Red: ACOM2, green: ACOM1.**

Figure 52 shows the root-mean-square (rms) and mean of the errors taken over different horizontal regions. rms indicates a magnitude of the background error and the mean indicates the model background bias. Note: the background error depends on model error, forcing error and the previous assimilation. Shown is the full field over 1992-1996, as well as the mean over this period. The data have also been broken down into seasonal cycle and interannual anomalies (only for period 1992-1995).

EQPAC (10S to 10N) rms Background - Obs Statistics:

TOP (green)- ACOM1 , Bottom (red)- ACOM2

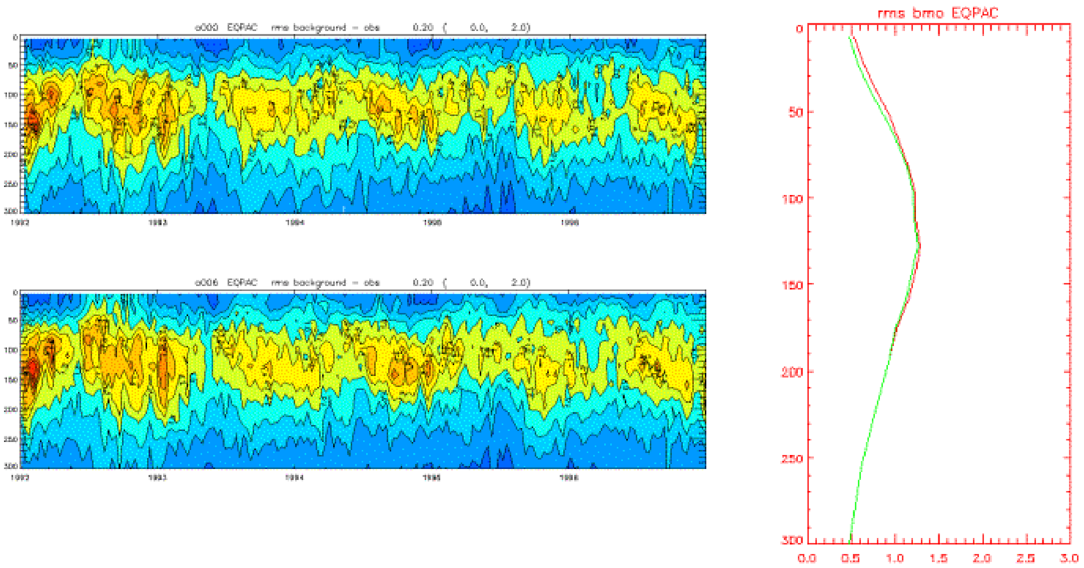

EQPAC (10S to 10N) Mean Background - Obs Statistics:

TOP (green)- ACOM1 , Bottom (red)- ACOM2

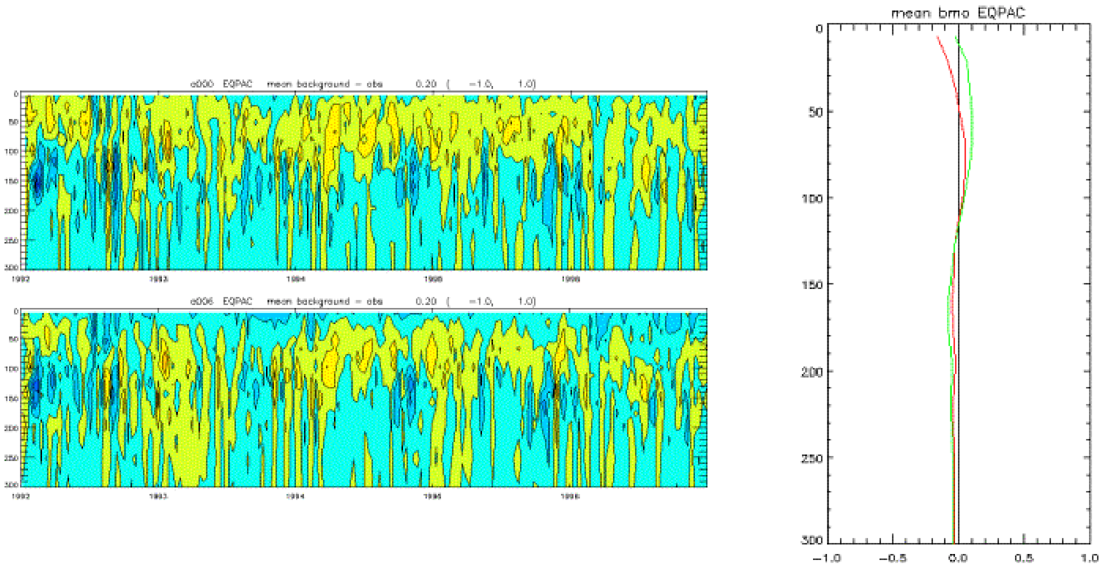

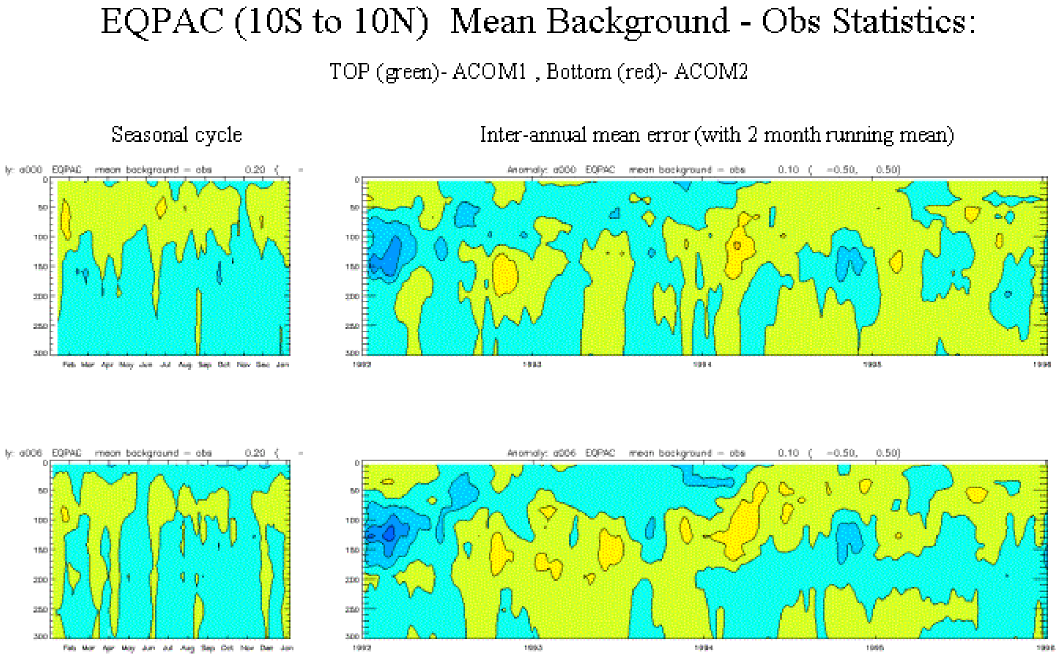

**Figure 52: Plots of assimilation statistics as a function of depth for the equatorial Pacific region for (top) ACOM 1 and (bottom) ACOM 2. The mean of the entire period is shown at the right.**

The rms differences are quite similar, with ACOM 1 having slightly smaller errors near the surface. The rms differences have interannual variability, related to variability of thermocline. Also seen is a decrease in background error with time, for example compare the first couple of years with the last two. This is because of the build up of the TOGA-TAO observing network over this period. More observations lead to a better analysis and hence better 10-day forecasts and therefore lower background errors.
The bias of ACOM 2 is greatest at the surface but significantly better at the depth of the thermocline. We have identified a difference between the two models in the shortwave forcing that contributes to the ACOM 2 surface error. The mean seasonal differences (left columns of bottom panels) and anomalies (right columns) suggest a significant portion of the ACOM 1 errors come from the seasonal cycle.

In fact ACOM2 may be better than ACOM1 at the surface even though the errors are greater. This is because ACOM2 takes account of sub-surface solar penetration by taking heat from the surface layer and adding it lower down and ACOM1 does not. But in the runs performed here the ocean was not forced with a solar flux and hence why the ACOM2 looks worse, i.e. it goes too cold at the surface. In future runs ACOM2 will be forced at the surface with NCEP surface radiation and heat fluxes (results from a new run with NCEP fluxes do reduce the ACOM2 errors at the surface, figures not shown).

## 5.2 Coupled model mean states

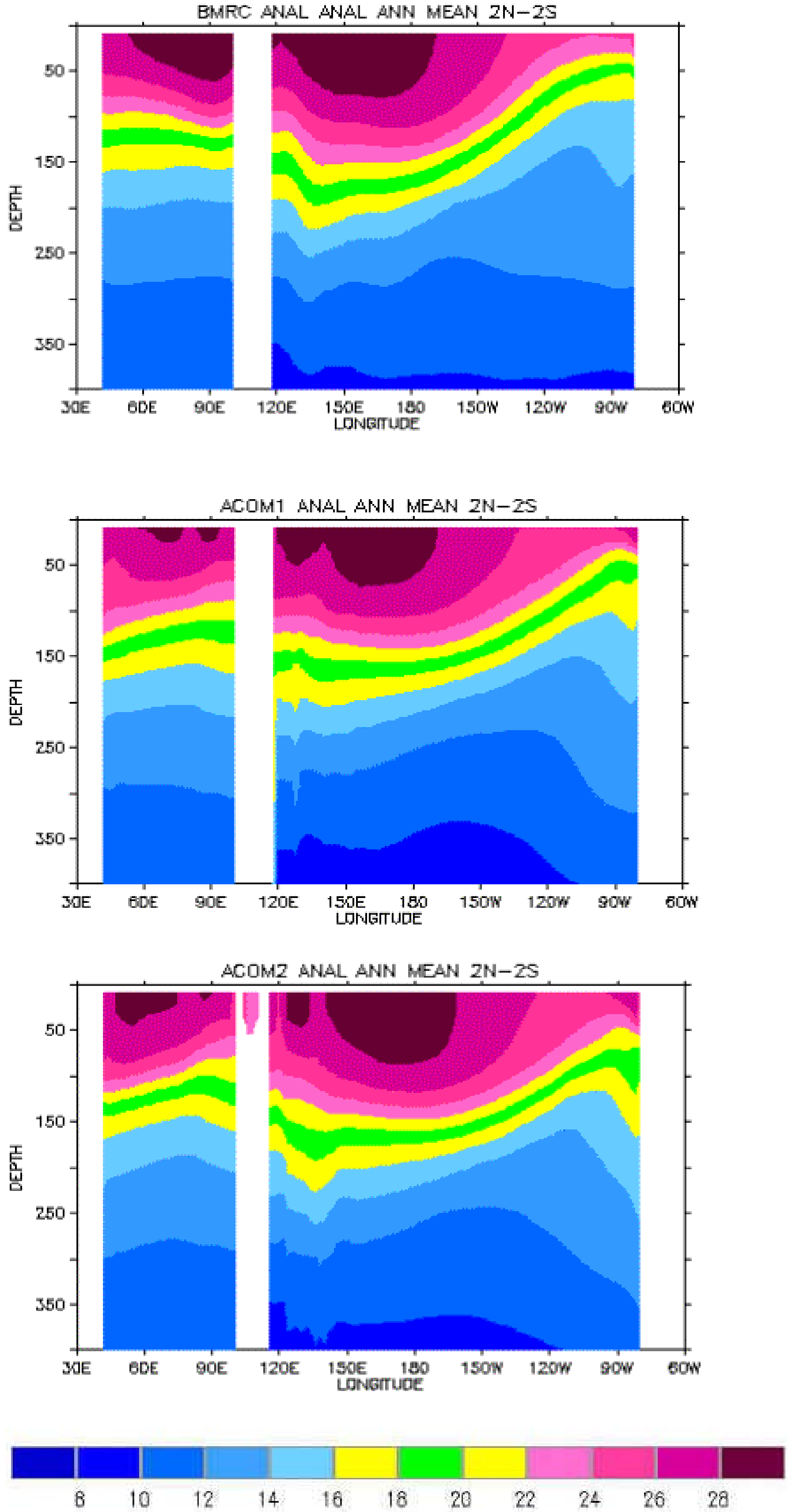

**Figure 53 (previous page): Annual mean longitude-depth sections at the equator (thumbnails) from (a) the BMRC sub-surface analysis, (b) 60 coupled model 6-month lead forecasts with ACOM 1, and (c) as (b) but with ACOM 2.**

Figure 53 shows the mean longitude-depth sections of subsurface temperature in the equatorial region (2° S - 2° N mean) from the BMRC analysis and CM1 (coupled model using ACOM1) and CM2 (coupled model using ACOM2) hindcasts. The data from the coupled hindcasts are six months lead forecasts initialised at Feb, May, Aug and Nov of years 1981 through 1995 (sixty in total); and the corresponding 60 monthly means are used for the analysis. From Fig. 53 the overall improvement of CM2 compared to CM1 includes slightly better thermocline gradient over the central to western Pacific and shoaling of the thermocline depth towards western Pacific boundary.

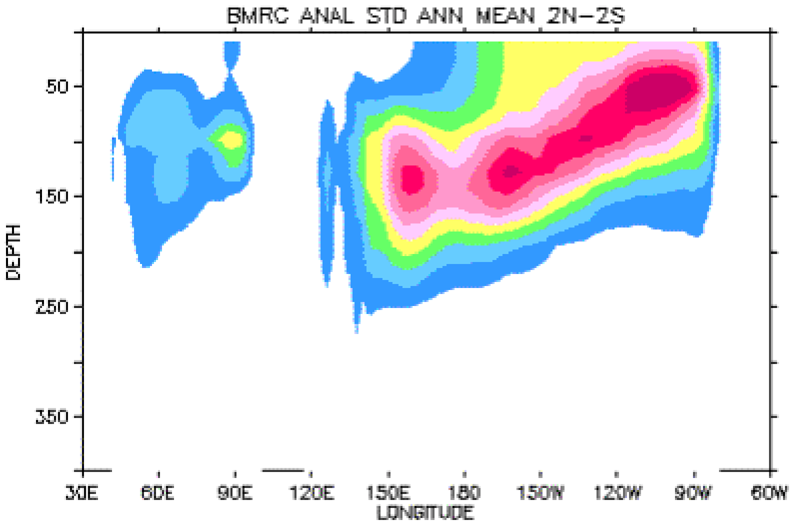

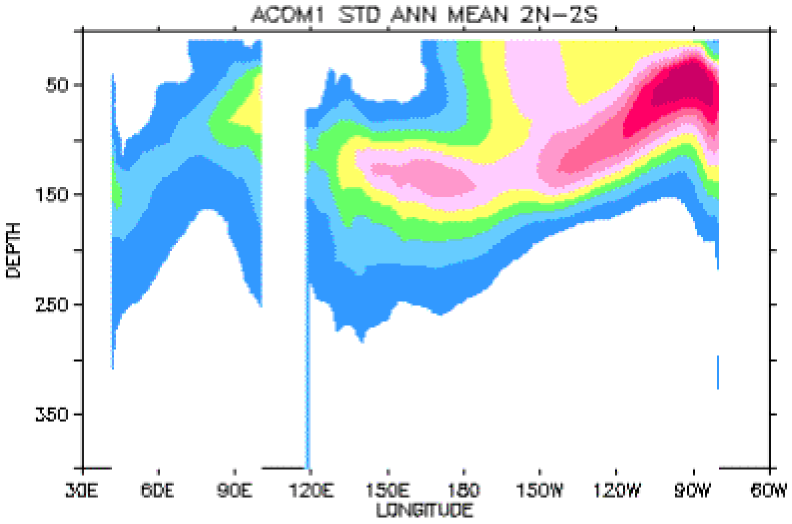

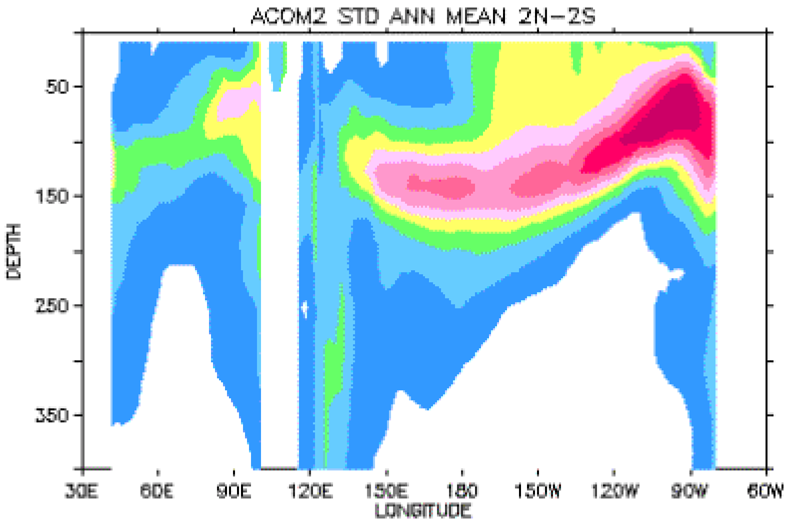

**Figure 54: Standard deviation of the fields shown in Fig. 53. Contour interval is 0.25º C.**

The variabilities of sub-surface temperature from the model forecasts at six months lead-time (CM1 and CM2) and from the analysis are shown in Fig. 54. The observed variability shows a maximum around the depth of the thermocline with typical amplitudes of 1.5 to 2° C. Lack of variability towards the eastern coastal region in the BMRC analysis is due to the lack of observations in this region, so that the analysis has actually gone back to the background or climatology. The two coupled model results show increasing variability right across to the east boundary, which is consistently following the depth of the thermocline where larger variability is expected due to stronger temperature gradients as seen in Fig. 53. The variability over the central and western Pacific is stronger in CM2 than that in CM1, possibly due to sharper thermocline gradients in CM2 then that in CM1 as seen in Fig. 53. Still, both models have too weak variability in the central Pacific.

It is seen in Fig. 55 that both coupled models can produce skilful forecasts compared with persistence for all lead times. CM2 appears to have slightly higher skill compared with CM1. Using a correlation of 0.6 as the threshold for useful forecasts then the maximum lead-time for useful NINO3 anomaly forecasts would be 11 and 9 month for CM2 and CM1 respectively; that is, an increase of 1-2 months in useful lead time (but note that with such a limited number of cases there is considerable uncertainty in these skill estimates; statistical significance of the differences has not been calculated).

Figures 56 and 57 show NINO3 SST autocorrelation skill, standard deviation of the 6-month forecasts with NINO3 SST and global pattern of correlation skill for ACOM1 and ACOM2 at lead times of six months, respectively. All figures indicate an improvement in ACOM2 over ACOM1 in the tropical Pacific.

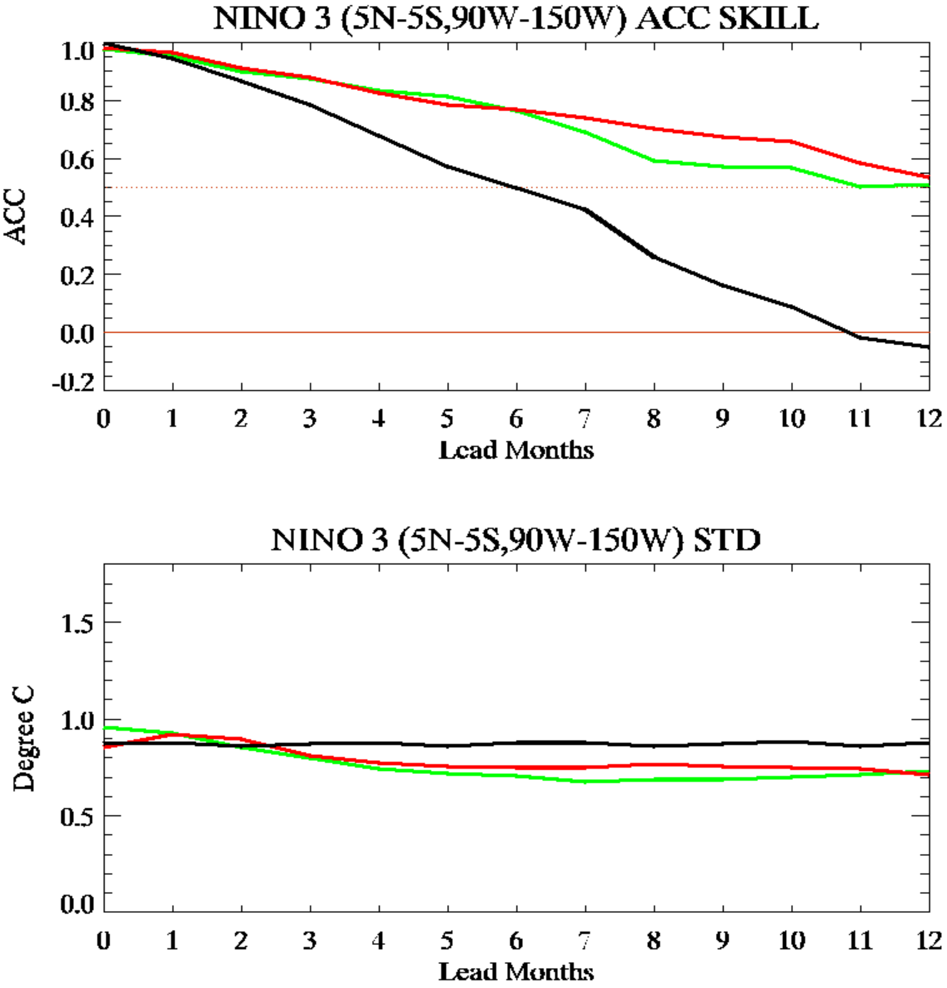

**Figure 55: The autocorrelation (top) and standard deviation (bottom) of the 6-month forecasts with NINO3 SST. Observations used for verification are Reynolds data. Persistence is shown in black, the CM1 model in green, and the CM2 model in red. Note the increase in skill between 6 to 12 months of lead time (top). This period also corresponds to enhanced variability (bottom), which improves agreement with observations.**

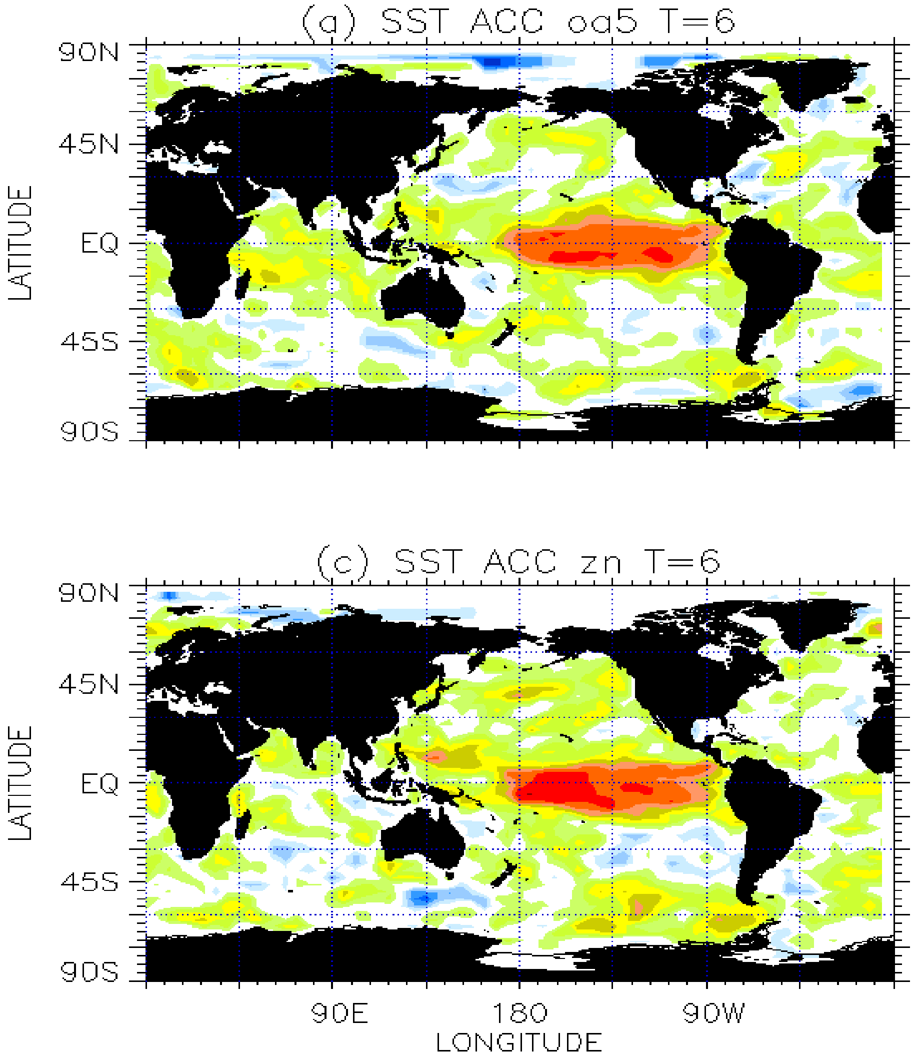
(a) SST ACC oa5 T=6

(c) SST ACC zn T=6

**Figure 56: Global spatial pattern of correlation skill at lead time of six months by ACOM1 (top) and ACOM2 (bottom). Skill increase is seen in ACOM2 in the central equatorial Pacific region and some spots in the west, north and south Pacific.**

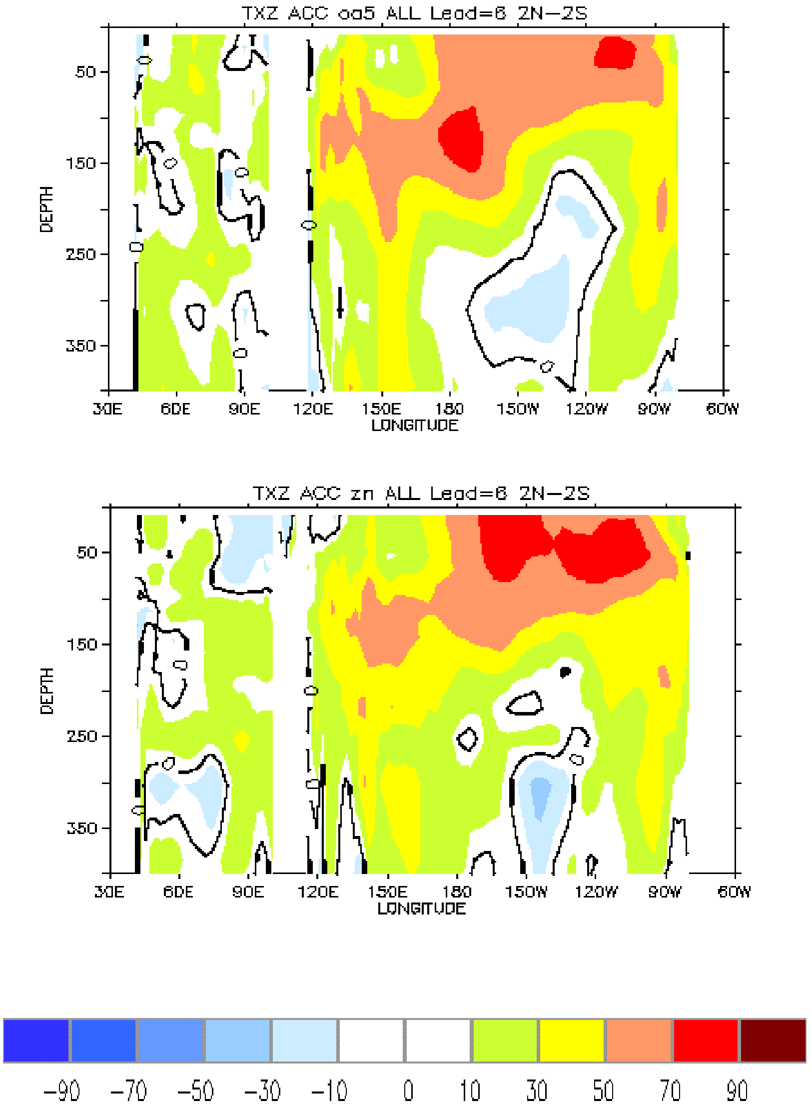

**Figure 57: Depth-longitude section of skill along equatorial Pacific at six months lead times by ACOM1 (top) and ACOM2 (bottom). Higher skill is found in ACOM2 in the central and eastern subsurface areas of the Pacific.**

# 6. SUMMARY

In this report we have used a variety of observational data - satellite based SST and sea-level records, XBT sections, mooring data and observed salinity climatology - to check on the performance of the ACOM2 global ocean model, with particular reference to its suitability as the ocean component of a coupled model for predicting global and Australian climate. Most of the report concentrates on the "ACOM2daily" run, in which daily wind stresses from NCEP were interpolated into monthly mean wind stress estimates from Florida State University. This report is written to meet a deadline, and work will be continued on some remaining "loose ends". Some highlights are as follows:

Large scale patterns in the Pacific and Indian Oceans:

These were generally quite well simulated. These include:
- annual mean temperature (Fig. 1). Heat flux corrections have been applied to ensure this, but:
- annual mean surface heat fluxes are generally within the known errors of climatological estimates.
- Depth-integrated steric heights agree well with observations (Fig. 4), except that the trough between the North Equatorial Current and Countercurrent is a few degrees too far north and is too strong in the model. The most likely cause is an error in the mean FSU winds, since these mean patterns are probably determined by simple Sverdrup physics.
- The model overestimates the depth of the 20° C isotherm (Fig. 5), part of a general overestimate of thermocline depth.
- The spatial patterns of the seasonal cycle of heat content (0-400m) are quite well simulated, but their amplitude is underestimated somewhat (Fig. 7).
- Annual mean sections of temperature (Fig. 8) and salinity (Fig. 10) along the equatorial Pacific show systematic differences from observations in the east Pacific. These may reflect model problems in simulating spasmodic water mass formation in the far east Pacific (Figs. 43-45); further work will be done to explore this possibility.
- Patterns of correlation of observed sea-level anomalies with model anomalies (Figure 18b) and SST anomaly (Figs. 21b, 22b) both show typical values of order 0.6 in the tropics for the "ACOM2daily" run (exceeding 0.8 in places). A run with FSU monthly winds only (Figs. 21a, 22a) show much reduced correlations for SSTA, especially in the far west Pacific where correlations become negative. These regions roughly coincide with places in which correlations (Figs 24) and regressions (Fig. 25) of SSTA on NINO4 SSTA - a good measure of the ENSO-related SST variability - have the wrong sign in the model compared to observation. These occur near places where winds are thought to have errors (Fig. 4). A run with "ACOM2 daily" fluxes but with substantially greater horizontal resolution (Figs. 18c, 21c, 22c) shows little improvement over ACOM2, in simulating these correlation patterns (though it greatly improves simulation of coastal currents round, e.g., Australia).
- Seasonal versions of Fig. 24 (Figs. 26-29) show that the ACOM2daily run does not simulate the observed seasonal reversal of sign of SSTA regressions with NINO4, near and just south of Indonesia. Thus the simple hypothesis that this reversal is due to a seasonal change in the effect of a given wind anomaly on evaporation (e.g. *McBride et al.*, 2001) needs reconsidering, since this mechanism is included in the ACOM2daily run.
- SSTA patterns at 3 monthly intervals during the massive 1997/98 El Niño/La Niña event are quite well simulated (Figs. 30, 31), as are comparable sea-level anomaly patterns (Fig. 33); and

RMS errors in height anomaly are usually not more than twice the known uncertainy in the observations (Fig. 32).

Results from XBT sections and moorings:

These are harder tests of the model (and of the wind stress and flux patterns used to drive it). Near (0°, 140° W), near where correlations in the above figures are generally largest, the model performs well in simulating temperatures (Figs. 37 and 39). Simulations are somewhat less successful at (0°, 110° W), as might be expected from correlation diagrams like Figs. 18, 21 and 23. Nevertheless, correlations between observed and simulated anomalies in D20 still reach 0.86 and 0.76, respectively.

The seasonal cycles of SST and D20 along XBT sections IX1 and IX12 (Figs. 13 , 14, 49, 50) are reasonably simulated by the model. Typical differences of 20-30m exist for D20 in the centre of the XBT sections. The seasonal cycle of simulated geostrophic transport across XBT section IX1 (0-700m) is –3.8 Sv and compares well with the observations (-3.2 Sv, Fig. 14). The observed phases of interannual anomalies in SST and D20 are captured by the model (Figs. 46 and 47), but almost no correlation exists between simulated and observed geostrophic transport anomalies (Fig. 48).

Comparison of the ACOM2 model with the old ACOM1 model:

We have not applied the tests discussed above to the ACOM1 model, since it was not possible to extract a version of the older model from its coupled version in a form for which these tests could be meaningfully performed. Our tests of ACOM1 vs. ACOM2 are therefore somewhat restricted. However, it was found that when data assimilation was applied, ACOM2 rejected less data in all cases, suggesting that it had smaller systematic errors in the equatorial region. RMS differences between the models with and without assimilation were small, though ACOM2 has significantly less bias near the thermocline. Hindcasts - i.e. forecasts done retrospectively, starting 6 months before measurement time - were averaged from 1981 through 1995 for the coupled models based on ACOM1 and ACOM2, and compared with observations (Fig. 53). ACOM2 performs better than ACOM1 in the west Pacific Ocean, but neither model performed well in the east Pacific (probably reflecting problems discussed in connection with Figs. 43-45), or in the Indian Ocean. Here the coupled models may be generating erroneous easterly winds along the equator, to balance the zonal pressure gradients implied by the east-west slope of isotherms in Figs. 53b,c in the Indian Ocean. The two models are again similar in their patterns of variability (Fig. 54), differing markedly from the BMRC analysis - though the latter underestimates variability in places, since it returns to climatology when data are lacking. Initial estimates of coupled model forecast skill show indications that the coupled model using ACOM2 is at least as skillful, if not more skillful, than the coupled model using ACOM1. Improvements in ACOM2 contribute to forecast skill in two ways: firstly through the coupled model itself and secondly through improvements to the initial states since the data assimilation cycle also uses ACOM2.

Attempted attribution of errors to stress fields or model error:

The uncertainties in the "observed" momentum, heat and freshwater fluxes applied to the model limit our ability to tell what errors are due to those flux fields, and what to model error.

Momentum fluxes seem particularly suspect near 10° N in the Pacific. The only errors that seem definitely ascribable to the ocean model are:

- The model's thermocline is too deep. This is not confined to the equatorial region, but occurs throughout the region where 20° C water is found (Fig. 5). Part of the problem might be associated with too strong vertical mixing, although Wilson's (2000) parameterisation (see Appendix) helps to mitigate the problem.
- Mean model temperature and salinity show features in the eastern Pacific Ocean that differ markedly from observation (Figs. 8, 10). These are thought to be associated with equatorial mixing events in the model. Further work is needed to clarify this issue.

# 7. APPENDIX

## 7.1 Model details

ACOM2 includes the following features:

- the Chen mixing scheme
- Atmospheric Boundary Layer Model (ocean-only)
- a scheme for solar shortwave penetration
- Mediterranean and Red Sea outflows simulated by relaxation to Levitus data
- tidal mixing parameterisation in the Indonesian region
- careful representation of islands and straits in the Indonesian region
- viscosity in Lombok Strait tuned to give observed fraction of total Indonesian throughflow

The **grid spacing** is 2 degrees in the zonal direction. The meridional spacing is 0.5° within 8° of the equator, increasing gradually to 1.5° near the poles. There are 196 grid points from south to north and 182 grid points from west to east.

There are 25 levels in the vertical, with 12 in the top 185 metres. The maximum depth is 5,000 metres. The level thicknesses range from 15 metres near the surface to almost 1,000 metres near the bottom.

The **bathymetry** of the model represents a smoothed approximation to the high-resolution data set of *Gates and Nelson* (1975). To simulate the Indonesian Throughflow we modified the model's topography in that area, allowing for a transport of water masses through Lombok Strait and the Timor Sea. Because islands are computationally expensive in this version of the GFDL model only the Philipines, Kalimantan, Celebes, the Lombok-Flores islands, Australia (combined with New Guinea), New Zealand and Antarctica are separated from the remaining land points. There is no Bering or Torres Strait. The Drake Passage was artificially widened to aid throughflow of the Antarctic Circumpolar Current. See *Schiller et al.* (1997) for further information.

An **Atmospheric Boundary Layer Model** (ABLM) has been used to create surface fluxes for the ocean-only experiments described in this report. It is NOT used in the coupled version of ACOM2 and BAM. The ABLM provides net surface heat fluxes (based on heat flux components) to the ocean model. The boundary layer model contains a prognostic advection/diffusion equation for air temperature in the atmospheric mixed layer. Within the boundary layer, air temperature is determined by a balance between surface fluxes, horizontal advection by imposed winds, entrainment from above the mixed layer, horizontal diffusion and radiative cooling. Use of the Atmospheric Boundary Layer Model (ABLM) leads to improved simulations of SST and its anomalies compared to simpler surface boundary parameterisations. The code was provided by R. Kleeman (BMRC, Melbourne). A detailed description is given in *Kleeman and Power* (1995).

The **inflows of the Red Sea into the Indian Ocean and the Mediterranean Sea into the Atlantic** Ocean significantly change the water mass structures of these oceans. Because the Red and Mediterranean Seas are not included in this model the inflows are simulated by applying a restoring of the model temperature and salinity to observed values (*Levitus*, 1982) at the lateral boundaries between the respective seas and oceans. The grid cells at which this is done are "hard-wired" into the model code. Should changes be made to the model grid, some care needs to be taken in choosing the exact grid cells at which this relaxation should take place. The model code is easily adaptable for different grids.

Vertical mixing and vertical friction in the model are parameterised by using the one-dimensional ***Chen et al.* (1994) mixing scheme**. Strong mixing is assumed to occur within a bulk mixed layer, as in *Niiler and Kraus's* (1977) model. Below the mixed layer, internal mixing is decribed by a gradient Richardson-number dependent mixing that uses a parameterisation based on observations by *Peters, Gregg and Toole* (1988) (*Wilson*, 2000). Their parameterisation shows a sharper drop-off towards higher Richardson-numbers, which particularly improves the model performance at lower latitudes. The hybrid structure of this mixing scheme allows its application to high latitudes (where mixing is strongly influenced by the bouyancy fluxes of heat and freshwater, and thus the Niiler-Kraus part is assumed to be dominating); it is also applicable to the equatorial ocean (where vertical mixing is predominantly determined by large vertical current shears, and thus the gradient Richardson-number part is assumed to be dominating). The Chen et al. mixing scheme uses the surface fluxes of heat, freshwater and momentum as input to compute the mixed-layer depth and to determine the vertical diffusion and viscosity coefficients within the whole water column. The maximum values for viscosity and diffusivity in the mixed layer are set to 266.0 x 10^-4m2/s and 199.0 x 10^-4m2/s, respectively. The background values (i.e. the smallest possible values for viscosity and diffusivity) are set to 0.2 x 10^-4m2/s and 0.01 x 10^-4m2/s, respectively. The level version of this mixing scheme has been implemented in the MOM model by Richard Kleeman at the Bureau of Meteorology Research Centre, Melbourne (*Power et al.*, 1995). The gradient Richardson-number parameterisation of Peters, Gregg and Toole was made available to us by Steve Wilson, CSIRO Division of Atmospheric Research, Melbourne (*Wilson*, 2000). For a detailed discussion of the *Chen et al*. (1994) mixed-layer model in its level version and tests with observed data we refer to the CSIRO report of *Godfrey and Schiller* (1997).

Due to the large changes in grid sizes of the model (enhanced tropical grid and coarse resolution close to the poles), and in order to guarantee numerical stability, the **zonal and meridional viscosity** are dependent on latitude. The modifications are similar to changes which *Power et al.* (1995) applied to another version of the MOM(1) model. The meridional viscosity is set to 2.0 x 10^3 m2/s near the equator but then increases to 1.0 x 10^5 m^2/s at high latitudes while the zonal viscosity is constant (2.0 x 10^4 m^2/s). The horizontal diffusivity is set to 1.0 x 10^3 m^2/s everywhere.

The **viscosity in Lombok Strait** is also increased to better simulate the observed transport through the Indonesian Archipelago. To achieve this the meridional viscosity in Lombok Strait is increased by a factor of 8. This reproduces the observed ratio of volume transport through Lombok Strait (20%) to that through the Timor Sea (80%).

As water flows from the Pacific to the Indian Ocean, the **tidally induced vertical mixing** in the Indonesian archipelago is able to change the water mass structure of the Indian Ocean significantly. An analysis by *Ffield and Gordon* (1996) suggests that the center of the tidal mixing effect on SST is located in the Banda Sea. To simulate this observed feature, the vertical mixing coefficients (diffusion and viscosity) in the Indonesian area were increased. The centre of the additional tidal mixing in the model is located in the Banda Sea and has a maximum value of 2 x 10^-4 m^2/s; it gradually decreases as the distance from the Banda Sea increases. The additional mixing is independent of time, that is, no attempt is made to resolve the timescales associated with its physical origin. This is legitimate as long as one is only concerned with its larger time scale effects on SST.

An observation-based climatology of turbidity (CZCS) is used to estimate the subsurface decay rate for the **heat flux penetration**.

The model produces **netCDF output files** of time mean fields or snapshots of the following variables: Potential Temperature, Salinity, Velocity, Surface Net Heat Flux, Surface Freshwater Flux, Wind Stresses, Streamfunction (rigid lid option) or Surface height and vertical velocity at surface (implicit free surface option). Output data can be written as separate files or as concatenated files (see namelist output).

The model code and some forcing fields are available from the ACOM web page at http://www.marine.csiro.au/acom/index.htm.

## 7.2 Namelist file

```
set days  = $DAYS
set diag  = 3.0
set diag1 = 30.416666666666666
set diag2 = 10.0
set diag3 = 1.0

set NAMELIST_EOF = "/"

cat > namelist.contrl << ENDNAMELIST
 &contrl init=.false., runlen=$days, rununits='days',
         restrt=.true., initpt=.false.,
 $NAMELIST_EOF
ENDNAMELIST

cat > namelist.mbcin << ENDNAMELIST
  &mbcin $NAMELIST_EOF
ENDNAMELIST

cat > namelist.tsteps << ENDNAMELIST
 &tsteps dtts=900.0, dtuv=900.0, dtsf=900.0,
 $NAMELIST_EOF
ENDNAMELIST

cat > namelist.riglid << ENDNAMELIST
 &riglid mxscan=2000, sor=1.60, tolrsf=1.0e8, tolrsp=1.0e-4,
         tolrfs=1.0e-4,
 $NAMELIST_EOF
ENDNAMELIST

cat > namelist.mixing << ENDNAMELIST
 &mixing am=2.e7, ah=1.e7, ambi=1.e23, ahbi=5.e22,
         kappa_m=20.0, kappa_h=1.0, aidif=1.0,
         nmix=17, eb=.true.,  ncon=1, cdbot=0.0,
         acor=0.5,
         dampts(1)=7.0, dampts(2)=7.0 ,
         dampdz(1)=15.00e2, dampdz(2)=15.00e2,
 $NAMELIST_EOF
ENDNAMELIST

cat > namelist.isopyc << ENDNAMELIST
 &isopyc $NAMELIST_EOF
ENDNAMELIST

cat > namelist.blmix << ENDNAMELIST
 &blmix $NAMELIST_EOF
ENDNAMELIST

cat > namelist.hlmix << ENDNAMELIST
 &hlmix $NAMELIST_EOF
ENDNAMELIST

cat > namelist.chmix << ENDNAMELIST
 &chmix  fricmx=0.0, diff_cbt_back=0.01, visc_cbu_back=0.2,
         visc_cbu_limit=266.0, diff_cbt_limit=199.0,
 $NAMELIST_EOF
ENDNAMELIST

cat > namelist.diagn << ENDNAMELIST
 &diagn  tsiint=$diag3,
         tavgint=$diag,  itavg=.false.,
         tmbint=$diag,   itmb=.false.,
         trmbint=$diag,  itrmb=.false.,
```

```
         snapint=$diag, snapls=-90.0,  snaple=90.0,   snapde=5000.0e2,
         timavgint=$diag,
         glenint=$diag,  vmsfint=$diag, stabint=$diag, zmbcint=$diag,
         gyreint=$diag,  extint=$diag, prxzint=$diag, dspint=$diag,
         trajint=$diag3,  xbtint=$diag, exconvint=$diag,
cmixint=$diag,
 $NAMELIST_EOF
ENDNAMELIST

cat > namelist.io << ENDNAMELIST
 &io     expnam='MOM2_GLOBAL',
         iotavg=$iotavg, iotmb=$iotmb, iotrmb=$iotrmb,
         iozmbc=$iozmbc,
         ioglen=$ioglen, iovmsf=$iovmsf, iogyre=$iogyre,
         ioprxz=$ioprxz, ioext=$ioext,   iodsp=$iodsp,
         iotsi=$iotsi,   iotraj=$iotraj, ioxbt=$ioxbt,
 $NAMELIST_EOF
ENDNAMELIST

cat > namelist.ictime << ENDNAMELIST
 &ictime eqyear=.false., eqmon=.false., refinit=.true.,
         year0=1962, month0=1, day0=1, hour0=0, min0=0, sec0=0,
 $NAMELIST_EOF
ENDNAMELIST

cat > namelist.output << ENDNAMELIST
 &outfiles separate_files=.F.,
 $NAMELIST_EOF
ENDNAMELIST
```

# 8. REFERENCES

Busalacchi, A. J. and J. J. O'Brien, 1980, The seasonal variability in a model of the tropical Pacific, J. Phys. Oceanogr., 10, 1929-1951.

Chen, D., L.M. Rothstein and A.J. Busalacchi, 1994. A hybrid vertical mixing scheme and its application to tropical ocean models. J. Phys. Oceanog., 24, 2156-2179.

Chelton, D. B., J. C. Ries, B. J. Haines, L.-L. Fu and P. S. Callahan, 2001. Satellite Altimetry. In: Satellite Altimetry and earth sciences. A handbook of techniques and applications. Ed.: L.-L. Fu and A. Cazenave. Academic Press. 1-131.

Clarke, A. J. and X. Liu, 1994. Interannual sea-level in the northern and eastern Indian Ocean. J. Phys. Oceanogr., 24, 1224-1235.

Ffield, A. and A.L. Gordon, 1996. Tidal mixing signatures in the Indonesian seas. J. Phys. Oceanogr., 26, 1924-1937.

Gates, W.L. and A.B. Nelson, 1975. A new (revised) tabulation of the Scripps topography on a 1 degree global grid. Part I. Terrain heights. Tech. Rep. R-1276-1-ARPA, The RAND Corporation, 132 pp.

Godfrey, J.S. and T.J. Golding, 1981. The Sverdrup relation in the Indian Ocean, and the effect of Pacific-Indian ocean throughflow on Indian Ocean circulation and on the East Australian Current. J. Phys. Oceanog. 11, 771-779.

Godfrey, J.S. and A. Schiller, 1997. Tests of mixed layer schemes and surface boundary conditions in an ocean general circulation model, using an equatorial data set. CSIRO Report 231.

Griffin, D. A, J. L.  Wilkin, C. F. Chubb, A. F. Pearce and N. Caputi, 2002. Ocean currents and the larval phase of Australian western rock lobster, *Panulirus Cygnus.* Marine and Freshwater Research, in press.

Hayes, S. and L. Mangum and J. Picaut and A.Sumi and K. Takeuchi, 1991. TOGA-TAO: A moored array for real-time measurements in the tropical Pacific Ocean. Bull. Amer. Meteor. Soc., 72, 339-347.

Kalney and 21 other authors, 1996. The NCEP/NCAR 40-year reanalysis project. Bull. AM. Met. Soc., 1996, 77, 437-471.

Kessler, W.S., and M. J. McPhaden, 1995, Oceanic equatorial waves and the 1991-93 El Nino, J. Climate, 8, 1757-1774.

Kessler, W.S., G.C. Johnson and D.W. Moore, 2002, Sverdrup and nonlinear dynamics of the Pacific South Equatorial Current. Submitted to J. Phys. Oceanog.

Kessler, W.S, 2002, Mean three-dimensional circulation in the north-east Pacific. J. Phys. Oceanog., accepted.

Kleeman, R. and S.B. Power, 1995. A simple atmospheric model of surface heat flux for use in ocean modeling studies. J. Phys. Oceanogr, 25, 92-105.

Levitus, S., 1982. Climatological atlas of the world ocean. NOAA Prof. Paper No. 13, 173 pp.

Lukas, R., 1986. The termination region of the Equatorial Undercurrent in the eastern Pacific. Journal, Progress in Oceanogr., 16, 63-90.

Masumoto, Y and G. Meyers, 1998. Forced Rossby waves in the southern tropical Indian Ocean. J. Geophys. Res., 103, 27589-27602.

McBride, J.L., M.R. Haylock and N. Nichols, 2001: Relationships between the maritime continent heat source and the El Nino-Southern Oscillation phenomenon. Submitted to J. Climate.

Meyers, G., 1996. Variation of Indonesian Throughflow and the El Nino-Southern Oscillation. J. Geophys. Res., 101, 12255-12263.

Meyers, G.and L. Pigot, 2000. Analysis of frequently repeated XBT lines: IX-1, IX-12, IX-22/PX-11, PX-2, CSIRO Marine Laboratories Report.

Meehl, G.A., P.R. Gent, J.M. Arblaster, B.L. Otto-Bliesner, E.C. Brady and A. Craig, 2001: Factors that affect the amplitude of El Nino in global coupled climate models. Climate Dynamics 17, 515-526.

Niiler, P.P. and E.B. Kraus, 1977. One-dimensional models of the upper ocean. In: E.B. Kraus (Ed.): Modeling and prediction of the upper layers of the ocean. Pergamon Press, Oxford, 143-172.

Peters, H., M.C. Gregg and J.M. Toole, 1988. On the parametrization of equatorial turbulence. J. Geophys. Res., 93, 1199-1218.

Power, S.B., R. Kleeman, F. Tseitkin and N.R. Smith, 1995. On a global version of the GFDL Modular Ocean Model for ENSO studies. BMRC Technical Report.

Reason, C. J. C., R. J. Allan, J A. Lindesay and T. Ansell, 2000. ENSO and climatic signals across the Indian Ocean basin in the global context: part I. Interannual composite patterns. Int J. Climate, 20, 1285-1327.

Reynolds. R. W. and T. M. Smith, 1994. Improved global sea surface temperature analyses using optimum interpolation. J. Climate, 7, 929-948.

Schiller, A., J.S. Godfrey, P.McIntosh and G. Meyers, 1997. A Global Ocean General Circulation Model for Climate Variability Studies. CSIRO Marine Laboratories Report 227.

Schiller, A., J.S. Godfrey, P.McIntosh and G. Meyers and S. E. Wijffels, 1998. Seasonal near-surface dynamics and thermodynamics of the Indian Ocean and Indonesian Throughflow in a global ocean general circulation model, J. Phys. Oceanogr., 28, 2288-2312.

Schiller, A., J.S. Godfrey, P.McIntosh and G. Meyers and R. Fiedler, 2000. Interannual Dynamics and thermodynamics of the Indo-Pacific Oceans, J. Phys. Oceanogr., 30, 987-1012.

Schiller, A. and J.S. Godfrey, 2002. Indian Ocean intraseasonal variability in an ocean general circulation model. J. Climate (accepted).

Shinoda, T. and H.H. Hendon, 1998. Mixed layer modelling of intraseasonal variability in the tropical western Pacific and Indian Oceans. J. Clim. 11, 2668-2685.

Simonot, J.-Y. and H.L. Le Treut, 1986. A climatological field of mean optical properties of the world ocean. J. Geophys. Res., 91, 6642-6646.

Wang, G., O. Alves, N. Smith and F. Tseitkin, 2001: The new version of the BMRC coupled general circulation seasonal forecasting model. BMRC Technical Report.

Webster, P. J., A. M. Moore, J. P. Loschnigg and R. R. Leben, 1999: Coupled ocean-atmosphere dynamics in the Indian Ocean during 1997-98, Nature, 401, 356-360.

Wilson, 2000: How ocean vertical mixing and accumulation of warm surface water influence the "sharpness" of the equatorial thermocline. J. Climate, 13, 3638-3656.

Wyrtki, K. and G. Meyers, 1975: The trade wind field over the Pacific Ocean. Hawaii Institute of Geophysics Report HIG-75-1.

Zhong, A., O. Alves, A. Schiller, G. Wang, F. Tseitkin and N. Smith, 2001: A new version of the BMRC Ocean-Atmospheric General Circulation Model for seasonal predictions: a brief description, BMRC Research Report.

Zhong, A., R. Colman, N. Smith, M. Naughton, L. Rikus, K. Puri and F. Tseitkin, 2001b: Ten-year AMIP1 climatologies from versions of the BMRC Atmospheric Model, BMRC Research Report, 83, 33pp.